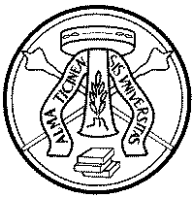

Università degli Studi di Pavia

Dipartimento di Fisica

DOTTORATO DI RICERCA IN FISICA

XXXIII CICLO

LEAD-FREE METAL HALIDE PEROVSKITE NANOCRYSTALS

Novel Nanomaterials for Possible Future Technologies

Alessandro Veronese

Submitted to the Graduate School of Physics in partial fulfillment of the requirements for the degree of

DOCTOR OF PHILOSOPHY IN PHYSICS

at the

University of Pavia

Supervisors: Prof. Maddalena Patrini, Prof. Lorenzo Malavasi

Ad Alessia,

che ha sempre creduto in me

TABLE OF CONTENTS

CONTENT OF THE THESIS

The present thesis focuses on the synthesis and characterization of colloidal nanocrystals of different lead-free metal halide perovskites as possible alternatives to the current lead-based nanomaterials. The aim is to achieve a deeper knowledge of these compounds that are still little known to encourage the research on lead-free perovskites and promote the transition towards more green materials.

The thesis can be divided in two parts. The first part is a review of the basic properties of metal halide perovskites and the relative nanocrystals. *Chapter I* gives a general introduction to the subject, explaining the origin of the recent interest in these compounds and outlining their potentiality and the issues and concerns associated to them.

Chapter II summarizes the main characteristics of metal halide perovskites illustrating their most peculiar features: the crystal structure and the electronic band structure.

Chapter III, instead, focuses on perovskites in the form of colloidal nanocrystals. It presents the synthesis of the crystals, explaining the theory behind their formation and growth. Next, it describes their electronic structure and their optical properties, underlying how the latter are modified by compositional tuning and size reduction. Finally, it addresses the problems related to their stability.

The second part of the thesis is devoted to the experimental work and reports the results of my research. *Chapter IV* concerns the synthesis and characterization of Cs_2SnX_6 (X = Cl, Br, Br/I, I) nanocrystals and presents the results of the investigation on their crystal

structure, size, light absorption, and light emission.

In *Chapter V*, the effects of different capping agents on the crystals of the previous chapter are explored, showing how amines of various length can modify not only their morphology but also their optical properties.

Chapter VI, instead, concerns the synthesis and characterization of $Cs_3Bi_2X_9$ (X = Br, I) nanocrystals and, once again, the structural, morphological, and optical features are reported. It also suggests a possible application of these crystals as photocatalyst in combination with graphitic carbon nitride presenting the results they can achieve in the production of hydrogen.

Finally, *Chapter VII*, the last chapter, summarizes the findings and observations of my research, addresses the main problems that affect these nanomaterials, and outlines the future perspectives for the development of this research topic.

Chapter I
INTRODUCTION

Semiconductors are one of the most significant class of materials of present times since they play a fundamental role in our society. By replacing vacuum tubes with small transistors, semiconductors paved the way to the miniaturization of electronic circuits and, currently, modern electronics is dominated by them.[1–3] Semiconductors are the basis of integrated circuits as well as several discrete devices (e.g. diodes, transistors, rectifiers, LEDs). All these elements are indispensable components for the functioning of almost every device we commonly use in everyday life such as smartphones, computers, televisions, household appliances and lighting systems. In addition to consumer electronics, semiconductors are also of crucial importance for the renewable energy field: the current photovoltaic technology, indeed, is entirely based on these materials. It is easy to understand the tremendous impact that semiconductors have on our lives. Due to vast number of applications and the resulting huge demand for more efficient, powerful, and compact devices, research on semiconductors is in constant evolution and is always looking for new materials and new ways to use them profitably.

In this context, metal halide perovskites (MHPs) have emerged as a novel family of semiconductors that, in the last ten years, has received ever-growing attention from the scientific community. This interest arises from a fortuitous combination of favorable properties and from a series of practical advantages they possess in comparison to conventional II–VI and III–V semiconductors that contribute to make them highly suitable for several applications in

different fields like electronics, photonics and energetics.[4–8] From the electrical point of view, they have unusually long carrier lifetimes and small carrier effective masses which result in long diffusion lengths and, consequently, in good charge-transport properties.[9,10] From the optical point of view, instead, metal halide perovskites exhibit high absorption coefficients and sharp absorption edges as well as photoluminescence characterized by very narrow emission linewidths. This is one of the rare cases in which the same material has simultaneously good properties for both light harvesting and light emission applications.[9,11] Besides that, MHPs have another remarkable property: the possibility to tune in a continuous way their fundamental band-gap over a wide range of wavelengths (from violet to the near infrared) by varying their chemical composition.[12–14] All these features, along with the ease and low cost of processability, contribute to make metal halide perovskites a class of very intriguing and versatile materials and explain the great interest that has developed around them.

Although the earliest studies on MHPs date back to the end of the 1800s,[15,16] it took more than one century before their potential applicability in electronics was explored: the electrical properties of metal halide perovskites were investigated only in the 1990s and early 2000s.[17–21] These initial works marked a fundamental step in the research on metal halide perovskites because they set the basis for their subsequent exploitation in several optoelectronic applications. Since then, a variety of devices have been fabricated with these crystals but the area in which they have obtained the most astonishing results is certainly photovoltaic: starting from a power conversion efficiency less than 4%, after just five years of research perovskite solar cells have reached values of 20% and at present they can achieve certified efficiencies of more than 25%.[22–24]

The idea of exploring MHPs as nanomaterials comes in the wake of the well-established research in the field of nanoscience and nanotechnology. The basic principle of this research is that the behavior of matter is not fixed but depends on its size: due to geometrical factors and quantum mechanical effects, solids exhibit new properties that are not present in their bulk form when their size is reduced to the nanometer scale. This phenomenon is very intriguing because it gives new potentialities to materials already well-known and widely used in their conventional macroscopic form. The research of nanomaterials is then a promising topic that opens up the opportunity for novel fields of investigation and innovative applications.[25–28]

Figure 1.1 Colloidal suspensions of semiconductor quantum dots under UV illumination. Adapted from ref [28].

In the past, a vast number of nanostructures of different dimensionalities has been fabricated with III–V and II–VI semiconductors, producing a wide variety of shapes: particles, rods, wires, platelets are some of the most common forms but more complex and exotic structures like tetrapods or cages have also been explored.[29–32] Following the success of metal chalcogenide quantum dots in suspension, researchers have then tried to produce colloidal nanocrystals (NCs) using metal halide perovskites as well. Already from the first reports, the crystals proved to have extraordinary optical properties.[33,34] Moreover, their synthesis and post-synthetic manipulation revealed to be easy, thus suggesting they could be suitable and advantageous for several applications.[35,36] These findings boosted the research on this topic leading to remarkable results and, currently, MHP NCs are one of the most studied class of nanomaterials, promising to replace conventional semiconductors in many fields of electronics in the future.

Metal halide perovskites are affected by two serious problems that limit their large-scale use: instability and toxicity. Due to the soft nature of their crystal lattice, these compounds are inherently unstable over time and many factors such as temperature, moisture and light irradiation can degrade their structure and properties, undermining the functioning of the related electronic devices.[37,38] The second major issue of MHPs is the presence of lead, a toxic heavy metal that raises great concern for human health and environment safety. Its

dangerousness derives from the severe effects it has on many organs combined with its ease of absorption by the human body, which can occur through skin contact, inhalation, and ingestion.[39–41] In fact, this metal causes acute damage to brain, liver and kidneys, and it can also affect the respiratory, cardiovascular, urinary and reproductive systems. Moreover, there is evidence indicating it as a probable carcinogen.[40,42] Contrary to many substances that are safe or even essential in trace amounts, lead is poisonous at any dose. Even worse, it is hardly excreted by the body and so it tends to accumulate in various tissues over time, mainly in the bones.[43] The toxicity of this heavy metal is related to its ability to interfere with biochemical processes and induce oxidative imbalance. Lead, indeed, can easily bind to different biomolecules, such as proteins, lipids, and nucleic acids, by replacing the metal ions present in them. This alters the normal behavior of the molecules and, consequently, affects the functions of the organs. In addition, Pb can induce changes in the cell membrane, promote the generation of free radicals and decrease the concentration of many antioxidants.[40,41] All these actions result in high oxidative stress that damages the cell structures as well as proteins and DNA.

At present, lead halide perovskites are the best performing ones, but their hazardousness poses a sizeable obstacle to their widespread commercialization in daily applications. The main concern regarding perovskite-based devices is the possible leakage of Pb during both the operation period and the final dismantling. In fact, device encapsulations proved to be ineffective in preventing the metal from leaking into the environment, especially in the occurrence of extreme events like heavy rains or fire.[44,45] Moreover, the bioavailability of Pb originating from perovskites is ten times higher than that of other compounds, therefore the risk of lead pollution from MHPs is a real threat.[46]

To overcome the problem of toxicity, new compounds that replace Pb with more environmentally friendly elements are being explored with great attention.[47–49] Such elements can have the same oxidation state of lead like tin or germanium, or a different oxidation state like bismuth, antimony, or titanium (*Figure 1.2*).[50] These alternative perovskites exhibit interesting features that make them very promising, however, when compared to their lead-based counterpart, they appear considerably inferior: their optical properties are much poorer as well as their stability. Despite their problems, lead-free compounds are of crucial importance for the progress of the perovskite-based technology: considering the high toxicity of Pb and the

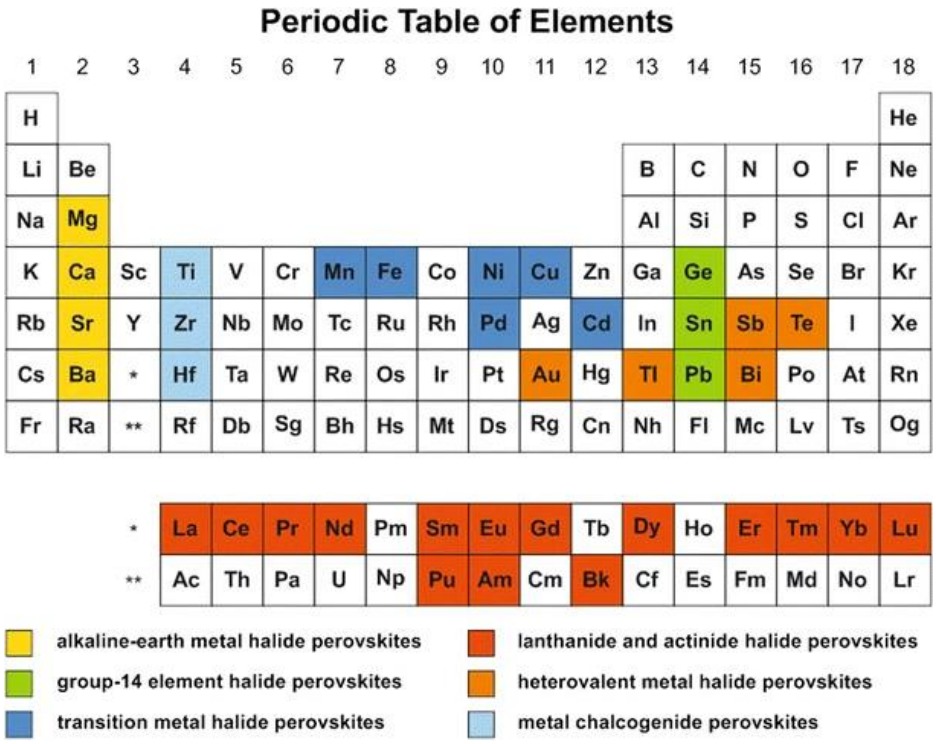

Figure 1.2 Possible lead replacements to achieve lead-free perovskites. Substitutions include homovalent elements from Group 14, heterovalent neighbouring elements, transition metals, alkaline-earth metals, rare earths, and metal chalcogenide perovskites. Adapted from ref [50].

growing sensitivity to the environment from a political and social point of view, it is very unlikely that lead-containing devices will ever be put on the market. Therefore, more research and more thorough investigations are necessary to understand the fundamentals of lead-free perovskites and improve their performances to promote the development of this field.

Chapter II

AN OVERVIEW OF METAL HALIDE PEROVSKITES

2.1 Crystal Structure

The term "perovskite" was originally coined in honor of the Russian mineralogist Lev A. Perovski to name a mineral of calcium titanate ($CaTiO_3$) discovered in 1839 by Gustav Rose in the Ural Mountains.[51] Now the term is used to indicate any crystalline solid that shares the same crystal structure of $CaTiO_3$. Besides that, perovskites are also characterized by the general formula ABX_3, where A and B are cations while X is a non-metallic anion.

The building blocks of the perovskite structure are identical octahedra made of six X ions placed in the corners and one B ion placed in the center. In the ideal case, the $[BX_6]^{4-}$ octahedra are arranged in a simple cubic array, sharing one corner in each of the three directions, while the A ions are placed in the interstitial spaces between adjacent octahedra to grant structural stability and charge neutrality (*Figure 2.1*).[52] In this configuration, the cations present a high coordination number: the A atoms are in 12-fold coordination and the B atoms are in 6-fold coordination.

The so-called classical perovskites are a large class of metal oxides like the aforementioned $CaTiO_3$. In these materials, A is a large metal ion, such as alkaline earths or rare

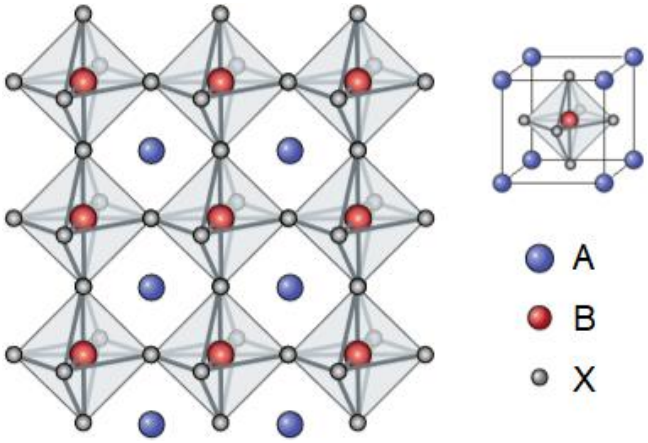

Figure 2.1 Crystal structure of an ideal perovskite. The X ions are placed in an octahedral arrangement around the B ions. The $[BX_6]^{4-}$ octahedra are then connected through their corners to form a continuous three-dimensional matrix. The A ions are instead located in the voids within this matrix. Adapted from ref [52].

earths (e.g. Mg, Ca, Sr, La, Nd, Yb, Lu, Hg, Pb), B is a smaller ion, typically a transition metal (e.g. Ti, Fe, Ni, Y, Zr, Ce, Er, Yb, Si, Pb), and X is clearly oxygen in the 2– oxidation state. According to the oxidation numbers of the cations, instead, three pairings of ions are possible: monovalent and pentavalent ($A^{+}B^{5+}O^{2-}_3$), bivalent and tetravalent ($A^{2+}B^{4+}O^{2-}_3$), and trivalent and trivalent ($A^{3+}B^{3+}O^{2-}_3$). In the past decades, these perovskites were largely studied due to their remarkable properties like piezoelectricity, ferroelectricity, ionic conductivity and magnetoresistance.[53–55] Although oxides are the most common and known compounds, also nitrides,[56,57] hydrides[58,59] and chalcogenides[60,61] are found to crystallize in this structure, thus contributing to make perovskites one of the most abundant and heterogenous families of crystals.

MHPs have the same lattice of oxide perovskites but with some substantial differences in the chemical composition. Firstly, as it is apparent from the name, the X anion consists of a halide (Cl^-, Br^-, I^-) in place of oxygen. Then, the A site is occupied by a monovalent ion that can be either a metal or an organic molecule. Cesium Cs^+ and rubidium Rb^+ are the typical inorganic A cations while methylammonium $CH_3NH_3^+$ (MA^+) and formamidinium $CH(NH_2)^+$ (FA^+) are the most common organic ones. According to the nature of this ion, MHPs are differentiated into hybrid organic-inorganic perovskites (HOIPs) and totally inorganic perovskites (TIPs). Finally,

the B cation is still metal but exclusively in the 2+ oxidation state. As discussed in *Chapter I*, lead Pb^{2+} is the most widely used element, however, due to its toxicity, other metals, even with a different electronic configuration, are being explored to obtain safer materials. Some examples of such replacements are tin Sn^{2+}, germanium Ge^{2+}, copper Cu^{2+}, and also bismuth Bi^{3+}, antimony Sb^{3+}, titanium Ti^{4+} and palladium Pd^{4+}.[7,47,62,63] This change in the oxidation number of the B cation causes a modification of the standard perovskite structure as it will be discussed later on. According to the metal, MHPs are further differentiated into lead halide perovskites (LHPs) and lead-free halide perovskites.

Similar to the case of classical perovskites, varying the chemical composition of MHPs allows to obtain a vast number of compounds with very different and tunable properties that may be suitable for a wide range of applications. [5,6,55,64]

The capability of a crystal to adopt the perovskite structure relies on two parameters: the Goldschmidt tolerance factor t and the octahedral factor μ. In the assumption purely ionic bonding, these factors are dimensionless geometrical parameters that depends exclusively on the radii r_I (I = A, B, X) of the perovskite constituting ions, as shown in *Equations 2.1* and *2.2*:

$$t = \frac{1}{\sqrt{2}} \frac{(r_A + r_X)}{(r_B + r_X)} \tag{2.1}$$

$$\mu = \frac{r_B}{r_X} \tag{2.2}$$

The Goldschmidt tolerance factor quantifies the mismatch between ion sizes that the perovskite lattice can tolerate before turning in a different structure, thus it allows to predict the formability and the stability of a crystal. It was first proposed by Victor M. Goldschmidt in 1926 on the basis of the so-called “non-rattling postulate”, which is that perovskites arrange their atoms so as to maximize the number of anions surrounding each cation.[65–67] Originally, the tolerance factor was introduced to describe the structure of oxide perovskites but it can be extended to MHPs as well.[68,69] The octahedral factor, instead, evaluates the possibility for the B cation to fit into the octahedral interstices of the anion sublattice thus forming a regular $[BX_6]^{4-}$ octahedron. In the last years, more sophisticated factors, that take into account also

other quantities in addition to the ionic radii, have been proposed as a reliable tool to predict more accurately the formability of perovskites.[69–72]

In theory, a compound can form the ideal cubic perovskite lattice only if it has a tolerance factor of 1. In fact, it was observed that cubic perovskites can form for a range of *t* values close to unity. Moreover, outside this range a crystal can still adopt modified perovskite structures, with a lower degree of symmetry, derived from the ideal lattice by distorting the cubic array of corner-sharing octahedra (*Figure 2.2*).[73] The distortions are meant to improve the coordination environment around the cations and frequently result in a reduction of their coordination numbers.[66,74] They are generally induced by an interplay of four main elements: size effects related to geometrical factors, electrostatic interactions between the organic cations and the crystal lattice, deviations from the ideal chemical composition, and the Jahn–Teller effect.[75,76] Size effects, as discussed above, depend on ionic radii and the shape of the A cations, with the resulting capability of the materials to arrange in the cubic perovskite structure as predicted by the tolerance and octahedral factors. The interactions between the organic cations and the surrounding environment are of two types: nondirectional electrostatic interactions and directional hydrogen bonds.[77] They originate from the cation charge and the electric dipole moment that is typically present in molecular ions, and their effect is to stretch, contract, tilt or twist the inorganic network of $[BX_6]^{4-}$ octahedra.[76,78] The alterations of the ideal formula ABX_3, instead, can lead to deficient compounds in which the vacancies may adopt a long-range

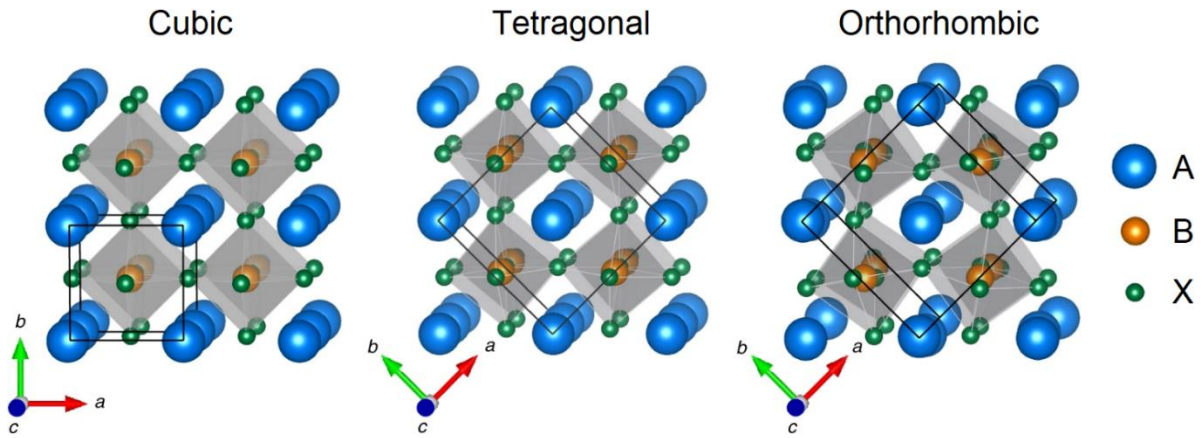

Figure 2.2 Crystal lattice of cubic, tetragonal, and orthorhombic perovskites in comparison. Adapted from ref [73].

order and modify the crystal structure.[79,80] Finally, the Jahn–Teller effect involves those compounds presenting an active ion in the B site. In this case, the degeneracy of the highest occupied metal orbital causes a deformation of the octahedra according to the Jahn–Teller theorem.[74,75] It is very common for perovskites to have multiple crystal phases and sometimes the stable phase under ambient conditions is not the cubic but a less symmetric one, like tetragonal or orthorhombic.[81,82]

For oxide compounds, it was empirically found that perovskite structures can form for $0.75 < t < 1.00$ and $0.45 < \mu < 0.90$, approximately.[66,83] The cubic phase, in particular, occurs in a narrower range of t values, namely for $0.80 < t < 0.95$.[84,85] On the other hand, when $t < 0.75$ or $t > 1.00$, the A cation appears to be, respectively, too small or too large to properly fit in the perovskite lattice and so different polymorphs become more favorable and stable. In the case of metal halide compounds, instead, the formability range for perovskite structures is estimated to be $0.80 < t < 1.10$, while, due to the lower electronegativity of the halides (especially the larger ones like iodide) and the non-sphericity of the molecular cations, the cubic window is reduced to $0.90 < t < 1.00$.[66,86–88] As it will be seen in the next chapter, this has not

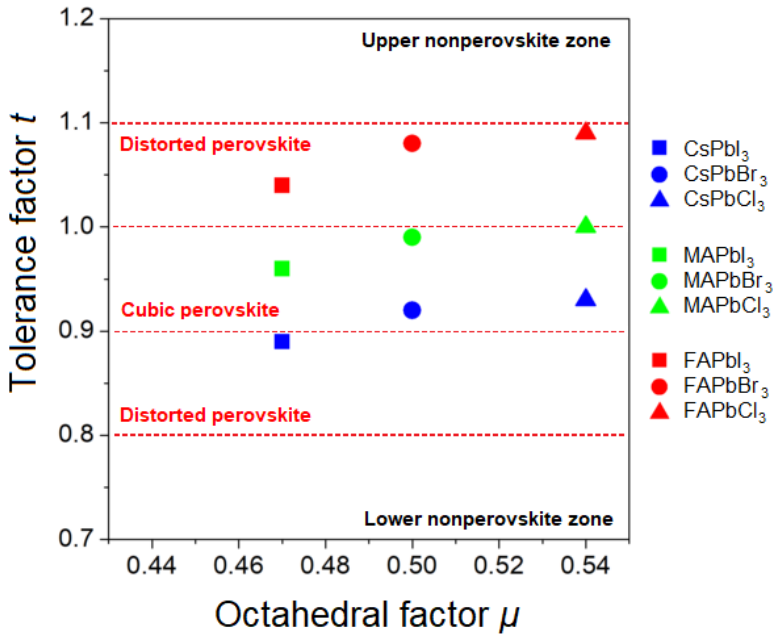

Figure 2.3 Tolerance factors of some of the most common lead halide perovskites with different halides and cations.

negligible consequences on the structural stability of MHPs.

When the value of the tolerance factor falls outside the stability range or the constituting ions have oxidation numbers different from those required by the chemical composition ABX_3, new crystal structures derived from the perovskite lattice are favored. These structures are obtained from the periodic repetition in space of a fundamental unit made of $[BX_6]^{n-}$ octahedra connected through corners, edges, or faces, whereas the A cations are packed around these inorganic blocks and keep them separated from one another. According to the connectivity of the octahedra, the materials are classified as three-dimensional (3D), two-dimensional (2D), one-dimensional (1D) and zero-dimensional (0D) perovskites.[89,90] As depicted in *Figure 2.4*,[90] in 3D compounds the octahedra are connected in all three directions creating a continuous network of metal and halide ions with the A cations placed into the voids in between. In 2D compounds, like $Cs_3Bi_2Br_9$ or $CsPb_2I_5$, the building units are planar or corrugated layers of octahedra stacked on each other. In 1D compounds, instead, like $CsTiBr_3$ or Cs_3PbI_5, the constituting units are chains of octahedra that can be either straight or zigzag. Finally, in 0D compounds, like Cs_2SnBr_6 or Cs_4PbI_6, the octahedra are completely isolated or connected in small clusters separated from one another.

In this context, the A cation plays a crucial role in the formation of MHPs with reduced dimensionality: once the metal and the halogen are chosen, the tolerance factor defines the size ranges in which the A radius must fall to achieve a cubic 3D, a distorted 3D, or a lower-dimensional perovskites.[91,92]

It should be noted that only three-dimensional crystals with chemical composition

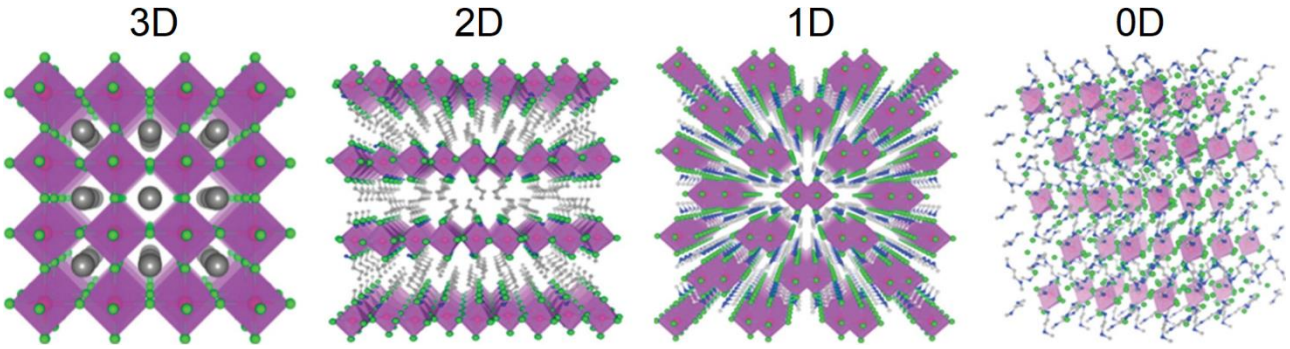

Figure 2.4 Crystal structure of low-dimensional perovskites. Adapted from ref [90].

ABX_3 are actual perovskites based on the very definition of perovskite. Crystals with a different structural dimensionality should be more precisely called non-perovskites or perovskite derivatives since they are in fact a rearrangement of the perovskite octahedra. Nevertheless, the name "perovskite" is still accepted and widely used for these materials if their dimensionality is explicitly specified.

A final case of perovskite derivatives is the so-called double perovskite, characterized by the general formula $A_2B'B''X_6$. These compounds exhibit the same crystal structure of a regular 3D perovskite, but the B sites are alternatively occupied by two different metal species B′ and B″ that can have the same oxidation number 2+ or, more commonly, two distinct numbers, namely 1+ and 3+ to keep the charge neutrality.[62,93] Compared to standard perovskites with formula ABX_3, the unit cell of these compounds appears doubled to consider both metals, hence the name "double perovskites".

2.2 Electronic Structure

2.2.1 Energy Bands

In the following we will specifically focus on lead halide perovskites. These materials were the first MHPs to be studied and currently are the most investigated ones since they are the best performing and most promising compounds for optoelectronic applications. For this reason, lead-based perovskites can be considered as the archetype of MHPs, and their properties can be taken as a benchmark for the entire class of halides.

The unusual energy band structure of LHPs is one of their most distinctive features. Contrary to classical semiconductors, in these materials both the conduction band (CB) and the valence band (VB) arise from σ^* antibonding interactions between the lead and the halide orbitals as shown in *Figure 2.5*.[94] Considering the electronic configuration of these two ions,

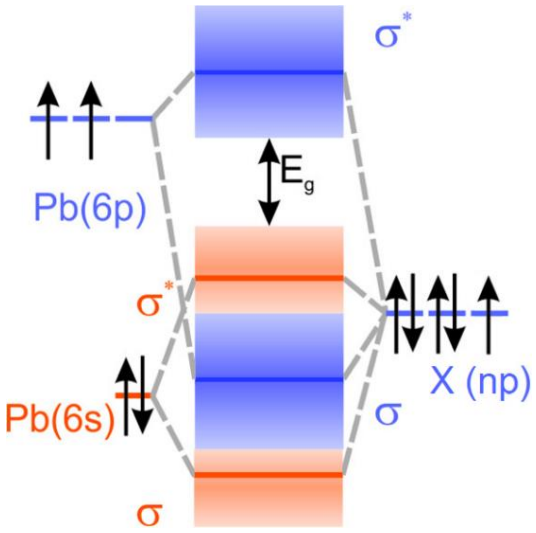

Figure 2.5 Schematic illustration of the formation of the electronic band structure for lead halide perovskites starting from the individual s and p orbitals of Pb and X ions. Adapted from ref [94].

namely $6s^26p^0$ for Pb in the oxidation state 2+ and np^6 for X in the oxidation state 1– (n = 3–5 from Cl to I), the CB originates from the binding between the Pb 6p and X np states, whereas the VB originates from the binding between the Pb 6s and X np states.[14,94,95] Due to the constituting orbitals, the CB has a strong p-type character while the VB shows a partial s-type character. In this framework, it appears evident that the A ion does not take part directly in the formation of the electronic band structure of LHPs because the bands are generated uniquely by the orbitals of the metal and the halide. The only effect of this cation is to distort the inorganic octahedra array through the interactions with the surrounding ions, thus causing a change in the lattice parameters and, consequently, in the gap energy.[78]

LHPs are direct gap semiconductors and, interestingly, the conduction band minimum (CBM) and the valence band maximum (VBM) do not occur at the Γ point, as in many conventional semiconductors, but at one edge of the Brillouin zone like, for example, the R point. Since lead and halogens (especially iodine) are heavy elements, the spin–orbit coupling (SOC) in LHPs is strong, so it has a sizeable effect on their energy band structure. Due to its pronounced p-type character, this interaction affects mainly and deeply the CB: it causes, indeed, a split-off of the conduction band into two distinct states with different total angular

momentum *J*, namely 3/2 for the upper band and 1/2 for the lower one.[96,97] This phenomenon is analogous to the formation of the split-off band of traditional semiconductors, however in these materials the band is part of the VB and lies below the light hole branch while in LHPs it is part of the CB, therefore the electric band structure of perovskites appears inverted compared to that of conventional semiconductors. By lowering the CBM, the spin–orbit splitting results in a reduction of the bandgap: depending on the compound, the energy decrease can reach values of almost 1 eV. Moreover, the spin–orbit interaction enhances the energy dispersion of the CB in the **k**-space near the band edge and slightly shifts the CBM and VBM from the original point of the Brillouin zone at which they occur.[14,98] Regarding the VB, instead, the effects of the SOC are radically different. Having a more s-type character, this band remains essentially unaffected by the coupling. However, because of the strong hybridization between the s and p orbitals of lead and halide, also the VB presents a pronounced curvature in the **k**-space near the band edge.[98]

Since the VBM is mostly dominated by the p orbitals of the X ion, changing the halide content causes substantial modifications in the electronic band structure: going from Cl to I, indeed, the bandgap is considerably reduced (*Figure 2.6*).[99] This shrinkage is mainly determined by the decreasing difference of electronegativity between the halogen and the metal and their increasing interatomic distance.[95,100] As the distance between B and X grows, the CBM is lowered because the electrons on the metal atoms are less confined and so their energy levels decrease. On the other hand, the VBM is raised because, as the halogen electronegativity drops, its p levels rise significantly. The position of the VB is the result of three competing factors: the aforementioned reduced confinement of electrons and the less hybridization strength between the B s and X p orbitals would tend indeed to move the band edge in the opposite direction. However, the rising of the halogen p levels has a much more incisive effect than the other two phenomena and so it dominates over them. In fact, the reduction of the gap energy is mostly driven by the upshift of the VBM rather than the downshift of the CBM, which is very limited.

In the case of the B ion, instead, the situation appears quite different. Since the CBM and VBM depends similarly on the orbitals of this ion, they both shift in the same direction when the metal content is modified, therefore the outcomes of lead replacement on the bandgap of

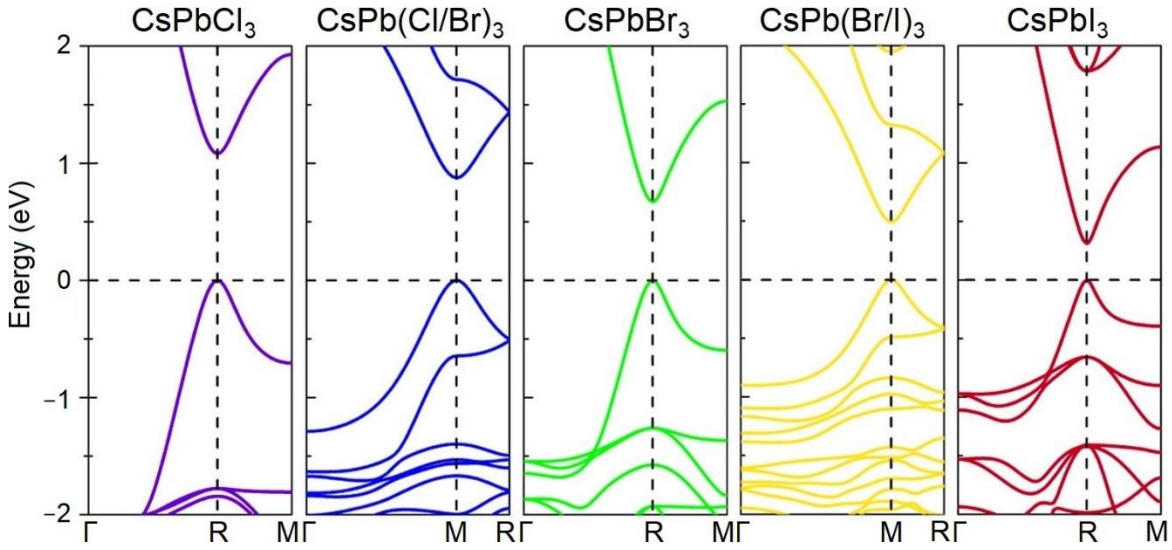

Figure 2.6 Electronic band structure of $CsPbX_3$ perovskites (X = Cl, Br, I) with different composition. The effects of the halide content on the energy bands are evident. Adapted from ref [99].

LHPs are more difficult to predict.

Finally, the A cation has even more subtle effects on the band structure. As previously mentioned, this ion does not intervene actively in the formation of the electronic bands but still has an indirect influence on them. In fact, it can modify the B–X bond length and the B–X–B bond angle through size effects and the electrostatic interactions with the surrounding lattice.[77,78,101] These modifications lead to a different overlapping between the metal and halide orbitals and a different spin–orbit interaction, therefore the alterations of the crystal structure result also in alterations of the band structure.[12,101,102] As the A cation varies, both band edges shift in the same direction, however the cation-induced lattice distortions affect mostly the VB and increase the bandgap due to the reduced overlap and hybridization between the B s and X p orbitals, while the cation-induced volume expansion affects mostly the CB and decreases the bandgap due to enhanced interatomic distance. The variations induced by the A cation in the band structure are moderate compared to those related to the X ion, nevertheless they are of considerable importance because they allow to get a finer tuning of the perovskite optoelectronic properties. For example, moving from $CsPbI_3$ to $FAPbI_3$ only decreases the bandgap of about 200 meV, from 1.72 eV to 1.51 eV.[95]

Playing with the chemical composition is then a very powerful tool that offers unlimited potential because it allows to obtain an endless number of compounds with the desired properties for any purpose (*Figure 2.7*).[95]

Besides the elemental composition, octahedra connectivity also has a considerable impact on the electronic structure of perovskites. As mentioned above, lattice distortions affect the energy bands because they alter the overlap between the orbitals of neighboring metal and halide ions. As a general rule, when the symmetry of the perovskite lattice is lowered, the energy of the bandgap grows and the band dispersion in the **k**-space decreases.[103] This phenomenon is related to the concept of electrical dimensionality: this parameter quantifies effectiveness of the overlapping between the orbitals of adjacent $[BX_6]^{n-}$ octahedra and the ease with which the electrons can hop from one octahedron to the next. Structural and electrical dimensionalities are strongly linked together but they do not always have the same value: the electrical dimensionality can be lower than the structural dimensionality but never higher. For example, cubic and tetragonal $MAPbI_3$ have both a 3D structure but the latter has a slightly reduced electrical dimensionality due to the different Pb–I–Pb angle, resulting in a higher bandgap.[104] Another example is the double perovskite Cs_2SrPbI_6: it is structurally 3D but electrically 0D because only Pb takes part in the formation of the band structure, therefore the $[PbI_6]^{4-}$ octahedra result to be electrically separated by the $[SrI_6]^{4-}$ octahedra.[103]

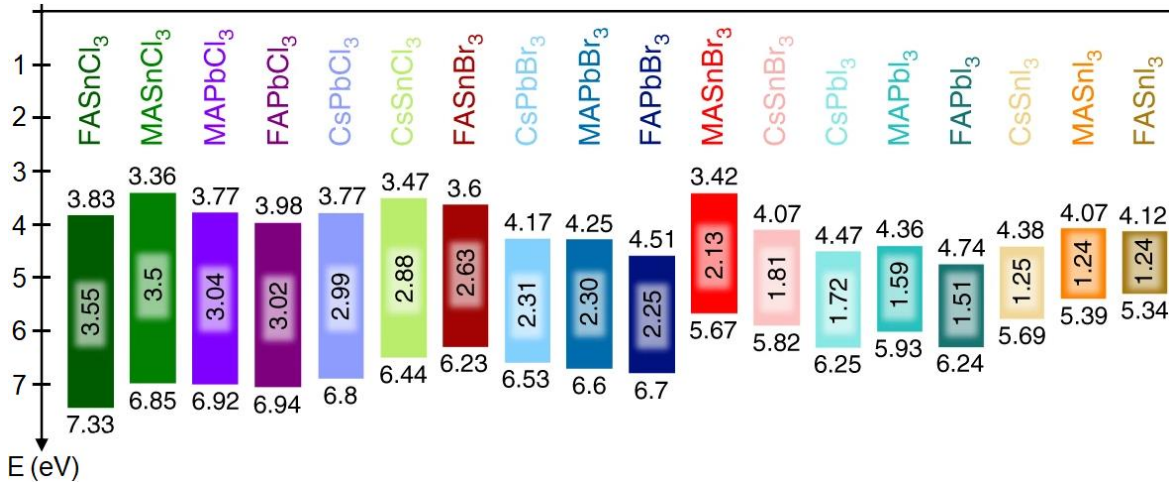

Figure 2.7 Bandgap values and absolute energy level positions with respect to the vacuum level for different lead-based and tin-based halide perovskites. Adapted from ref [95].

The effects of reduced electrical dimensionality are even more pronounced in the case of low-dimensional perovskites. Since their building blocks are totally isolated from one another, they show a flat dispersion of the energy bands in the directions along which the octahedra are not connected, as shown in *Figure 2.8*.[90,103] In fact, these materials can be imagined as macroscopic periodic assemblies of their constituting units, therefore their band structure reflects the structure of the single metal-halide unit.

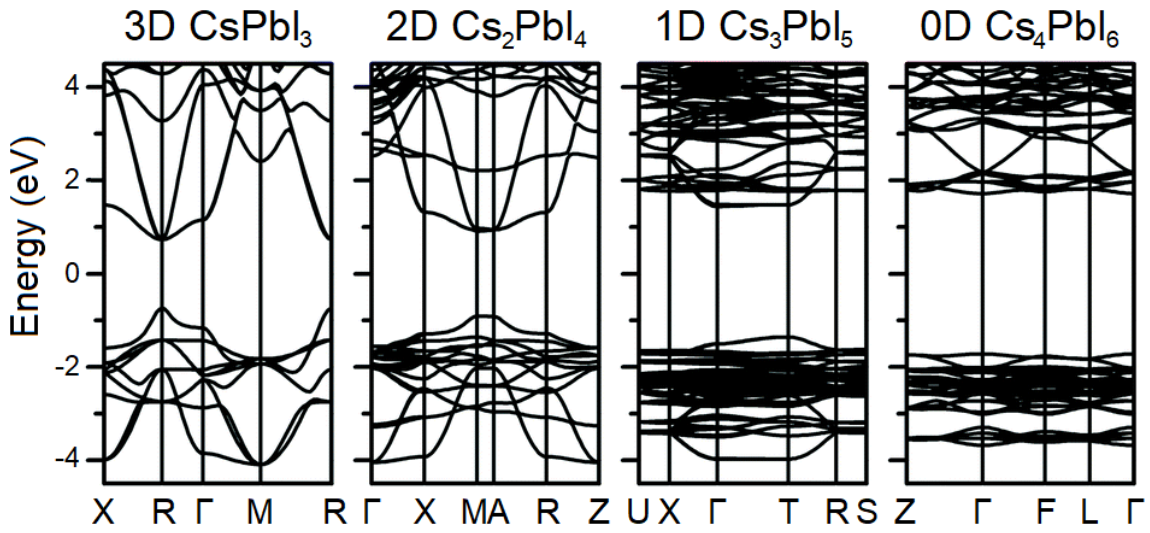

Figure 2.8 Electronic band structure of metal halide perovskites with different structural dimensionality. As the dimensionality is lowered, the dispersion of the energy bands decreases, and their profile becomes flatter and flatter. Adapted from ref [103].

2.2.2 Defect Tolerance

The peculiar nature of the LHP band structure has a remarkable outcome. Typically, the energy levels introduced by vacancies and surface dangling bonds lie between bonding and antibonding states (the surface of a crystal can be imagined as a plane of vacant ions, hence surface defects should show a behavior similar to vacancies). In the case of LHPs, where the CB and VB are both generated by antibonding interactions, these levels tend then to fall within the bands or close to their edges (shallow states) rather than in the gap (deep states). In such situation, defect states appear almost delocalized and consequently they cannot act efficiently as electronic traps (*Figure 2.9*).[105] The strong SOC of LHPs, moreover, further stabilizes their

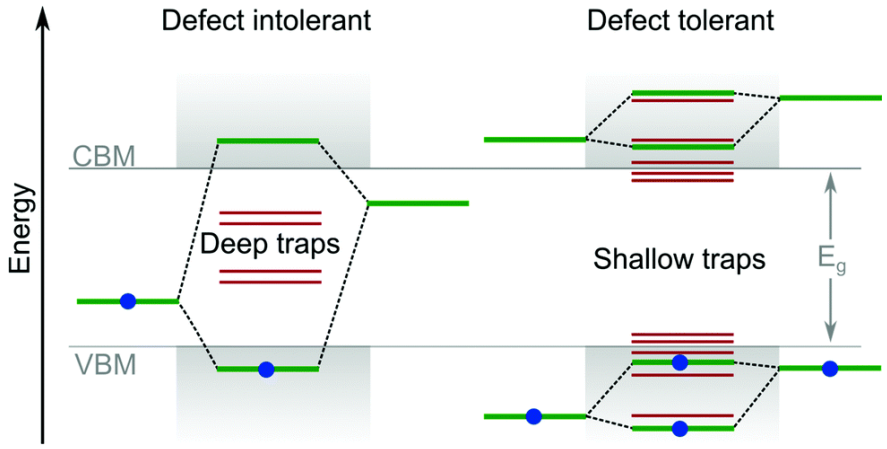

Figure 2.9 Visual representation of defect tolerance related to the bonding and antibonding nature of the energy bands. Adapted from ref [105].

energy band structure by lowering the CBM. This feature, by which defects are present in a crystal but do not affect its properties as if they were inert, is called defect tolerance[106] and it was proved to be a common property of many metal halide perovskites[94,107,108] and other semiconductors like metal chalcogenides.[94,109,110]

The defect-tolerant nature of LHPs is also related to their dielectric response. These materials, indeed, are characterized by a high dielectric constant ε across a broad range of frequencies.[111–113] This results in an effective screening of charged crystal defects and, therefore, in a reduction of their carrier capture cross-section σ_t.[94,114] Assuming a coulombic model, σ_t can be expressed as:[115]

$$\sigma_t = \frac{e^4}{16\pi(\varepsilon k_B T)^2} \tag{2.3}$$

where e is the electron charge, k_B is the Boltzmann constant, and T is the temperature.

From *Equation 2.3* it appears evident that high values of ε determine low values of σ_t, thus a large static dielectric constant is beneficial to semiconductors because it reduces the scattering and trapping of charged defects and impurities, thus improving consequently their defect tolerance.

The origin of the high dielectric constant in LHPs is related to multiple factors. In fact, several processes that induce a polarization occur in these materials at different frequencies, although the precise mechanisms under their contributions to the dielectric response are not fully understood yet.[116,117] In the infrared region (above 1 THz), ε is dominated by the ionic polarization arising from lattice vibrations and deformations of the $[BX_6]^{4-}$ octahedra. The internal vibrations of the organic cations further increase this type of polarization. Below 1 THz, the highly dynamic reorientation of the molecular ions is the main factor that enhances the dielectric constant.[118] Owing to their dipole moment, the organic A cations can in fact interact with one another and adopt a particular arrangement within the inorganic metal-halide sublattice, thus leading to orientation polarization. Below 1 GHz, instead, the electron conduction and the ionic drift induce space-charge polarization that additional increase the value of ε. Compared to conventional semiconductors, due to their high mobility, ion motions in LHPs have a greater impact on the dielectric response of the material compared to conventional semiconductors, especially the halide diffusion.[118,119] At low frequencies (below 1 Hz), were proved to have a giant dielectric constant reaching values of the order of 10^3–10^4 times the vacuum permittivity, which can even be further enhanced by three orders of magnitude when the crystals are illuminated above the gap energy.[111,120,121] This phenomenon is believed to originate from structural fluctuations induced by the coupling between photoexcited electrons and phonons, namely photogenerated polarons, and it may also be assisted by the dipole–dipole interaction of the molecular A cations.[111]

Another factor the contributes to the high dielectric constant of lead-based perovskites is their Born effective charge. This quantity is a tensor that relates the macroscopic polarization of a crystal with the displacements of its ions under the condition of zero external electric field, thus it describes the ionic polarizability of a material. As previously discussed, in MHPs the metal is partially oxidized, namely it is in the oxidation state 2+ and has the electronic configuration $6s^26p^0$. The lone pair of electrons in the outermost s orbital makes Pb ions highly polarizable. This increases the mixed ionic-covalent nature of the bonding between metal and halide and induces a large Born effective charge which, in turn, leads to a high dielectric constant.[94,114,122]

The formation energy of defects also plays a role in the defect tolerance of LHPs.

Several studies have demonstrated that, typically, point defects introducing shallow electronic states have low formation energies, while point defects introducing deep electronic states have, on the contrary, higher formation energies.[94,107,123,124] For example, LHPs usually present large concentrations of vacancies, mostly of the A and X ions, but, as mentioned above, these defects are related to shallow levels and so they reveal to be not detrimental for the crystals. Other kinds of defects, instead, like interstitials and antisites that may generate deep trap levels, have much higher formation energies since ions are energetically difficult to misplace in the perovskite lattice, therefore their concentrations in LHPs are very low and appear to be negligible.[94,125]

Chapter III
AN OVERVIEW OF PEROVSKITE NANOCRYSTALS

3.1 Synthesis

The methods to produce nanomaterials can be divided in two main categories: top-down and bottom-up. The top-down methods consist in breaking down bulk materials to reduce their size to the nanoscale. They include, for instance, mechanical milling, high pressure torsion, sputtering, etching and lithography with light, electrons, or ions. These techniques are suited for fabricating structures with long-range order and have the advantage of being less expensive, but they lose accuracy on very low dimensions.[25,126,127] The bottom-up methods, instead, consist in growing nanomaterials starting from their constituting elements: they are based on the self-assembly and positional assembly of single atoms, molecules or clusters by exploiting physical and chemical processes. The most common bottom-up approaches are wet chemical syntheses like the sol–gel method, inert gas condensation, chemical vapor deposition, molecular beam epitaxy and atomic manipulation via scanning tunneling microscope. These techniques are suited for fabricating great quality structures with short-range order given their high precision, however they are more expensive and they are not always scalable at the industrial level.[25,126,127]

Colloidal nanocrystals are mostly produced with bottom-up methods, specifically by

wet chemical syntheses. This kind of syntheses comprises of three general steps: the preparation of a precursor solution, the chemical reaction that leads to the formation of the perovskite NCs, and the purification of the obtained crystals. In the first stage, the precursors of the perovskite are combined in a solvent along with the ligands. During this phase, the reagents dissolve in solution and the resulting metallic and non-metallic species form coordination complexes with the ligand molecules. These complexes are usually referred to as monomers; it should be noted that they are not metal-organic compounds because they do not comprise metal–carbon bonds. The precursors typically used in the synthesis of MHPs are solid, of which the most common are acetates and halides, but liquid compounds can also be employed.[36,128,129] In this case, the precursors do not need complexation.

In the second step, the actual synthesis of the NCs takes place. At this stage, the monomers react among them and produce the first seeds for the growth of the perovskite. The formation of NCs is described by the LaMer model and can be divided into three additional phases that strictly related to the concentration of monomers in solution: induction, nucleation, and growth (*Figure 3.1 A*).[29,130,131] In the induction phase (phase I), the monomer concentration C is quickly raised until it reaches the critical saturation value C_c, namely the concentration corresponding to the solubility limit of the monomers in the used solvent. This condition can be achieved, for example, by adding one last precursor in the solution. Alternatively, it can be obtained by reducing the solubility of the monomers through the decrease of the solvent temperature or the addition of a poor solvent into the mixture. When the monomer population exceeds the critical threshold, the system enters the nucleation phase (phase II) where the perovskite NCs begin to form. In this stage, the solution reaches a supersaturation concentration C_{ss} and becomes thermodynamically unstable, thus triggering a rapid burst of nucleation: to lower their concentration, the monomers start to react and produce small clusters of atoms that are called indeed nuclei. This process depletes very quickly the monomer population and therefore their concentration drops. Finally, in the growth phase (phase III), the monomer concentration returns below the critical value and the nucleation halts since now it is thermodynamically too costly. In this regard, C_c can be seen as the minimum concentration needed to obtain nucleation. At this stage, the already formed nuclei can dissolve back into the solution or grow into nanocrystals. The crystal growth continues until the

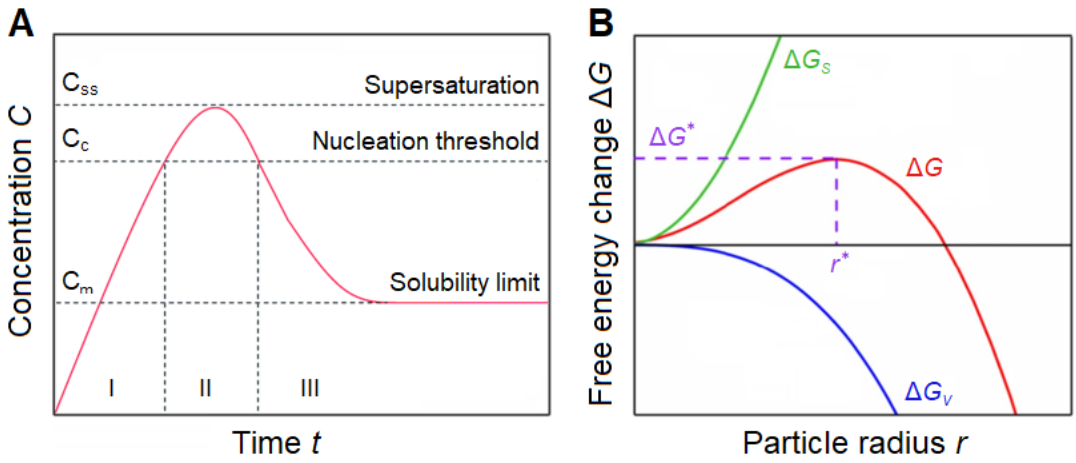

Figure 3.1 (**A**) Diagram of LaMer mechanism for the formation of colloidal nanocrystals. Adapted from ref [130]. (**B**) Gibbs free energy for the formation of solids from a liquid phase. Adapted from ref [133].

monomer population is exhausted to the minimal saturation value C_m, which corresponds to the solubility limit of the perovskite in the used solvent.

The nucleation and growth processes are explained by LaMer model based on the classic nucleation theory. This theory was originally proposed to describe the formation of liquid droplets from a vapor, but LaMer extended it to describe the formation of solid colloids from a liquid.[130,132] The basic principle of the model is that the system always tend to minimize its Gibbs free energy as new volumes and interfaces are produced. The excess free energy ΔG between a solid particle of a crystal dispersed in a liquid and the crystal dissolved in the liquid depends on two terms: the Gibbs free bulk energy ΔG_V, that represents the energy contribution arising from the formation of bulk, and the Gibbs free surface energy ΔG_S, that represents the energy loss arising from the formation of a surface. In the case of a spherical particle, ΔG can be expressed by the following formula:

$$\Delta G = \Delta G_V + \Delta G_S = -\frac{4\pi}{3}\frac{k_B T}{V_m} r^3 \ln(S) + 4\pi\gamma_S r^2 \qquad (3.1)$$

where r is the particle radius, γ_S is the superficial density of interfacial energy, V_m is the molar volume of the solute, and S is the degree of supersaturation defined as the ratio between the

solution concentration and the equilibrium concentration at the solubility limit of monomers C_c.

As it is evident from *Equation 3.1*, the Gibbs bulk free energy is always negative while the Gibbs surface free energy is always positive. Consequently, the balance between these two terms determines the trend of the excess energy as a function of the particle radius (*Figure 3.1 B.*)[133] For small crystal size, ΔG results to be positive because, due to the high surface–volume ratio, it is dominated by the adverse contribution of the interface. As the particle diameter increases, ΔG reaches a peak value and then it starts to decline owing to the predominant contribution of the bulk, until it eventually becomes negative. The maximum value of the excess energy, called critical energy ΔG^*, occurs in correspondence of a critical radius r^*, which from *Equation 3.1* can be derived as:

$$r^* = -\frac{2\gamma_S V_m}{k_b T \ln(S)} \tag{3.2}$$

$$\Delta G^* = \frac{16\pi\gamma_S^3 V_m^2}{3(k_b T \ln(S))^2} \tag{3.3}$$

The critical radius is a fundamental parameter since it determines the evolution of the nuclei after the nucleation phase is concluded. In fact, since they tend to minimize their Gibbs free energy according to LaMer model, the clusters with a radius small than r^* will redissolve into the solution while the clusters with a radius larger the r^* will grow to increase their volume. This process leads then to a focusing of the NC size distribution because the smaller crystals tend to disappear in favor of the bigger crystals that, in turn, develop towards a similar size. To achieve a narrow distribution, it is also important that the three phases are well separated so that new nuclei do not form during the growth of the others.

The nucleation rate R_n can be expressed using the Arrhenius reaction rate formula, which is commonly employed to describe thermally activated processes:

$$R_n = R_0 \exp\left(-\frac{\Delta G^*}{k_B T}\right) = R_0 \exp\left(-\frac{16\pi\gamma_S^3 V_m^2}{3(k_b T)^3 \ln(S)^2}\right) \quad (3.4)$$

where R_0 is a constant.

Equation 3.4 reveals that the nucleation rate has a strong dependance on the temperature of the system, the supersaturation level, and the nature of the synthesis expressed by the interface energy γ_S. In particular, the equation allows to understand the evolution of the nucleation process during time: as the concentration of monomers approaches their solubility limit, S tends to 1 and, consequently, the reaction rate tends to 0, in other words when the concentration reaches the critical threshold C_c the nucleation stops.

The crystal growth is driven by two main factors: the diffusion of monomers to the particle surface and the reaction of monomers on the surface. The flux of monomers J_d passing by a particle and the reaction rate J_r of monomers at the solid–liquid interface are given by *Equation 3.5* and *Equation 3.6*:[134,135]

$$J_d = 4\pi D r (C - C_i) \quad (3.5)$$

$$J_r = 4\pi k_d r^2 (C_i - c_r) \quad (3.6)$$

where D is the diffusion constant of monomers in the solution, k_d is the rate constant of a deposition reaction, C_i is the monomer concentration on the particle surface, and c_r is the solubility of the particle in the solution.

Depending on whether the growth is controlled by the diffusion or the reaction process, the growth rate R_g can be approximately expressed as:

$$R_g = \frac{D V_m}{r}(C - C_i) \quad (3.7)$$

$$R_g = k_d V_m (C_i - c_r) \tag{3.8}$$

More precisely, the growth mechanism is usually a combination of the two factors. Therefore, the following generalized equation that considers both processes, as well as the dependance of the particle solubility on its radius, was proposed to give a more exhaustive description of the phenomenon:[136]

$$R_g = \frac{r'}{t'} = \frac{S - e^{\left(\frac{1}{r'}\right)}}{r' + Ke^{\left(\frac{\alpha}{r'}\right)}} \tag{3.9}$$

with

$$r' = \frac{RT}{2\gamma_S V_m} r \tag{3.10}$$

$$t' = \frac{R^2 T^2 DC}{4\gamma_S^2 V_m} t \tag{3.11}$$

$$K = \frac{RT}{2\gamma_S V_m} \frac{D}{k_d} \tag{3.12}$$

where t is time, α is the transfer coefficient of the activated complex, and R is the ideal gas constant.

K is a parameter called Damköhler number and it indicates whether the growth is driven more by the diffusion or the reaction process.

In the third stage of the NC synthesis, the crystal growth is stopped, and the resulting samples are collected by centrifugation. Removing the NCs from the precursor solution is a necessary step to prevent changes in their size and morphology. In fact, when they are left in the solution, they can undergo a phenomenon known as Ostwald ripening.[137] As the

temperature and the monomer concentration are lowered, the critical radius increases and alters the equilibrium of the system. As in the case of nucleus growth, the nanocrystals with a radius smaller than r^* begin to dissolve, while the others continue to grow. This leads to a general increase of the average size of NCs and a defocusing of their size distribution.

To remove any trace of the precursor solution and excess ligands, the crystals can be dispersed in a weak solvent and centrifugated again for several times. This washing process has a not indifferent importance because solvent and ligands, being typically long organic molecules, can interfere with electrical conduction and, consequently, affect the performance of electronic devices fabricated with the NCs.

3.2 Electronic Structure

As previously mentioned, when at least one dimension of a solid is reduced to the nanoscale, namely below 100 nm, it starts to exhibit novel, and often unpredictable, features that are not observed in its usual bulk form. The different structural, mechanical, thermal, and chemical properties that appear upon size reduction are mainly due to the increasing surface–volume ratio and the smaller diameter of the crystal grains, whereas the new optical and electrical properties are the result of a modification of the electronic band structure of the material.[25,138] This alteration of the energy bands is a purely quantum-mechanical phenomenon called quantum confinement and it can be understood using the well-known model of the particle in a box.[139] In this modeling, a point particle with mass m is constrained inside a one-dimensional infinite potential well of width L, as depicted in *Figure 3.2 A*. Considering the potential V, the time-independent Schrödinger equation of such a system is given by *Equation 3.13*:

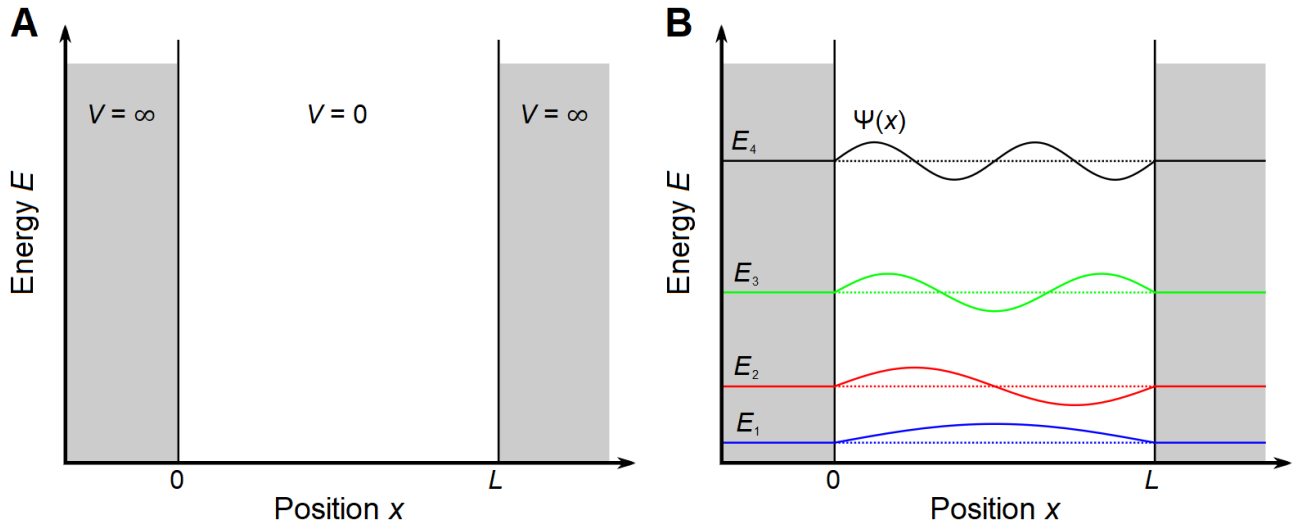

Figure 3.2 (**A**) Schematic illustration of an infinite potential well with width L in one dimension, also called box. (**B**) Schematic illustration of the energy levels and wavefunctions of a particle in a one-dimensional infinite potential well.

$$-\frac{\hbar^2}{2m}\frac{d^2\Psi}{dx^2} + V\Psi = E\Psi \tag{3.13}$$

with

$$V(x) = \begin{cases} \infty, & x \leq 0 \\ 0, & 0 < x < L \\ \infty, & x \geq L \end{cases} \tag{3.14}$$

$$\begin{cases} \Psi(0) = 0 \\ \Psi(L) = 0 \end{cases} \tag{3.15}$$

where ψ is the wavefunction of the particle, E is the energy of the particle, x is the position in one dimension., and $\hbar$ is the reduced Planck constant.

Equation 3.15 represents the boundary conditions that ψ must satisfy at the edges of the potential well, which mean that the probability of the particle escaping the box is zero. With these assumptions, the Schrödinger equation can be solved analytically, and the resulting

energy values are given by the following formula:

$$E_n = n^2 \frac{\pi^2 \hbar^2}{2mL^2} \tag{3.16}$$

where *n* is an integer number.

This simple model shows that when a particle is confined, like in the case of charge carriers in a nanomaterial, its energy can no longer vary with continuity but becomes quantized in discrete levels (*Figure 3.2 B*).

This phenomenon can be understood also considering how the energy bands originate in semiconductors. When two atoms bind together to form a molecule, their atomic orbitals are combined to generate a bonding and an antibonding molecular orbital, as described by the linear combination of atomic orbitals (LCAO) approach. As further atoms are added to the molecule, more molecular orbitals are formed, and the energy separation between two consecutive bonding or antibonding states becomes increasingly smaller. In the case of a macroscopic crystal, whose number of atoms is of the order of the Avogadro number, this separation is so narrow that the molecular orbitals basically merge into a continuum of energy, namely a band. In the case of NCs, instead, the opposite process occurs. Due to the reduced size, they consist of a relatively small ensemble of atoms, typically ranging from 10^2 to 10^4 units depending on the crystal size. In fact, these nanomaterials can be imagined as giant molecules. Therefore, their electronic bands separate again into the constituting orbitals, and distinct energy levels appear (*Figure 3.3*).[140]

The particle-in-a-box model is well suited to describe two-dimensional systems in which the quantum confinement occurs only in one direction, such as nanoplatelets or quantum wells, but it can be extended analogously to also treat systems with a different dimensionality. In the case of a zero-dimensional nanomaterial, indeed, the charge carriers are confined in all three directions, therefore they can be modelled as particles in a sphere surrounded by an infinite potential rather than in an infinite square box.[139] Solving the Schrödinger equation in this representation, the energy of the particles is found once again to be quantized and its levels

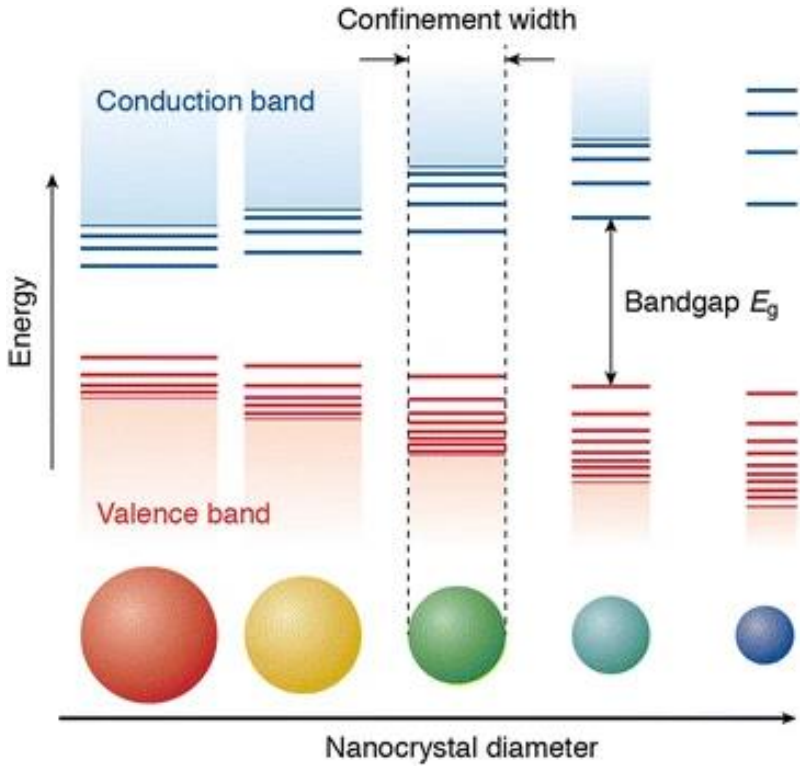

Figure 3.3 Schematic illustration of the effects of quantum confinement on the electronic band structure of semiconductors. As the size of a crystal decreases, its energy bands start to separate into individual quantized levels. Adapted from ref [140].

are given by:

$$E_{l,n} = \frac{\hbar^2 \phi_{l,n}^2}{2mr^2} \tag{3.17}$$

where l is an integer number, r is the sphere radius, and $\phi_{l,n}$ is the n-th root of the spherical Bessel function of order l.

It is worth to note that the dimensionality of nanomaterials refers to their morphological dimensionality, which is defined by the number of dimensions that are not subjected to confinement and is completely independent from the concept of structural dimensionality introduced to describe the lattice of perovskite derivatives.

In the case of NCs, the Coulomb interaction between electrons and holes must also be considered when studying their electronic band structure. The energy of this interaction is of the order of $e^2/\varepsilon r$. Since it scales as $1/r$ whereas the confinement energy grows as $1/r^2$, the effects of the Coulomb interaction become decreasingly relevant compared to those of quantum confinement as the size of the crystals is reduced.[30,141] The key parameter to investigate this phenomenon in semiconductor NCs is the exciton Bohr radius a_B. When $r \gg a_B$, the system is in a weak confinement regime. In this condition, the electrostatic interaction prevails, the electron and hole bind together to form an exciton which, subsequently, is confined by the reduced crystal dimensions. The exciton energy E_{ex} is given then by *Equation 3.18*:[142]

$$E_{ex} = E_g^0 - E_b + \frac{\pi^2 \hbar^2}{2M^* r^2} \tag{3.18}$$

where $E_g{}^0$ is the gap energy of the bulk semiconductor, E_b is the exciton binding energy, and M^* is the effective translation mass of the exciton.

When $r \approx a_B$, the system is in an intermediate confinement regime. Assuming that the hole effective mass is bigger than the electron effective mass, the hole appears localized at the center of the nanocrystal and moves in the average potential generated by the electron, which instead moves much faster. The region of the hole motion around the NC center is much smaller than r, hence the dependence of E_{ex} on the crystal size can be described as the behavior of a donor localized in the same position of the hole.

Finally, when $r \ll a_B$, the system is in a strong confinement regime. In this case, the quantum confinement dominates, therefore the electron and hole are individually subjected to the energy quantization and the Coulomb interaction only slightly modifies their energy levels. The gap energy of the NCs E_g is given by the Brus equation including the correction for the spatial correlation effect:[143,144]

$$E_g = E_g^0 + \frac{\pi^2 \hbar^2}{2\mu^* r^2} - A\frac{e^2}{4\pi\varepsilon r} - BE_b \tag{3.19}$$

where μ^* is the effective reduced mass of the exciton, and A and B are numeric constants.

The first additive term on the right side of *Equation 3.19* represents the confinement energy. The following terms, instead, represent respectively the first- and second-order corrections calculated in perturbation theory due to the Coulomb interaction and the spatial correlation between electron and hole. This shows that the exciton effect persists even in the limit of zero dimension because the electrostatic interaction grows as $1/r$ as the crystal size is reduced, hence it diverges for r tending to 0.

Equation 3.18 and *Equation 3.19* show how the size of nanocrystals has a huge impact on their gap and exciton energy, however their dimensionality also plays a role in the modulation of the material properties. Changes in the dimensionality, in fact, have a strong effect on the density of states (DOS) of the electronic bands.[139] In bulk semiconductors, the DOS has a square root dependence on the energy, as depicted in *Figure 3.4*.[140] In the case of 2D nanomaterials, the DOS shows a stepped profile, namely the energy is a continuum but increases by discrete steps, whereas the DOS remains constant between one step and the next. In the case of 1D nanomaterials, instead, the energy grows again in discrete amounts, but the DOS presents an inverse square dependence on it and decreases rapidly between every steps.

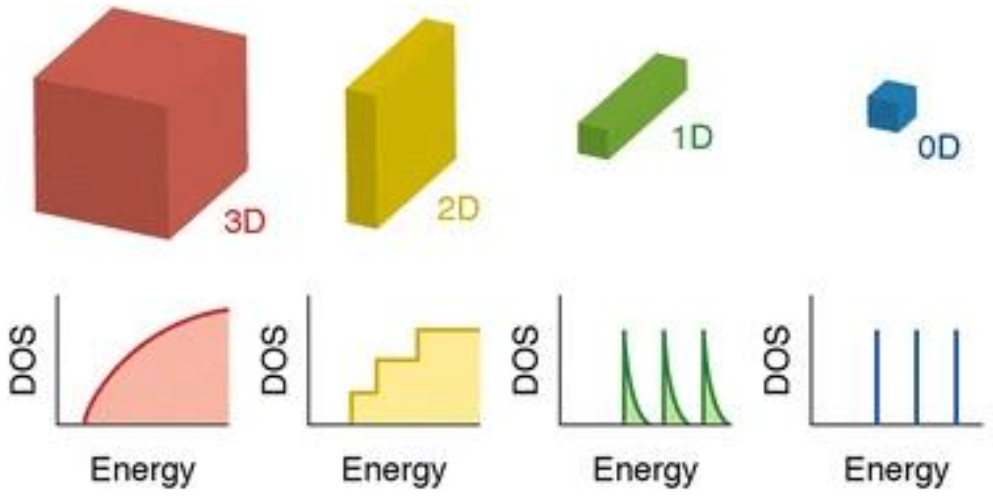

Figure 3.4 Schematic illustration of the effects of reduced dimensionality on the density of states of the energy bands in a semiconductor. Adapted from ref [140].

Finally, for 0D nanomaterials, the energy is completely quantized in levels and the states are allowed only for energies of these levels, therefore the DOS exhibits a comb-like profile.

3.3 Optical Properties

3.3.1 Bandgap Tunability

One of the most promising properties of metal halide perovskites is the possibility to tune their gap energy, and thus their absorption and emission wavelengths, over the entire visible range, from UV to near IR. This can be realized by varying their composition or, in the case of nanomaterials, modifying their size.[35,36,145]

The chemical composition of perovskites can be controlled directly from the synthesis of the crystals. MHPs displaying a blended composition of either cations or anion can be

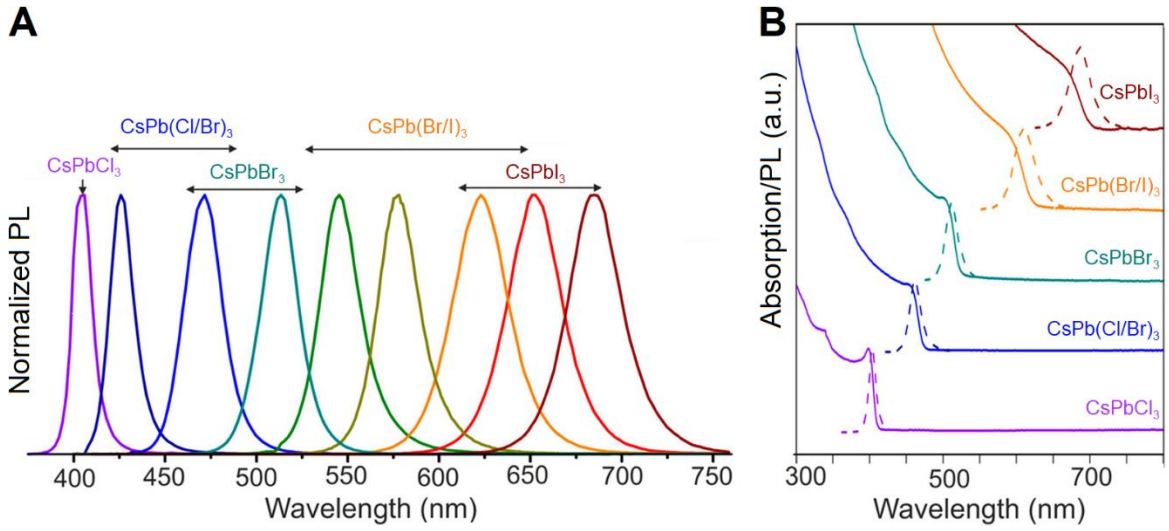

Figure 3.5 (**A**) Normalized emission of $CsPbX_3$ nanocrystals (X = Cl, Br, I). (**B**) Absorption and photoluminescence spectra of $CsPbX_3$ nanocrystals (X = Cl, Br, I). Adapted from ref [34].

achieved by combining, from the start of the reaction, different ion precursors with variable molar ratio. Adjusting the ratios between the constituents it is possible to continuously tune the bandgap to any energy value in the visible range, thus enabling the creation of materials with properties fit for any purpose (*Figure 3.5*).[34,146,147]

It is also possible to alter the chemical composition of perovskite NCs after the synthesis is completed through an ion-exchange process, namely a chemical reaction that substitutes the already present ionic species with new ones (*Figure 3.6*).[148] While cation-exchange processes are already routinely applied to standard semiconductor nanocrystals, anion-exchange techniques are hardly employed. In the case of anions, in fact, the ion substitution is hampered due to their bulkier nature and the stronger bonding of their sublattice.[149,150]

In the case of LHP NCs, on the contrary, ion-exchange reactions can be successfully executed with ease on both cations and ions[35,36]: they are simply achieved by combining the selected ion precursors with NCs in suspension. The great effectiveness of ion-exchange

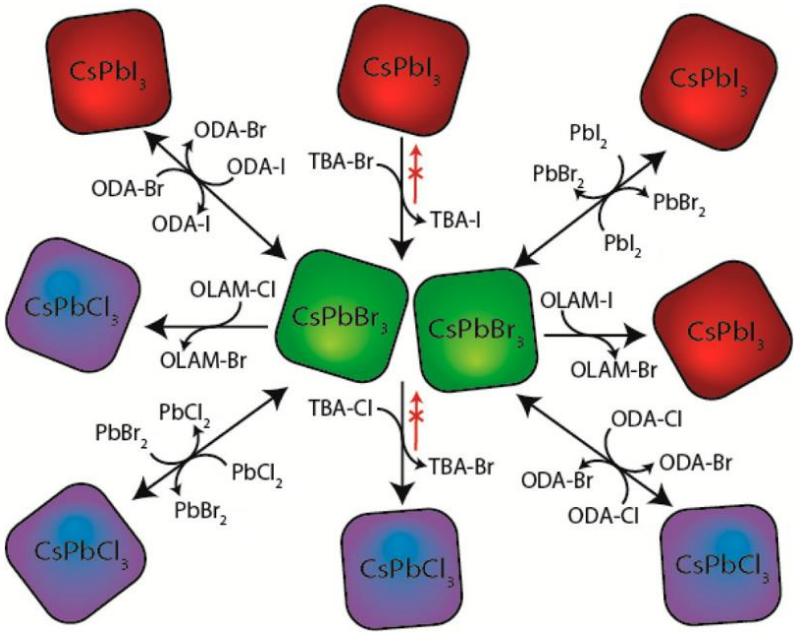

Figure 3.6 Schematic representation of the ion-exchange process. Some compounds enable the exchange of different halides and so they allow to obtain alternatively one perovskite from another. Other compounds, instead, are selective only for specific ions and therefore the reaction can just occur in one direction. Adapted from ref [148].

reactions in these materials is related to the high mobility of the halides and their fast diffusion in solution combined with the soft ionic nature of the LHP lattice.[119,151,152] This method is particularly convenient because it allows to preserve the crystal size and morphology, therefore it enables, in principle, the formation of nanocrystals of any perovskite, even those that cannot be directly synthesized, by converting pre-existing NCs from a different, more easily synthesizable perovskite.

A further strategy commonly used to tune the bandgap of NCs is the modification of their size and dimensionality.[35,36] As in the case of traditional semiconductors, the basic concept of this technique is to control the quantum confinement arising from size reduction and exploit its effects to modulate the optical properties of the crystals (*Figure 3.7*).[34,153] For example, nanoplatelets of hybrid perovskite $MAPbBr_3$ were synthesized with a variable thickness ranging from five unit cells to just one single cell, and, as the number of octahedra layers decreases, a blue-shift of almost 100 nm in the PL emission was observed, thus revealing a strong quantum confinement.[154]

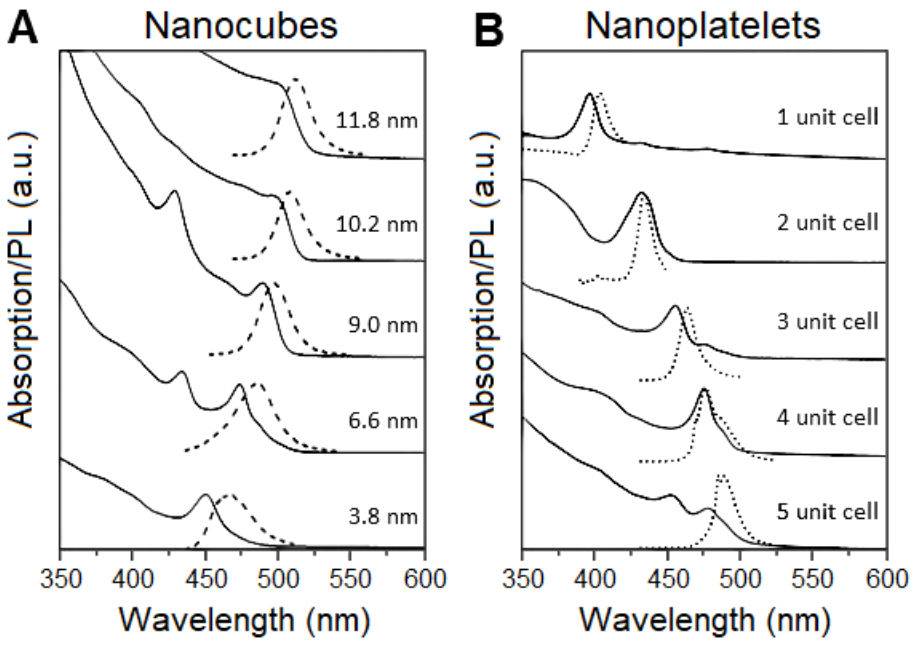

Figure 3.7 (**A**) Absorption (solid lines) and photoluminescence (dashed lines) spectra of $CsPbBr_3$ nanocubes with different size. Adapted from Reference [34]. (**B**) Absorption (solid lines) and photoluminescence (dashed lines) spectra of $CsPbBr_3$ nanoplates with different thickness. Adapted from ref [153].

The size and shape of NCs can be modified by varying the synthesis conditions. The reaction temperature, the reaction time, the nature of the ligands, the ratio between the precursors, and the ratio between the precursors and the ligands are all parameters that affect the crystal growth, therefore they can be exploited to achieve great control over the size and morphology of colloidal nanomaterials (*Figure 3.8*).[155,156] The effects of the ligands and the reaction temperature on the shape of LHP NCs were extensively investigated in the past and they are still a subject of great interest.[157] Amines and organic acids with different chain lengths have a different impact on the perovskites and can modify not only the size of the NCs but also their shape.

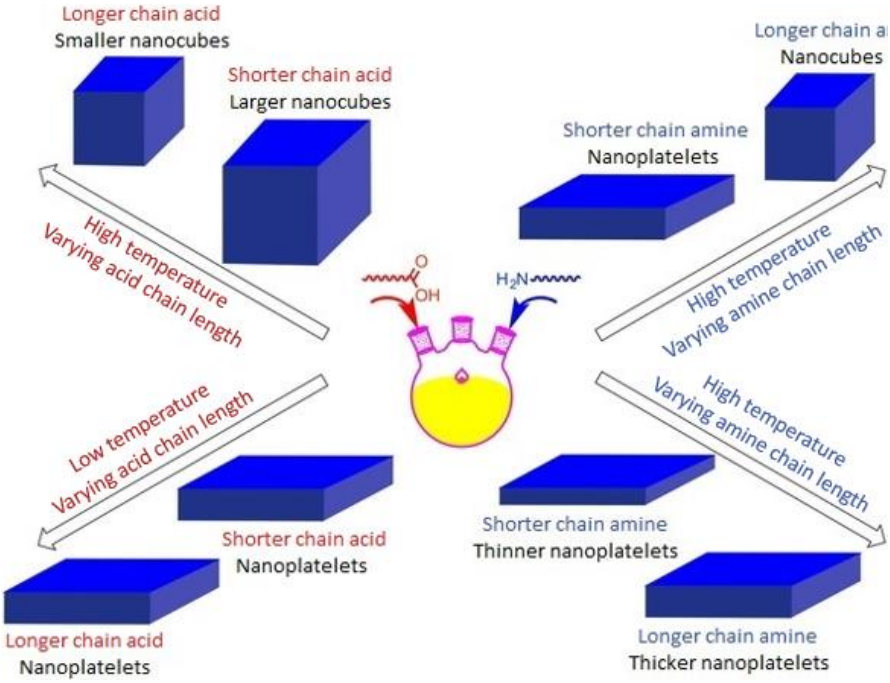

Figure 3.8 Schematic representation of the size and shape dependence of lead halide perovskite nanocrystals on the length of the ligand chain and the reaction temperature. Adapted from ref [155].

3.3.2 Photoluminescence

Besides color tunability, another of the most striking features of LHP NCs is the extremely bright photoluminescence (PL), quantified in terms of photoluminescence quantum

yield (QY). Several factors may influence this quantity, and, depending on the quality of the materials, it can even reach peak values of more than 95%.[35,158,159].

The photoluminescence of perovskite NCs has been object of extensive research to shed light on its origin. Both free charge carriers and excitons contribute to light emission, although the weight fraction of their contribution is unclear and, moreover, it appears to vary with temperature. At room temperature the effect of free carriers prevails, while at low temperature Wannier–Mott excitons seem to be the main responsible of the process.[35,160,161]

The efficient luminescence of LHP NCs occurs together with narrow emission linewidths, which reveal to be much narrower than those of many traditional semiconductor nanocrystals. Moving from blue to red, the PL full width at half-maximum (FWHM) ranges from 10 to 40 nm.[35,36] This feature originates from the fact that the emission line of LHPs is affected only by the homogenous broadening arising from the scattering with longitudinal optical phonons, whereas the inhomogeneous broadening is essentially negligible.[162,163] In the case of NCs, moreover, the PL linewidths are even narrower because the exciton–phonon coupling strength is decreased due to quantum confinement effects.[164,165] It is worth to note that when an emitter displays a narrow emission linewidth, namely it is characterized by what is called saturated emission, its color coordinates are closer to the edge of the CIE chromatic space.[166] Three emitters of complementary colors can span an entire color gamut, and the more saturated their emission is, the wider the gamut becomes. Thanks to these favorable properties, lead halide perovskite NCs appear then suitable materials for various light-emitting applications.

In addition, LHP exhibit a small Stokes shift, typically ranging from 20 to 85 meV, that increases as the size of the material is reduced. This phenomenon is attributed to the appearance of a confined hole state that tends to delocalize across the entire crystal, hence it shows a size-dependence on the radius of NCs.[167,168]

The spectral properties of colloidal NCs are influenced by several factors that may alter them, like self-absorption and Förster resonance electron transfer which depend on the nanocrystal concentration in suspension. To overcome the effects of these phenomena, and thus evaluate only the intrinsic emissivity of the nanomaterial, PL from single nanocrystals is widely employed. Surprisingly, the results obtained show no significant differences between

particle ensembles and single particles, thus demonstrating that LHP NCs are insensitive to this kind of phenomena.[145,169]

Another outstanding feature of these nanomaterials is the suppression of fluorescence blinking.[169,170] PL intermittency is a well-kwon phenomenon because it was previously documented for metal chalcogenide NCs whose properties are deeply affected by it. In these nanomaterials, in fact, the so-called "dark state" can last from some microseconds to several minutes.[171] Blinking is generally attributed to photoinduced cycles of charging and discharging of the nanocrystals, but the exact origin of these cycles is still not completely clear since the carrier dynamics in LHP NCs is very complex and a lot of radiative and nonradiative processes take place. Ionization of the nanomaterial and capture of charge carriers by photogenerated defect states are the two main mechanisms considered responsible for the intermittency of fluorescence.[171–173] The ionization of NCs happens when charges are moved from the crystal core to its surface or the surrounding environment. It can occurs through resonant quantum-mechanical tunnelling or non-resonant thermally activated ejection of photogenerated carriers, but it may also occurs via Auger ionization, namely the energy transfer from one recombined exciton to a second exciton that expels its electron or hole.[174] Regarding charge trapping, instead, the carriers are captured by shallow defect states activated by photons. In this situation, they can rapidly relax nonradiatively or interact with an exciton inducing its recombination through trion-mediated processes. In both cases, the charged state of NCs favors nonradiative recombination routes, thus suppressing the photoluminescence. When the charge is neutralized, the system returns to its normal state and the radiative recombination can occur again with the consequent emission of light.

3.4 Stability

3.4.1 Structural Stability

As previously mentioned in *Paragraph 2.1*, metal halide perovskites are typically characterized by different polymorphs.[175] This feature represents a potential issue for the materials because it undermines their structural stability, especially in the perspective of optoelectronic applications since the operating temperature of the devices may induce a phase transition in crystals that are otherwise stable under ambient conditions.[176,177] This problem is particularly pronounced in the case of iodide-based perovskites. At room temperature, $CsPbI_3$ and $FAPbI_3$ exhibit respectively orthorhombic and cubic 3D lattices that are, however, thermodynamically metastable, therefore they tend to reshape into 1D polymorphs that ensure a better stability (*Figure 3.9*).[178] Due to the reduction of structural dimensionality, this phase

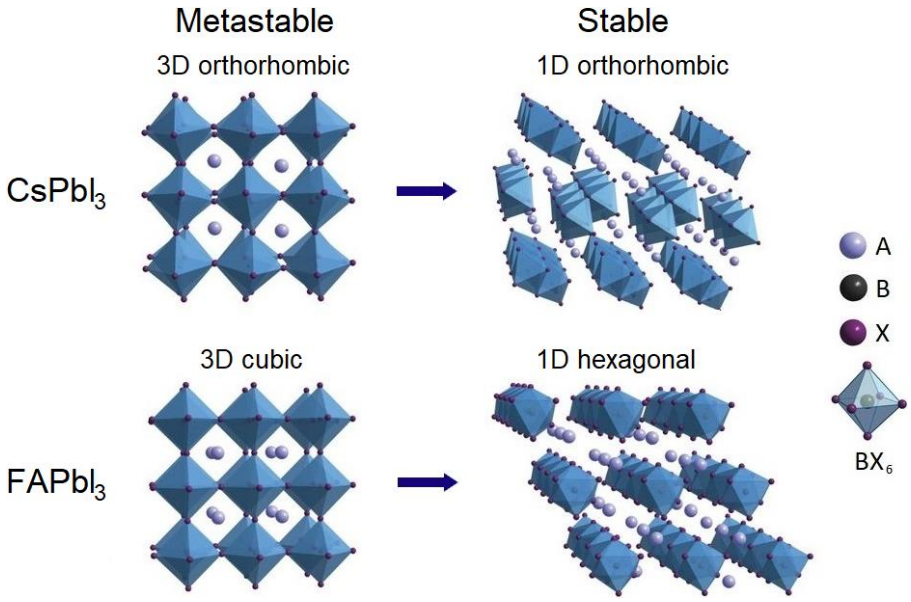

Figure 3.9 Schematic illustration of the phase transition in iodide-based perovskites. The 3D crystal structures of $CsPbI_3$ (orthorhombic) and $FAPbI_3$ (cubic) are metastable at room temperature and so they tend to turn into more stable 1D polymorphs. The reduction of structural dimensionality causes a widening of the bandgap of the two compounds, which is reflected by a change in their color from reddish black to yellow. Adapted from ref [178].

transition results in a shift of the gap energies, from near IR to the visible region, that consequently alters the optical properties of the materials and make them no longer suitable for the original purposes, especially in the case of light-harvesting applications.

The structural instability of iodide-based LHPs is to be attributed to the size of their A cation. Indeed, Cs and FA ions are, respectively, too small and too big to adequately fit into the A site of the 3D perovskite lattice. Besides, the determination of the tolerance factor for HOIPs is often a demanding effort because, due to the non-sphericity of the molecular cations and their hydrogen-bonding interactions with the surrounding lattice, it is very difficult to precisely establish their ionic radius. According to the best estimates of this parameter, the tolerance factor of lead iodide perovskites was reported to be 0.89 for $CsPbI_3$, 0.95 for $MAPbI_3$ and 1.03 for $FAPbI_3$.[68] These experimental data actually confirm that cesium- and formamidinium-based compounds fall right outside the cubic stability range and so are affected by structural lability, whereas the methylammonium-based ones are characterized by a more stable behavior.

The crystal lattice of MHPs can be stabilized by changing the chemical composition of the latter with the addition of new elements.[86,176] For mixed materials, the tolerance factor is computed by averaging over the different constituting ions, therefore it is possible to modify the initial value of *t* into the stability range. Changing the halide content is an effective way to strengthen the crystal structure. However, since the halogens have a deep impact on the electronic band structure of perovskites (see *Paragraph 2.2.1*), the most advantageous strategy to achieve stability is to mix the composition of the A site to tune the tolerance factor without altering the electrical and optical properties. For example, in the case of double-cation perovskites containing both cesium and formamidinium, this approach allows to successfully stabilize the materials because the detrimental contributions of Cs and FA ions counterbalance each other, while preserving the optimal optoelectronic features.[179,180] As concerns colloidal NCs, moreover, the composition can be easily adjusted post-synthetically through convenient ion-exchange procedures, as discussed in the previous paragraph.

In the case of polymorphic materials, size reduction to the nanoscale is another effective strategy to improve the stability of specific crystal phases. Due to high surface energy, the thermodynamics of nanomaterials is altered in comparison to their bulk counterpart and

so different crystal structures may appear more stable at room temperature.[181] In this regard, nanocrystalline LHPs reveal to have an enhanced stability of the 3D lattices, although the precise origin of this phenomenon is still unclear.[176,177,182] Besides from surface energy, the high surface micro-strain of nanocrystals may play a role in this process as well. In addition, ligands also contribute to the structural stabilization of LHP NCs because they reduce the freedom of ion redistribution, thus making lattice rearrangement more difficult, and alter the total free energy of the system through their binding with the crystals.[164,183]

Despite the improvement related to size reduction, it should be noted however that the stability timescale for iodide-based perovskite nanomaterials still remains very limited, ranging from few weeks to several months for $CsPbI_3$ and $FAPbI_3$ NCs, respectively.[179]

3.4.2 Chemical Stability

Another major challenge regarding metal halide perovskites concerns the chemical instability. Due to their low formation enthalpy, MHPs can be easily crystalized as well as they can be easily decomposed. Several environmental factors account for the lability of these compounds such as air, solvents, light irradiation, and heat.[37,176,177] The interactions with moisture, oxygen, and other chemical agents can also degrade their properties and morphology, worsening the material performances for commercial applications.

The chemical bonding of MHPs has a much stronger ionic component than that of conventional semiconductors. Therefore, their lattice appears quite soft and it can be easily disorganized or even broken under any weak exogenous attraction. Besides, the high ionicity of the bonding makes these compounds particularly unstable towards polar solvents, like water. In fact, humidity plays a key role in the long-term preservation of LHP properties, since water molecules can effectively break the chemical bonds between the $[PbX_6]^{4-}$ octahedra and the cations and ultimately convert the perovskites into PbX_2 and other volatile byproducts.[37,86,184] These phenomena are even worse in the case of NCs. Due to their high surface–volume ratio, the uncoordinated atoms on the surface of nanomaterials result in a huge density of dangling bonds. For this reason, NCs are extremely reactive and tend to readily react

with each other and any substance they come in contact with.[185]

Exposure to oxygen can impact MHP NCs through either oxidation or defect passivation, though only the former process wields a detrimental effect on the optical properties. $MAPbX_3$ perovskites are especially susceptible to oxygen degradation owing to their low formation energy, and they can easily decompose into PbX_2 and other compounds like CH_3NH_2, PbO_2, HX, or X_2.[186] This occurs in particular during the isolation and purification procedures. As stated above, the nanocrystalline form increases the instability of these materials because of the large surface area, and the concurrent action of other environmental factors like moisture, temperature shifts and irradiation can further boost the degradation.[184,187,188]

The chemical stability of solution-processed NCs, and nanomaterials in general, can be achieved by passivating their surface using capping agents. The ligands bind to the crystal surface curing the dangling bonds and consequently decreasing the reactivity of the material. This action is also essential for the synthesis of NCs because it prevents the particles to aggregate and react with each other during the growth phase, thus leading to the formation of crystals that are nanometric. In addition, the ligands form a shielding layer around the NCs that protects them from any external molecules. The effectiveness of this preservative action is influenced by the properties of the ligand molecules, such as length, branchness, anchoring groups, and steric effects.[48,189,190] The most common capping agents employed in the synthesis of NCs are amines and carboxylic acids[155,187]. When applied simultaneously, they were proved to produce excellent results in reducing the crystal instability, thus suggesting the presence of some sort of synergistic effect between the two species[191]. The mechanism behind the effectiveness of organic acids and amines combined in passivating and stabilizing NCs is still not completely clear. According to experimental evidence, a protonation transfer reaction is the most accredited hypothesis: the carboxylic acid moiety -COOH transfers a proton H^+ to the amino moiety $-NH_2$, producing charged carboxylate $-COO^-$ and ammonium $-NH_3^+$ groups that can bind, respectively, to the uncoordinated A and B cations and X anions on the facets of the NCs. This process successfully passivates the dangling bonds and stabilizes the crystals (*Figure 3.10*).

To further improve the chemical stability, nanocrystals can be encased with more

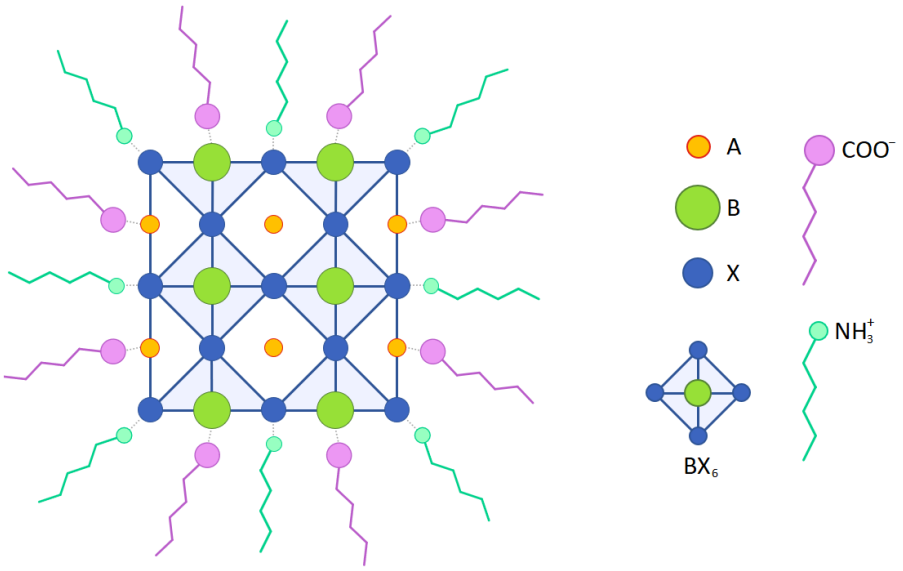

Figure 3.10 Schematic illustration of the binding between the ligand molecules and the surface of halide perovskite nanocrystals. The charged moieties -COO^- and -NH_3^+ respectively bind to the positive and negative ions on the surface of the crystals.

stable materials that are not affected by the surrounding environment.[37,176] Following the model of core–shell nanoparticles of traditional semiconductors, the most common technique to stabilize NCs is to coat them with a thin layer from a protective substance, like a metal oxide or a different semiconductor.[192] Alternatively, they can also be embedded into macroscopic matrices of stable materials such as oxides, inorganic salts, glasses, polymers and metal-organic frameworks.[193] This strategy was thoroughly investigated in the last years using different host compounds and it showed a satisfactory improvement in the chemical stability of perovskite NCs, especially against water.

3.4.3 Colloidal Stability

As previously described, ligands are essential to restore the dangling bonds of nanocrystals and passivate their surface, thus granting their chemical stability. Nevertheless, they also have another fundamental function because they enable control over the colloidal

stability of the crystals in suspension. The attractive force between two NCs derives from a van der Waals interaction originating from transient fluctuations in the electron distribution of the crystals.[194,195] Although the theory of the interatomic attraction at the nanoscale is very complex, this force can be expressed through a simplified representation using an effective pair potential *U* given by the following equation:

$$U = k\frac{\rho_1\rho_2}{d^6} \tag{3.20}$$

where *d* is the distance between the two interacting particles, ρ_i (i = 1, 2) is the density of atoms per unit volume of the particles, and *k* is a coefficient.

In general, the tendency to form aggregates depends on several factors and is determined by a balance between attractive and repulsive interparticle forces. When immersed in a good solvent for a given type of surface ligand, NCs evenly disperse in solution. However, the dynamic nature of the binding between the capping agents and the crystals can destabilize the suspension.[190,196,197] For example, the purification process of NCs may induce a fast detachment of ligand molecules from the crystal surface, leading to an irreversible loss of colloidal stability. Choosing a suitable ligand is then fundamental to guarantee the synthesis of nanomaterials and their chemical and colloidal stabilities.

Depending on the nature of surface ligands, NCs can form stable colloidal suspensions in polar or non-polar solvents. If the solvent quality is altered by a change of polarity, flocculation occurs. Colloidal stabilization can be achieved through two main processes: a steric repulsion and an electrostatic one.[195,198] In the case of sterically stabilized particles, the crystals are typically coated with long molecular chains, like hydrocarbons or neutral polymers, and the good solvents are associated to a negative free energy of chain–solvent mixing. The surfactant molecules repel each other, hindering the overlap between the ligand shells around the crystals and stabilizing therefore the suspension. On the other hand, the immersion in a non-solvent characterized by a positive chain–solvent mixing energy favors the contraction of the ligand molecules to minimize the contact with the surrounding material. This results in a

reduction of colloidal stability that consequently leads to the aggregation of the dispersed NCs. Non-polar liquids usually behave as good solvents for hydrocarbon-caped NCs, whereas polar liquids act as non-solvents. More generally, sterically stabilized NCs exhibit purely repulsive interactions when dispersed in good solvents, while in non-solvents or vacuum attractive interactions dominates at intermediate separations.

Electrostatic stabilization, instead, work through the incorporation of charged species on the NC surface. In this way, their surface charge is neutralized by the presence of oppositely charged ions diffused around the crystal. In this case, the best solvents are typically characterized by a high dielectric constant: the entropic penalty associated to the concentration of counterions in the diffuse double layer prevents the stabilized NCs from agglomerating. Adding a solvent with a low dielectric constant, namely bad screening properties, causes the collapse of the diffused counterion cloud, thus promoting aggregation.

Finally, it is worth to note that the use of hydrophobic or water-resistant capping agents successfully prevents the degradation of MHP NCs in polar solvents. This method is very useful to achieve a stable dispersion of the crystals in aqueous suspensions, which can be of primary importance for specific purposes regarding biological applications.[187,199]

Chapter IV
TIN(IV)-BASED PEROVSKITE NANOCRYSTALS

4.1 Introduction

As mentioned in *Chapter I*, the high toxicity of lead and the ease with which it can leak into the environment are the major disadvantages of lead halide perovskites. These compounds have proved to achieve great results in many fields, however the great risk they pose to the human health is an unsurmountable obstacle to their use in everyday life applications. For this reason, safer compounds containing different metals are of crucial importance for future research and widespread diffusion of perovskite-based technology.

Tin halide perovskites (THPs) seem to be a possible alternative to LHPs. Being the element just above Pb in Group 14 of the Periodic Table, tin has the same np^2ns^2 electronic configuration and a very similar ionic radius (1.19 Å for Pb^{2+} and 1.18 Å for Sn^{2+}),[200] therefore it satisfies the requirements of size, coordination, and charge balance to form a 3D perovskite structure.[201,202] Moreover, this metal presents a very limited toxicity in comparison to lead. Elemental tin, as well as its inorganic salts, has indeed mild effects on the human body and is hardly absorbed by it, so much so that it is commonly used in the fabrication of the containers for canned food and beverage.[39,203] However, it is worth noting that the regular exposure to high doses of Sn may still lead to poisoning and that some of its compounds, especially the

organometallic ones, are very toxic.[39,203,204] Besides the requirements of formability and safety, tin-based perovskites also exhibit electronic and optical properties equal if not better to those of LHPs, like high absorption coefficients, long carrier lifetimes and even superior charge carrier mobilities. In addition, due to the greater electronegativity of Sn, these compounds have narrower bandgaps in comparison to their Pb-containing counterparts, reaching values as low as 1.2 eV,[95,205] and so they appear to be potentially better light harvesting materials. For these reasons, tin appears to be the most natural and most promising choice to replace lead.

Tin halide perovskites, however, suffer from two major issues. The first problem is a high density of defects states that affects their emission properties. Contrary to lead-based compounds, in THPs the vacancies of B metal are proved to generate deep electronic states. Because of their low formation energy, this type of defect occurs in high concentrations in these materials and, consequently, their photoluminescence quantum yield is strongly limited by the resulting trap states that act as nonradiative recombination centers.[201,206] This issue is further worsened by the weaker spin–orbit coupling of Sn 5p states compared to Pb 6p states that makes the CB of tin-based perovskites less stabilized and, therefore, the compounds appear less defect tolerant.[207,208]

The second problem of THPs is a severe chemical instability that heavily undermines their physical properties. Under ambient conditions, indeed, Sn^{2+} tends to quickly oxidize turning into Sn^{4+}, as described by the following equations:

$$Sn^{2+} \rightarrow Sn^{4+} + 2e^{-} \tag{4.1}$$

$$Sn^{4+} + 2e^{-} + O_2 \rightarrow SnO_2 + 2h^{+} \tag{4.2}$$

This phenomenon could be explained through some thermodynamic considerations. The redox potential of the reaction expressed in *Equation 4.1* is very small (0.15 V), so it suggests that the oxidation state 4+ may appear more stable under certain conditions and hence the state 2+ can turn into that with relative ease. Recent findings, in fact, indicate that this transformation can occur even in the absence of oxygen.[209] To make a comparison, the redox potential of the same reaction involving Pb^{2+} and Pb^{4+} is 1.67 V, way higher than tin, and

therefore lead reveals to be much more stable in the state 2+ and it does not undergo oxidative processes. This transition is detrimental for THPs because it leads to the formation of crystal defects that compromise the stability of their structure and the architecture of their eventual devices. Moreover, the defects introduce trap states in the electronic band structure that irreversibly deteriorate the emissive properties of the materials. The oxidation reaction occurs in every tin-based sample regardless of the dimensionality, but in the case of NCs it is even faster due to their high surface–volume ratio that speeds up the reaction.

The first synthesis of luminescent $CsSnX_3$ nanocrystals (X= Cl, Br, I) was reported in 2016.[210] Adapting the synthetic procedures previously reported for LHPs, researchers demonstrated the tunability of the optical properties of the crystals by modulating their chemical composition through both direct synthesis and post-synthetic anion exchange. The NCs, however, proved to have extremely low quantum yields (less than 0.15%) and poor chemical stability: they retained the emission from few minutes when exposed to ambient conditions to few days when stored in a glovebox with inert atmosphere. Such problems represent a serious setback for these compounds because they exclude the possibility of any application in optoelectronic devices. For this reason, research on THP NCs did not flourish much over the years and the studies on these nanomaterials are still very limited.

To overcome the problem of oxidation, a possible solution is to use tin(IV) directly in place of tin(II). Due to the different oxidation state of the metal, this substitution modifies the regular perovskite structure to maintain the charge neutrality of the crystal and leads to the formation of a so-called vacancy-ordered double perovskite, characterized by the general formula A_2BX_6. The structure of these new compounds is obtained from the standard perovskite lattice by removing alternatively half of the BX_6 octahedra, namely half of the B sites are occupied by the now tetravalent metal ion whereas the adjacent sites are empty, as shown in *Figure 4.1*.[211] The formula of these perovskite derivatives can also be expressed as $A_2\square BX_6$ or, alternatively, $A(\square_{1/2}B_{1/2})X_3$, where $\square$ represents a vacancy. With this rewriting, it is easy to understand why these compounds are called vacancy-ordered double perovskites: compared to the general formula ABX_3 of 3D perovskites, indeed, their constituting ions appear doubled

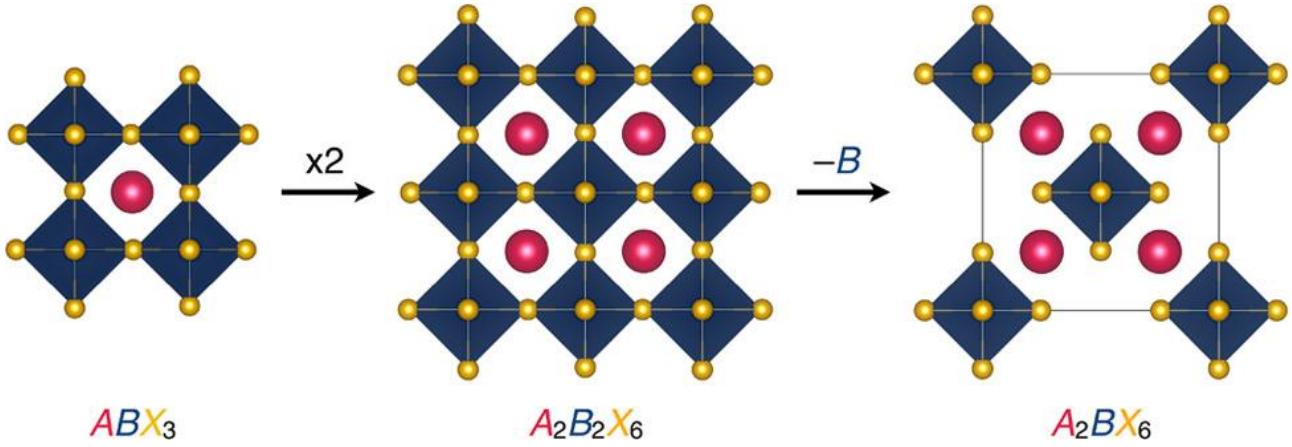

Figure 4.1 Schematic illustration of the crystal structure of 0D vacancy-ordered double perovskites and how it is obtained from the 3D lattice of standard perovskites. Adapted from ref [211].

while half of the B ions are replaced with vacancies. In such a configuration, the octahedra are isolated from each other, therefore, as discussed in *Paragraph 2.1*, these crystals can be classified as 0D perovskites.

At present, there are still very few studies on tin(IV)-based compounds in the form of colloidal nanocrystals and their results are sometimes contradictory.[212–215]. The earliest report on this family of nanomaterials dates back to 2016, when Wang et al. synthesized NCs of Cs_2SnI_6 with different shapes.[212] The synthesis and purification of the crystals were performed under ambient conditions and, after one week of storage in the same conditions, they did not show any degradation of the optical properties. These results indicate a clear enhancement in the chemical stability of tin(IV) halide perovskite NCs compared to their tin(II)-based counterpart, however their quantum yield was still very low, reaching peak values of less than 1%. This observation is in strict contradiction with previous theoretical studies claiming the defect-tolerant nature of bulk Cs_2SnI_6[216] and suggests that light emission from Cs_2SnI_6 nanomaterials depends on more complex factors that are not completely known yet and require further investigations to be fully unraveled.

In the following paragraphs, the synthesis and characterization of colloidal nanocrystals of Cs_2SnX_6 (X = Cl, Br, $Br_{0.5}I_{0.5}$, I) are reported.

4.2 Synthesis

Cs_2SnX_6 NCs (X = Cl, Br, I) were synthesized using a hot-injection (HI) method adapted from previous works on tin halide perovskites and their derivatives with tin(IV).[210,212,214] The HI method is a solution-based bottom-up synthetic procedure that was developed and exploited in the past for conventional semiconductor nanocrystals.[217] Owing to its ease and versatility, it has currently become one of the most commonly used technique to synthesize perovskite NCs.[36,218] The basic principle of this method is to combine all the reagents, except one, with the solvent and ligands to form a precursor solution. The mixture is then heated up to the reaction temperature and, when it reaches the desired value, the last reagent is swiftly injected into it. This rapid addition instantly triggers a burst of nucleation which is subsequently followed by the growth of NCs, as described by LaMer model (see *Paragraph 3.1*). Finally, the solution is quickly cooled down to room temperature with an ice water bath to stop the crystal growth and the product is collected and purified by centrifugation (*Figure 4.2*). The key parameters that allow to control the size and shape of the NCs are the reaction time, the reaction temperature, the injection temperature of the last reagent, the ratio between the precursors, and the ratio between the precursors and the ligands.

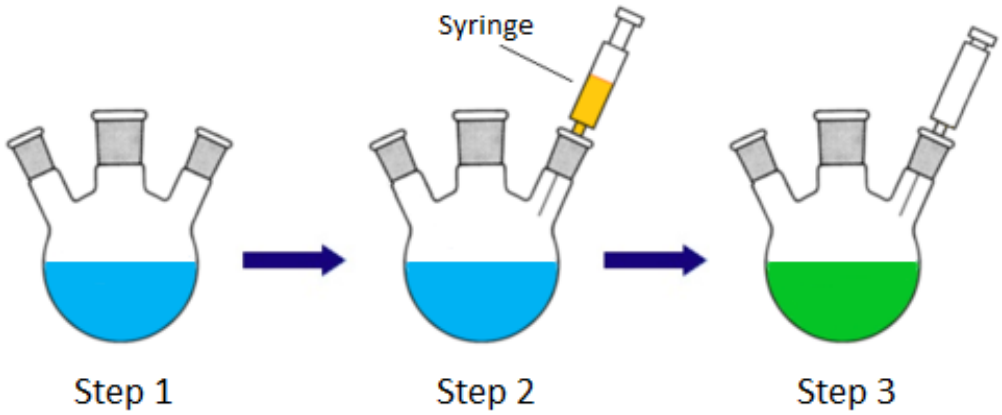

Figure 4.2 Schematic representation of the hot-injection method. In the first step the precursor solution is prepared. In the second step the final reagent is swiftly injected into it. In the third step the resulting suspension is cooled down to stop the synthesis and centrifugated to collect the nanocrystals.

The syntheses of Cs_2SnX_6 NCs were conducted in octadecene (ODE) using oleic acid (OA) and oleylamine (OLA) as capping agents, and tin(IV) halides and cesium oleate (Cs-oleate), that was synthesized as well, as perovskite precursors. After a process of trial and error, the following procedure was developed: at first, 5 mL of ODE, 0.2 mL of OA, and 0.2 mL of OLA are combined in a 50 mL three-neck flask and dried under vacuum for 1 hour at 120 °C. Subsequently, 0.235 mmol of SnX_4 (0.0611 g of $SnCl_4$, 0.1028 g of $SnBr_4$ and 0.1468 g of SnI_4) is added to the flask and the solution is degassed under vacuum for 15 minutes at 80 °C. In the case of mixed-composition NCs, an equimolar ratio of $SnBr_4$ and SnI_4 is used. The flask is then heated up at 220 °C under nitrogen flow and 1.5 mL of the as-prepared Cs-oleate solution is quickly injected with vigorous stirring. After a specific reaction time (15 seconds, 1 minute, 2 minutes, 10 minutes), the mixture is cooled down in an ice bath. To purify the NCs, the mother solution is then centrifugated at 7000 rpm for 5 minutes and the resulting supernatant is discarded. Some of the precipitated crystals are deposited on glass slides and covered with coverslips for future measures, while the remaining are dispersed in 5 mL of hexane (Hex). All the synthetic and purification processes were conducted under ambient conditions and no argon-filled glovebox was used to store the final samples.

At the beginning, the goal was to develop a synthetic procedure able to yield luminescent nanocrystals, so the efforts focused only on Cs_2SnI_6 NCs taking advantage of the previous literature on them. Once these crystals were obtained with the desired qualities, the next step was to extend the procedure to the entire halide series by replacing the halogen source.

Initially, the amount of SnI_4 used in the syntheses was smaller and the drying process of the precursor solution was performed at 100 °C for 1 hour. With these parameters, the synthetic procedure only led to the formation of CsI, thus suggesting that the ratio between cesium and tin was not correct for the crystallization of the perovskite. Besides, it was noticed that during the drying phase some red-orange spots tended to form around the necks of the flask. A sample of the material was collected and subsequently analyzed by X-ray diffraction (XRD) measurements, revealing that the spots were made of SnI_4. This discovery offered an explanation to the ineffectiveness of the synthetic procedure: being a volatile compound, SnI_4 escaped from the heated solution during the drying phase, thus causing a deficiency of tin that

eventually favored the crystallization of CsI. To overcome this problem, the drying process was conducted for a shorter time and at lower temperature, while the amount of SnI_4 was increased by 50% to perform the reaction in high excess of tin. With these changes, the new synthetic strategy successfully led to the formation of Cs_2SnI_6 NCs and it also proved to be suitable for the other halide perovskites.

4.3 Results

4.3.1 Structural Characterization

The crystal structure of the samples was investigated by X-ray diffraction measurements, and the resulting powder patterns are shown in *Figure 4.3*. All the samples appear to have a single phase that can be indexed according to the cubic Fm-3m space group (225), as previously reported for Cs_2SnI_6 and Cs_2SnCl_6.[212,213,215,219] By a simple visual inspection of the main reflection, namely the (222), a shift towards higher angles passing from Cs_2SnI_6 to Cs_2SnCl_6 is clear, thus indicating a reduction of the cubic cell size when I is replaced with Br, and Br with Cl. The trend of the cubic lattice parameter *a* determined for the four samples is reported in *Figure 4.4 B*, showing a significant change from 11.642(2) Å for Cs_2SnI_6 to 10.391(2) Å for Cs_2SnCl_6 with a reasonable linear scaling as a function of composition.

XRD measurements also demonstrate that the mixed-composition perovskite can be obtain with the synthetic procedure reported in *Paragraph 4.2*. However, there is a slight discrepancy between the experimental data and the reference. According to the calculated pattern, the (222) peak should occur at 27.36 degrees, while in the present sample it is at 27.72 degrees. Besides, the lattice constant *a* is estimated to be 11.140(2) Å in contrast to the value of 11.2819 Å reported in literature.[220]

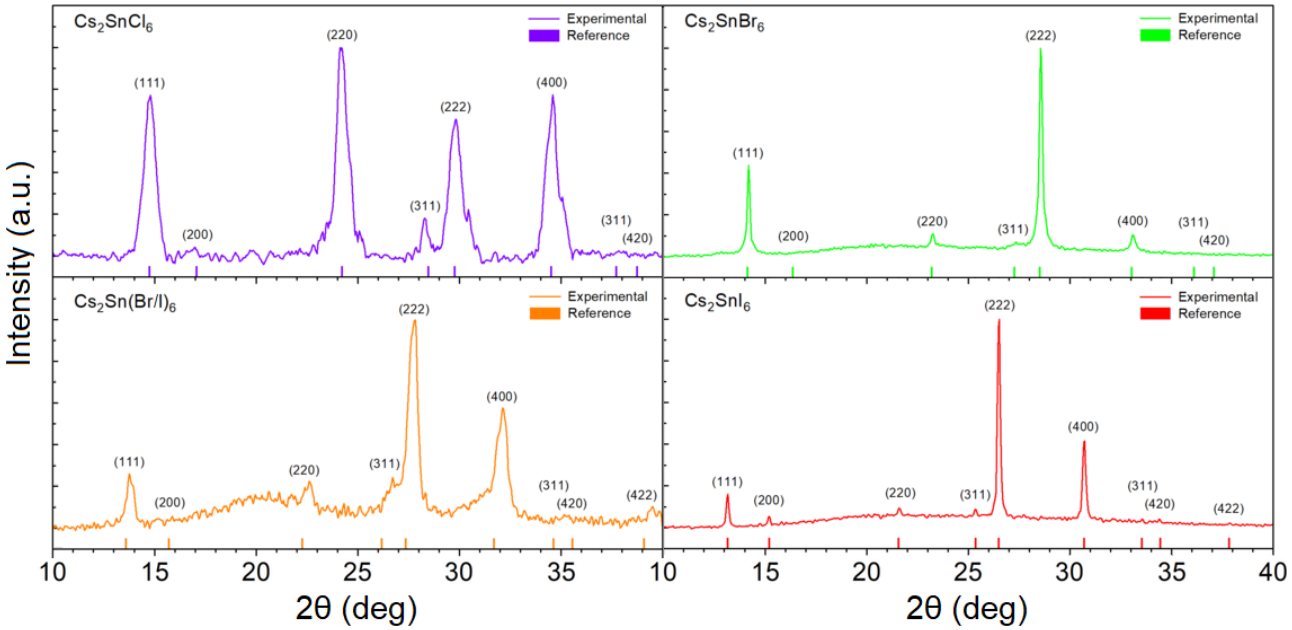

Figure 4.3 Indexed X-ray diffraction patterns of Cs_2SnX_6 nanocrystals (X = Cl, Br, $Br_{0.5}I_{0.5}$, I). The vertical bars in each pattern refer to the calculated cubic structure.

This discrepancy can be attributed to a variation in the perovskite composition: the volatile nature of SnI_4 could have caused a reduction in the quantity of this precursor during the synthesis, thus leading to the formation of NCs with a lower content of iodine. According to Vegard's law, the lattice constant *a* of solid solutions varies linearly with the concentration of solute *x*.[221] Therefore, a linear relation between *a* and *x* can be extrapolated from the experimental data and used to calculate the iodine content in the mixed-composition NCs. From the estimated value of their lattice constant, an iodine concentration of ∽40% is found, that is in fact lower than the expected value of 50%.

4.3.2 Morphological Characterization

Transmission electron microscopy (TEM) was employed to examine the morphology of the crystals. The investigation reveals the presence of spherical NCs with an average particle diameter *d* of about 3.2 nm for all the Cs_2SnX_6 compounds, except for the Cs_2SnCl_6 perovskite.

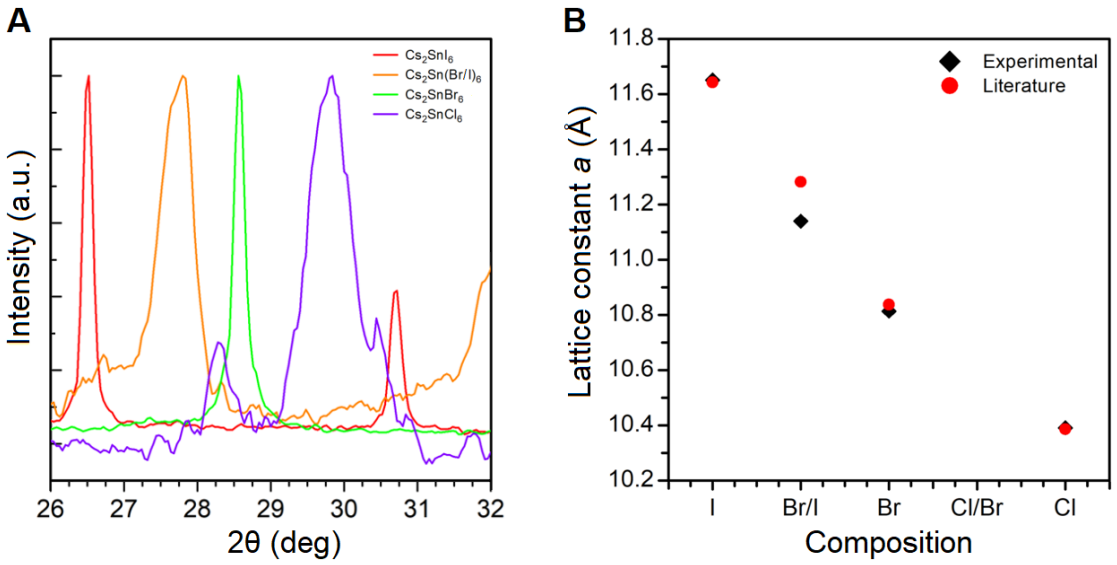

Figure 4.4 (**A**) Pattern zoom in the region around the (222) reflection for Cs_2SnX_6 nanocrystals (X = Cl, Br, $Br_{0.5}I_{0.5}$, I) highlighting the peak shift from higher to lower angles as the halide varies from Cl to I. (**B**) Trend of the cubic lattice parameter as a function of chemical composition for the Cs_2SnX_6 samples.

This material, in fact, shows a greater particle size of about 6.4 nm. Such values of *d* are similar or smaller than those previously reported in literature for Cs_2SnI_6 and Cs_2SnCl_6 NCs.[212–214,219,222] *Figure 4.5* shows a representative TEM image of the Cs_2SnI_6 nanocrystals, while *Figure 4.6* presents the size distribution diagrams of the four samples with different chemical composition reacted for 1 minute. The distribution of the bromide- and iodide-based NCs are quite narrow and symmetric as well as for the mixed-composition sample, while the distribution of Cs_2SnCl_6 NCs appears much broader. The larger diameter and the wider size distribution of chloride-containing crystals may be related to the faster growth dynamics of this perovskite.

As reported in *Paragraph 4.2*, all samples were prepared by quenching the reaction after 1 min upon the injection of the Cs-oleate solution. Different quenching times were also explored by stopping the reaction of Cs_2SnI_6 NCs at 15 s, 1 min, 2 min, and 10 min after addition of the last precursor. The relative data on the size distribution are reported in *Figure 4.7*. Once again, the samples present a spherical shape with a diameter of about 2.9 nm for the reaction time of 15 s, and of about 3.2 nm for all the other times. TEM investigation on this series of

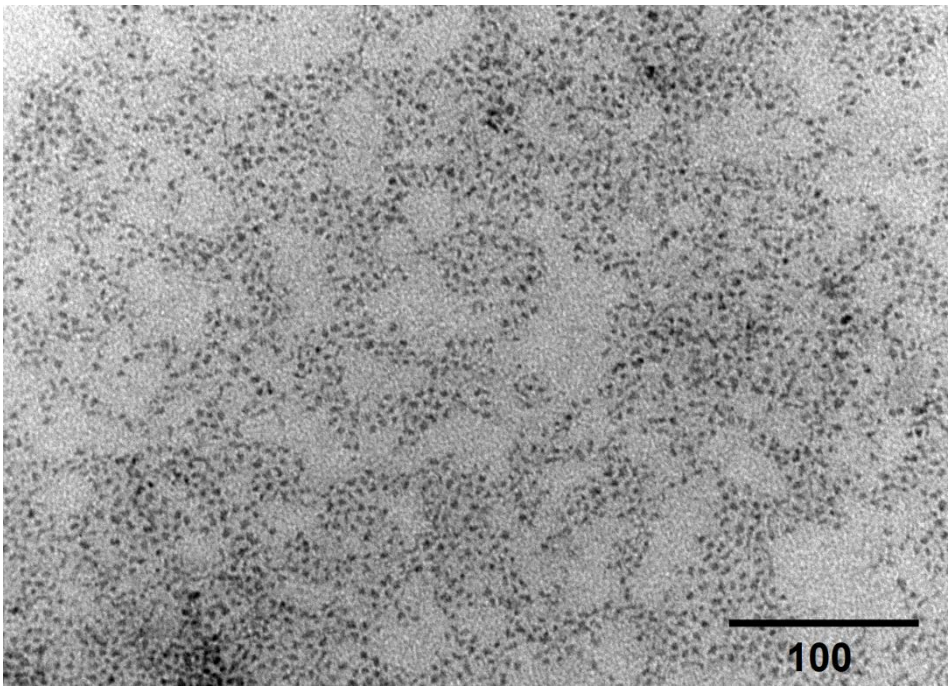

Figure 4.5 TEM image of Cs_2SnI_6 nanocrystals at 250kx magnifications.

samples indicate that the formation of NCs is fast and occurs within few seconds after the precursor injection, while the crystal growth, on the contrary, is slow and it requires long times to produce significant variations in the particle size. Besides, no variations in the morphology of the NCs are observed either, at least on the timescale explored.

The reduced growth rate can be attributed to the action of the ligands on the NC synthesis It was observed, indeed, that using smaller amounts of capping agents resulted in spherical crystals with a diameter of 15–20 nm.[214,215] This finding is coherent with previous works on Cs_2SnI_6 NCs reporting that no NCs were obtained when oleic acid was the only capping agent used during the synthesis, thus suggesting a suppressing action of this molecule on the crystal growth.[212]. Dolzhnikov et al., instead, carried out their syntheses without using any organic ligand and the samples prepared at 220°C were reported to have a diameter of about 38 nm.[213] In another work, Cs_2SnI_6 NCs were prepared using only oleic acid and no amine and they resulted with an average size of 10–15 nm.[215]

It should be also noted that a narrow size distribution is observed in almost all samples and for any reaction time, with standard deviations of about 0.6 nm, except for the sample

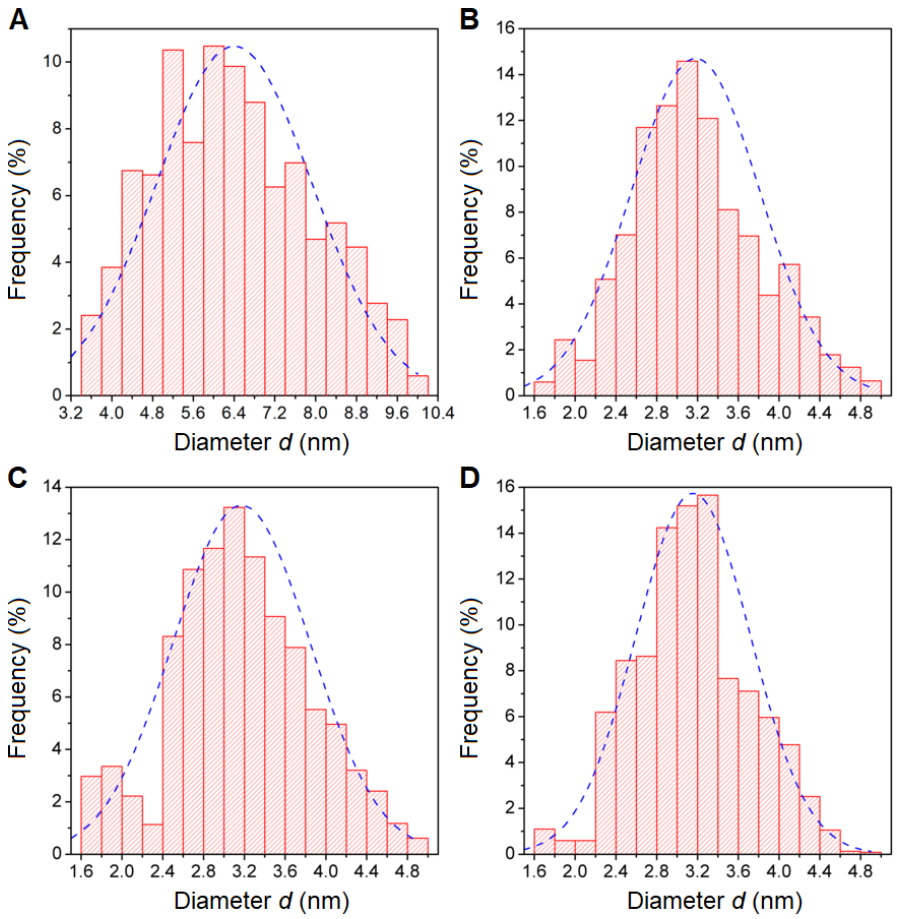

Figure 4.6 Size distribution histograms for nanocrystals of (**A**) Cs_2SnCl_6, (**B**) Cs_2SnBr_6, (**C**) $Cs_2Sn(Br_{0.5}I_{0.5})_6$, and (**D**) Cs_2SnI_6 quenched after 1 min.

whose reaction was stopped after 15 s (e.s.d. 1.2 nm), which in fact exhibits a significantly broader size distribution. This difference can be attributed to the general unevenness in the particle sizes right after the nucleation stage and the subsequent focusing during the crystal growth, as illustrated in *Paragraph 3.1*. Therefore, the good focusing of their size distribution for relatively longer reaction times together with their slow crystal growth can be very useful to achieve a good control over the diameter of tin(IV) halide perovskite nanocrystals.

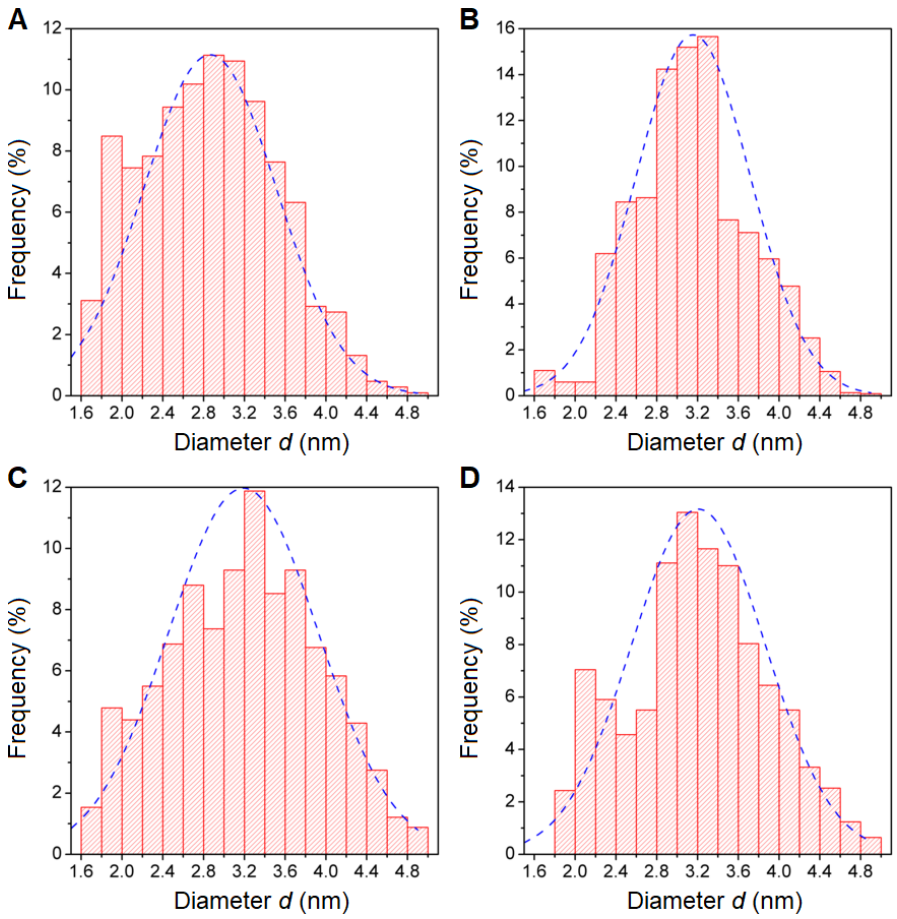

Figure 4.7 Size distribution histograms for $Cs2SnI_6$ NCs quenched after (**A**) 15 s, (**B**) 1 min, (**C**) 5 min, (**D**) and 10 min of reaction time.

4.3.3 Optical Characterization

The optical properties of Cs_2SnX_6 NCs (X = Cl, Br, $Br_{0.5}I_{0.5}$, I) were characterized by UV–Vis–NIR spectroscopy and steady-state photoluminescence (PL) spectroscopy. Unlike LHP nanomaterials, that usually display a sharp absorption edge, the absorption spectra of tin(IV)-based NCs are found to have a less distinct profile with a pronounced tail pushing toward longer wavelengths (*Figure 4.8*). In this regard, they are similar to the absorbance spectra of $CsSnX_3$ NCs (X = Cl, Br, I).[210]. These features were previously attributed to a sizable concentration of shallow electronic states arising from crystal defects, such as halide vacancies, which have a low formation energy and are believed to introduce such states right below the CB

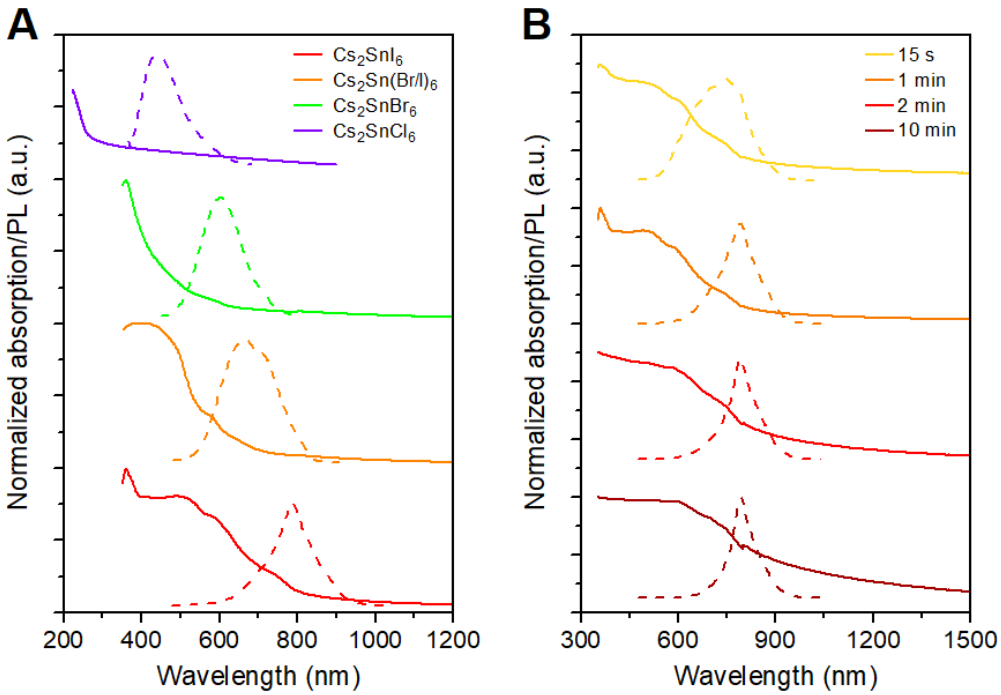

Figure 4.8 (**A**) Absorption (solid lines) and photoluminescence spectra (dashed lines) of Cs_2SnX_6 nanocrystals (X = Cl, Br, $Br_{0.5}I_{0.5}$, I). (**B**) Absorption (solid lines) and photoluminescence (dashed lines) spectra of Cs_2SnI_6 nanocrystals as a function of reaction time after Cs-oleate addition. (Curves were shifted vertically for clarity).

edge.[216,223,224]

The photoluminescence spectra of the NCs with different halide content are reported instead in *Figure 4.9 A*. Moving from Cl to I, the emissions are peaked at 444 nm (2.80 eV), 603 nm (2.06 e V), 663 nm (1.87 eV), and 790 nm (1.57 eV), with corresponding full widths at half maximum (FWHM) of, respectively, 117, 122, 165, and 112 nm. The values found for $Cs_2Sn(Br/I)_6$ and Cs_2SnI_6 NCs are considerably higher than the gap energies reported for these compounds in the bulk form (1.43 and 1.3 eV, respectively), thus suggesting a significant blue-shift in the NC optical properties due to quantum confinement effects.[220,225] The values of the bandgap extracted from the Tauc plots of the absorption spectra confirm the scaling of the emission. The trend in the gap energies of NCs compared to their bulk counterparts is consistent with TEM investigation, which in fact revealed a very small diameter for the present crystals, and with previous studies on Cs_2SnI_6 nanomaterials.[212,213,215] In the case of Cs_2SnBr_6 and Cs_2SnCl_6, instead, the PL peak energies are lower than the reported values for the bulk

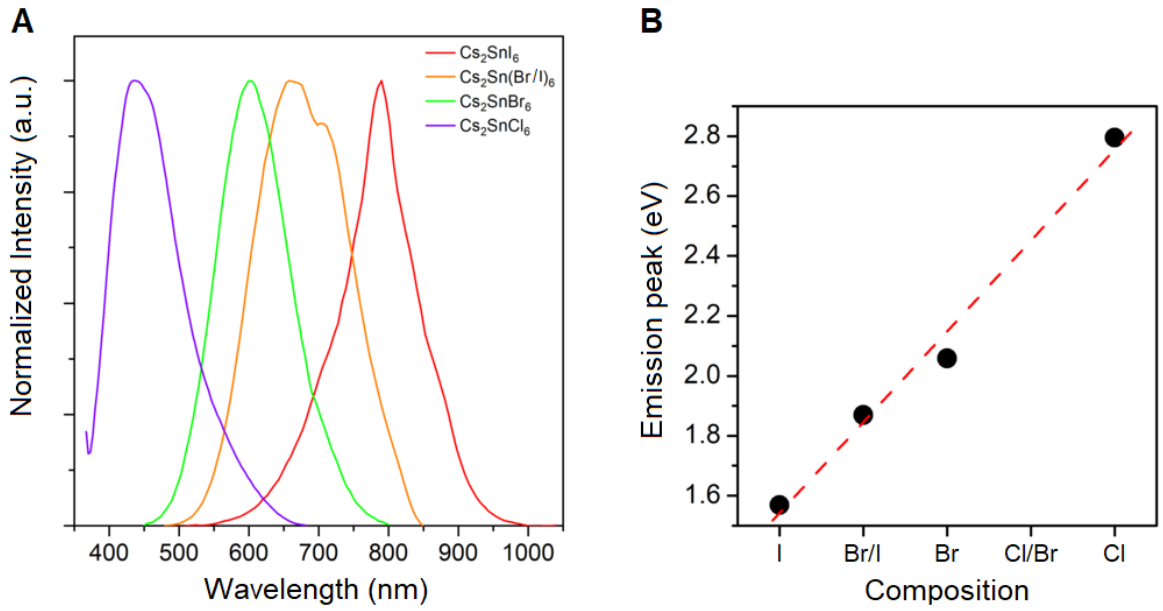

Figure 4.9 (**A**) Photoluminescence spectra of Cs_2SnX_6 NCs (X = Cl, Br, $Br_{0.5}I_{0.5}$, I) reacted for 1 minute. (**B**) Emission peak energy as a function of the halide content (dashed line is just a guide for the eye).

perovskites. Nevertheless, they still appear in line with a linear scaling of the emission peak as the NC composition varies from I to Cl (*Figure 4.9 B*), thus suggesting a more significant impact of size reduction for these materials and a possible dependence of the Stokes shift on the nature of the halide.[220]

Absorption and emission investigations were also carried out for the Cs_2SnI_6 NCs synthesized with different reaction times. The PL spectra reported in *Figure 4.10 A* reveal that the size of the NCs has a sizable impact on the luminescence properties of Cs_2SnI_6. By increasing the particle diameter from about 2.9 nm to about 3.2 (as determined by TEM measures), the emission peak shifts from about 741 nm (1.67 eV) to 793 nm (1.56 eV). This change in the optical properties is remarkable in proportion to the relatively small variation in the nanocrystal size. Moreover, the crystal size affects also the FWHM of light emission: the shift of the PL peak towards longer wavelengths is accompanied by a narrowing of the PL linewidth. In fact, the sample with the smallest NC size presents the broadest peak of the series, with a FWHM of more than 200 nm, while, on the other hand, the sample reacted for 10 min has the narrowest one, with a FWHM of 79 nm. These results, related to quantum confinement effects arising from

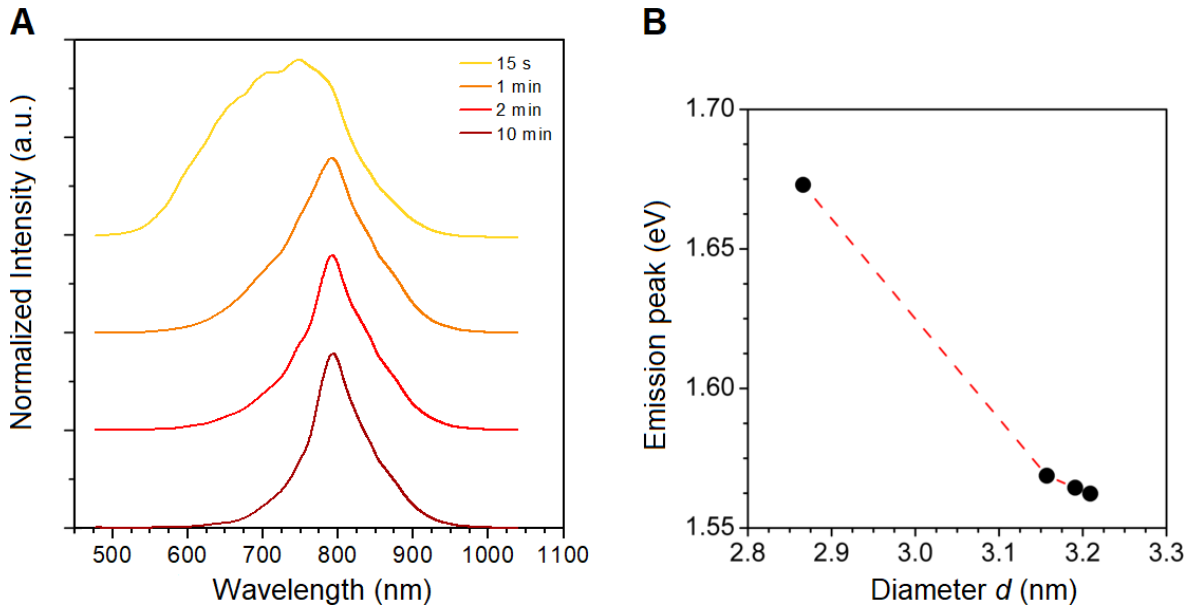

Figure 4.10 (**A**) Photoluminescence spectra of Cs_2SnI_6 nanocrystals reacted for 15 s, 1 min, 2 min, and 10 min. (Curves were shifted vertically for clarity). (**B**) Emission peak energy as a function of reaction time (dashed line is just a guide for the eye).

the small particle diameter, demonstrates how the luminescence properties of tin(IV) halide perovskite NCs can be tuned, with the present synthetic protocol, by varying both their chemical composition and their size.

The photoluminescence quantum yield (QY) was also evaluated for all the samples presented in the current chapter, and values ranging from 0.4% to 1.4% were found. Although such values are quite low if compared to the lead-based counterpart, they nevertheless represent an improvement with respect to the previously reported QYs for Cs_2SnI_6 NCs.[212]

Regarding air-stability, the present nanocrystals showed to retain their properties for about 9 days when deposited on a glass slide, covered with a cover slip, and stored in ambient conditions. *Figure 4.11 A* reports the absorption spectra of Cs_2SnI_6 NCs on a slide as a function of time over a period of 10 days, whereas *Figure 4.11 B* exhibits some selected photos of the sample under UV-lamp (excitation at 365 nm) at four time intervals. The images show clearly how, up to 5 days of air exposure, the properties of the crystals remained unchanged as their red emission was still very evident. From day 5, the sample started to exhibit the appearance of a new peak around 625 nm, thus suggesting the beginning of the perovskite decomposition.

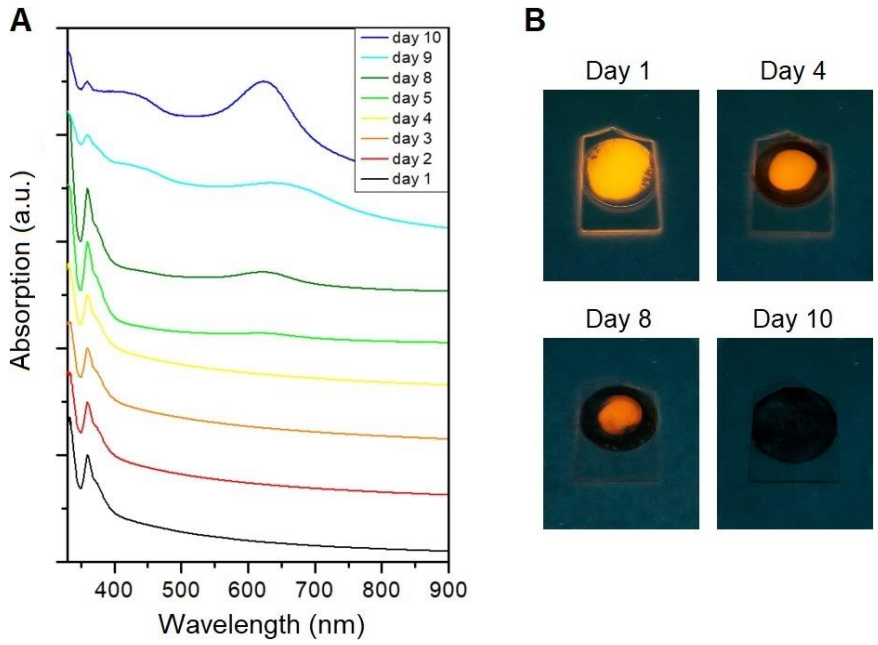

Figure 4.11 (**A**) Absorption spectra of Cs_2SnI_6 NCs as a function of air-exposure time. (Curves were shifted vertically for clarity). (**B**) Photos of Cs_2SnI_6 samples under UV-lamp at different time intervals.

As time passed, the absorption spectra became more and more altered until, at day 10, its profile was completely different, and the luminescence was totally suppressed. Although their stability is still limited to few days, these results prove a great enhancement in the resistance of tin(IV) halide perovskite NCs against air compared to their tin(II)-based counterpart and represent a good starting point to further improve their stability by playing with the synthetic routes and ligand engineering.

4.4 Conclusions

In summary, Cs_2SnX_6 (X = Cl, Br, $Br_{0.5}I_{0.5}$, I) nanocrystals have been prepared by a

simple hot-injection method, reporting for the first time the synthesis of Cs_2SnBr_6 and mixed $Cs_2Sn(Br/I)_6$ samples. The synthetic procedure can be performed under ambient conditions without the use of toxic phosphines and allows to tune the anion composition of perovskites. Besides, it leads to the formation of single-phase crystals with a cubic lattice that exhibit a linear scaling of the unit cell volume as the halogen content varies from chlorine to iodine. The prepared NCs, for the same reaction time, have a spherical shape with average size in the range around 3–6 nm, depending on the composition. Optical properties are nicely modulated by the halide content resulting in a progressive tuning of the optical emission from ~440 nm for Cs_2SnCl_6 to ~790 nm for Cs_2SnI_6. By varying the reaction time from 15 s to 10 min, the nanocrystal size shows only a limited growth (from about 2.9 to 3.2 nm) which however results in a progressive red-shift of about 0.1 eV of the bandgap as well as in a reduction of the PL spectra FWHM from 210 to about 80 nm.

The prepared samples exhibit stable optical properties under ambient conditions for some days. On the other hand, their QY reveal to be very poor while their emission linewidths appear much wider than those of LHP NCs, two aspects that may be attributed to the presence of electronic defect states. This hypothesis is also supported by absorption measurements which showed spectra with significant tails at long wavelengths. From these results, it appears that crystal defects play a fundamental role on the properties of tin(IV) halide perovskites: they may not only suppress their luminescence acting as nonradiative recombination centers, but also alter their optical features.

Despite these drawbacks, the present results add a significant contribution toward the discovery of new lead-free nanocrystalline compounds with enhanced air stability, showing for the first time an easy tuning of the optical properties of tin(IV)-based perovskite derivatives by anion composition in analogy with the previous results on 3D lead halide perovskites.

Chapter V
EFFECT OF DIFFERENT AMINES ON TIN(IV)-BASED NANOCRYSTALS

5.1 Introduction

As previously discussed in *Chapter III*, the ligands are a crucial element in the life of colloidal nanocrystals because they play several roles, each of fundamental importance, in the fabrication and use of nanomaterials: they drive the crystal growth during the synthesis, protect the crystals from the external environmental, passivate the dandling bonds on the surface thus suppressing the resulting defect states and making the crystals inert, and prevent aggregation in suspensions; these are some of their most important functions and clearly show the great impact they have on nanomaterials, but the list could easily go on.[35,226,227] It is not surprising that intensive research is dedicated to ligand engineering and the study of the NC surface chemistry in order to find the most suitable compounds to achieve the best results.[196] Since capping agents control the nucleation and growth processes of the crystals, they can be exploited to manipulate their morphology. Different molecules, indeed, have a different affinity for the various facets of NCs, therefore, by anchoring to specific surfaces, they can suppress their expansion and consequently promote the development in other directions, leading to an anisotropic growth.[156,227]

The present chapter shows how the properties of Cs_2SnX_6 (X = Br, I) nanocrystals are

affected by different capping agents. This research is a direct continuation of my work on tin(IV)-based vacancy-ordered double perovskites: the aim is to expand the knowledge on these perovskite derivatives and extend the results presented in the previous chapter. Herein, several amines different from the previously used oleylamine were employed. While OLA led to the formation of spherical NCs, the use of shorter chain amines caused a deep modification in the morphology of the NCs, favoring to the formation of 2D nanoplatelets (NPs). These molecules not only modify the shape of the crystals, but also alter their optical properties: increasing the length of the amine carbon chain, the bandgap of the crystals progressively widens while their emission peak shifts towards shorter wavelengths.

The following chapter, therefore, aims to discover how different capping agents affect tin(IV)-based perovskite NCs and investigate the correlation between the ligand length and the changes induced in the shape, crystal structure and optical properties of the nanomaterials.

5.2 Synthesis

The synthesis of the present Cs_2SnX_6 (X = Br, I) NCs was adapted from the hot-injection method previously reported in *Paragraph 4.2*. Once again, the perovskite precursors were tin(IV) halides and cesium oleate, and the solvent was octadecene. As seen in *Paragraph 3.4.2*, mixture of organic acids and amines is typically employed to passivate the surface of NCs. In this case, oleic acid was used in combination with different open-chain amines to investigate the effect of only one ligand with variable length while keeping the other component fixed. Specifically, the amines tested in the present chapter are hexylamine (C6A), octylamine (C8A), decylamine (C10A), and dodecylamine (C12A) because they are liquid at room temperature like oleylamine.

In a typical synthesis, 5 mL of ODE was loaded in a 50 mL three-neck flask along with 0.2 mL of OA and 0.2 mL of the desired amine, and the mixture was degassed under vacuum at

120 °C for 1 hour. Subsequently, 0.235 mmol of SnX_4 (0.1027 g of $SnBr_4$ and 0.1468 g of SnI_4, respectively) was added to the flask and the solution was dried under vacuum at 80 °C for 15 minutes. The flask was then moved under nitrogen flow and heated up to 220 °C. As soon as it reaches the desired temperature, 0.5 mL of the as-prepared Cs-oleate solution was quickly injected in the reaction vessel and after 1 minute it was cooled down in an ice water bath. To purify the NCs, 2.5 mL of Hex was added to the mother solution, the mixture was centrifugated at 7000 rpm for 5 minutes and the resulting supernatant was discarded. Part of the crystals was then deposited on glass slides for future measures while the rest crystals was dispersed in 5 mL of Hex. All the synthetic and purification processes were conducted under ambient conditions and no argon-filled glovebox was used to store the final samples.

5.3 Results

5.3.1 X-Ray Diffraction

The crystal structure of the two series of nanomaterials with different halide was investigated by mean of X-ray diffraction, and the relative diffraction patterns are reported in *Figure 5.1*. As discussed in the previous chapter, when OLA is used as capping agent in the synthesis of tin(IV)-based perovskite NCs, it produces spherical nanoparticles with a 0D vacancy-ordered structure that can be indexed according to the cubic Fm-3m space group (225). In this crystal phase, the samples show well distinct peaks between 12° and 33° corresponding to the reflections of (111), (220), (222), and (400) planes.

As evidenced by *Figure 5.1*, the replacement of OLA with shorter amines leads to

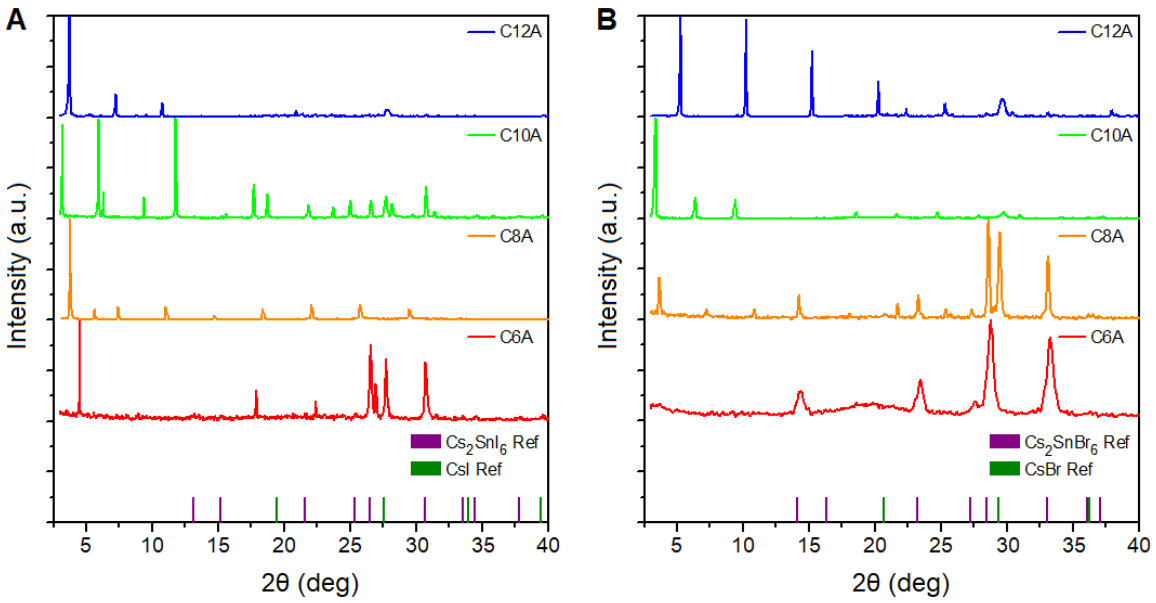

Figure 5.1 XRD patterns of (**A**) Cs_2SnI_6 and (**B**) Cs_2SnBr_6 samples synthesized with different amines. (Curves were shifted vertically for clarity)

dramatic changes in the XRD patterns: the appearance of intense periodic peaks at low angles is the essential evidence of the formation of 2D layered structures. These peaks, which correspond to the (002l) family of crystallographic planes, are indeed the fingerprint of this type of low-dimensional perovskites, indicating a high degree of preferred orientation. As discussed in *Chapter II*, in a conventional 3D perovskite the metal ion B and the halide X form a cubic array of $[BX_6]^{4-}$ octahedra sharing one corner in all the three directions, while the A ions are situated in the interstitial spaces of this metal-halide framework. In the observed 2D structures, instead, the octahedra are still corner sharing but only in two directions, meaning they are confined in planes separated by the ligand molecules.

The formation of these low-dimensional perovskites is related to the interaction between the ligands and the inorganic species during the synthesis. As discussed in *Paragraph 3.4.2*, organic acids and amines reveal to be very effective in passivating the surface of colloidal nanomaterials but only when combined.[187,191,199] This synergistic effect originate from a protonation reaction that takes place between the two organic molecules during the crystal synthesis: an H^+ ion is transferred from the carboxylic group -COOH to the amino group $-NH_2$ generating charged terminations $-COO^-$ and $-NH_3^+$ in the molecules that can bind to the crystal

surface ions.[156,190,197,228] In this framework, the protonated amine moiety attaches to the halide anions through hydrogen bonding due to their opposite charge. Depending on the synthetic conditions and the size and geometry of the amine, it may also enter into the crystal lattice between the different layers of $[BX_6]^{4-}$ octahedra, thus breaking their three-dimensional network and leading to the formation a 2D layered structure.[229,230]

When C6A is used in place of OLA, the diffractograms reveal that this substitution leads again to the formation of 3D nanocrystals. It is important to note that here "3D" refers to the morphological dimensionality of the nanocrystals, not the structural dimensionality of the perovskite, which is in fact 0D. The peaks of Cs_2SnBr_6 are also qualitatively equal to those of Cs_2SnI_6 but shifted to higher angles thus suggesting a reduction of the crystal cell volume as expected since Br^- ions are smaller. In the case of Cs_2SnI_6, however, the coexistence of layered structures was also detected as revealed by the peaks at 4.51°, 17.89° and 22.41°. Moving from C6A to C8A, the patterns appeared very different: 2D phases were now predominant with well distinguishable peaks at low angles while the 3D phase disappears in the iodide-based samples and just small traces were present in the bromide-based ones. Finally, a further increasing of the amine molecule length resulted in the complete vanishing of the 3D phase and only the NP peaks are now detectable. When only OA is used as ligand, instead, the synthesis led to 3D NCs, but they did not present any photoluminescence emission.

The formation of different crystal structures is related to a competition between the Cs^+ ions and the alkylammonium ions to bind to the inorganic octahedra during the nanocrystal growth.[156,231] The prevalence of NPs over NCs in a synthesis depends on the ratio between amine and Cs, the amine binding affinity for the tin(IV) halide and the acid-base equilibrium between the ligands.[215,232] When the pH decreases, the amine molecules protonate and the concentration of alkylammonium raises. This unbalances the reaction at the expense of Cs and the growth of 2D structures is promoted. The appearance in our samples of different crystal phases depending on the halogen may be due to the different binding affinity of the amines with the two halides; this aspect requires further investigation to understand the correlation between the amine length and the crystal morphology and its origin.

Interestingly, the presence of cesium halide was noticed in almost every sample. This can be due to the excess of tin(IV) halide used during the syntheses. As mentioned above, when

the amino group of the capping molecules bonds to the octahedra layers it takes in fact the position of the A cation, so the Cs^+ ions that do not enter into the lattice can react with the excess halogen in the solution producing the halide salts that was indeed detected. These results show already clear evidence of the influence that capping agents have on the structure of nanocrystals.

5.3.2 Electron Transmission Microscopy

The changes in the crystal shape and morphology are also confirmed by high resolution transmission electron microscopy (HRTEM). The images reported in *Figure 5.2* and *Figure 5.3* show remarkable differences if compared with those of the previous chapter. As already suggested by XRD analysis, the C6A sample of the iodine series presents a mixed phase

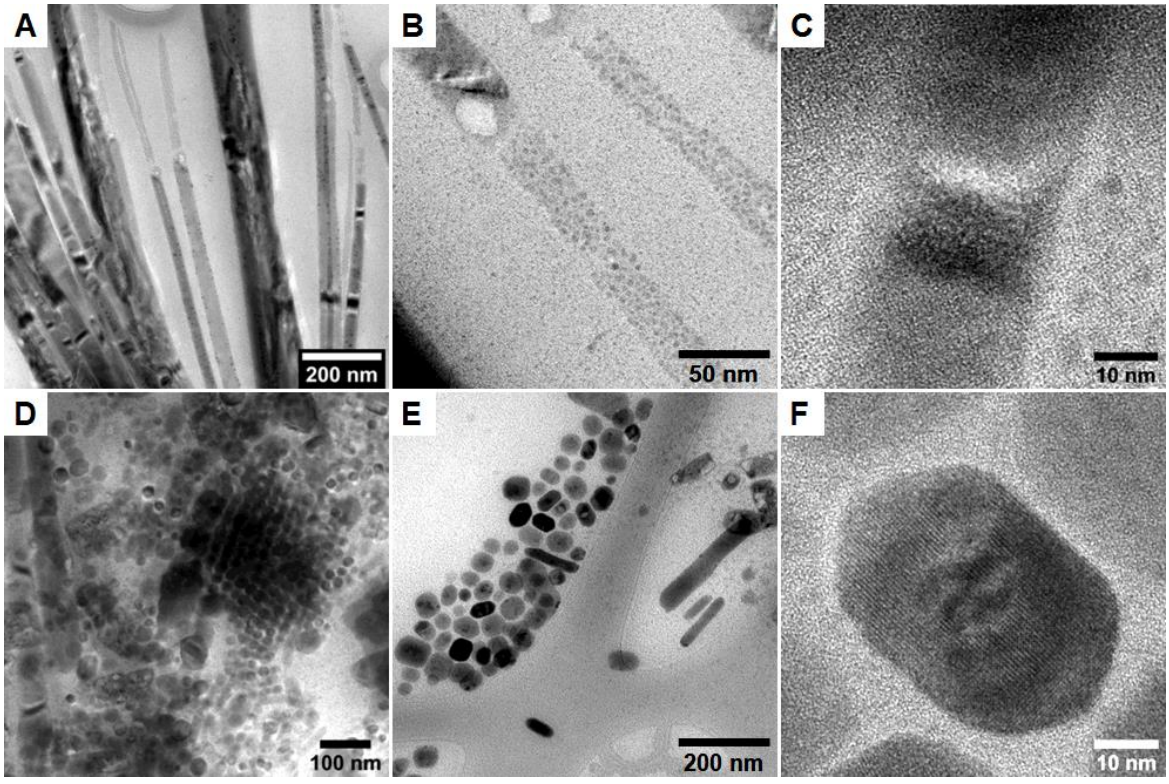

Figure 5.2 HRTEM images of Cs_2SnI_6 samples synthesized with (**A**, **B**, **C**) C6A and (**D**, **E**, **F**) C12A at different magnifications.

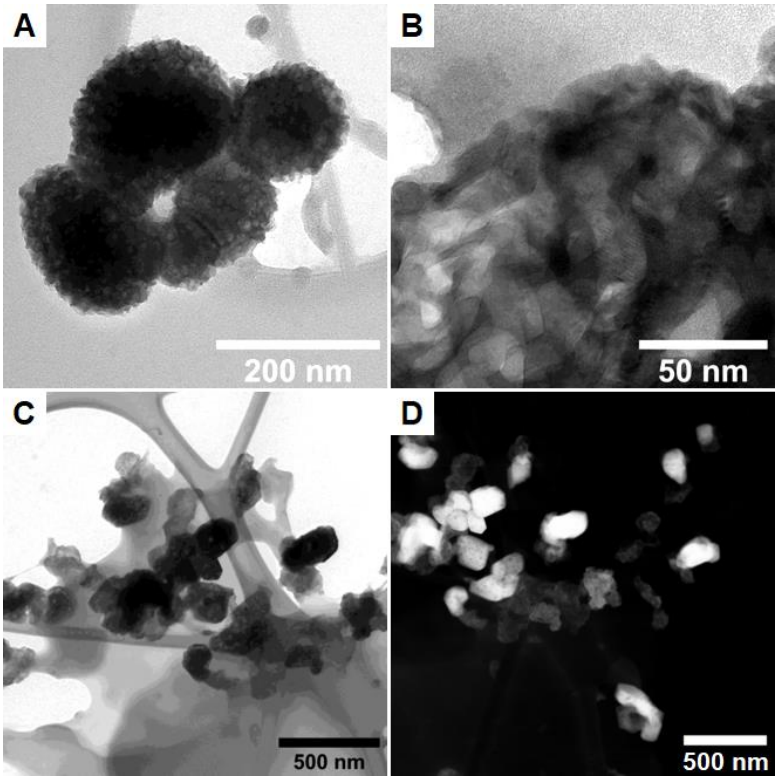

Figure 5.3 HRTEM images of Cs_2SnBr_6 samples synthesized with (**A**, **B**) C6A and (**D**, **E**) C12A at different magnifications.

comprising spherical NCs and 2D nanobelts, namely planar structures elongated in one direction with lateral size of hundreds of nanometers. In particular, the NCs display similar features to those synthesized with OLA but are characterized by a bigger diameter of about 10 nm. The C12A sample, instead, consists only of a 2D phase with NPs of hexagonal or square shape. This planar morphology reflects the layered crystal structure that was detected by XRD measurements, meaning that in these nanomaterials the structural and morphological dimensionalities are both 2D. Contrary to 3D crystals, here the platelets appear more varied presenting different shapes and a wide size distribution ranging from 10 to almost 100 nm. Both samples show a high degree of crystallinity as verified by electron diffraction (*Figure 5.4 A* and *B*). These results are in agreement with the only literature data on 2D layered structures of Cs_2SnI_6 where researchers obtained hexagonal NPs with lateral size of several hundreds of nanometers.[215]

The analysis on the Cs_2SnBr_6 series leads to similar results, although with some

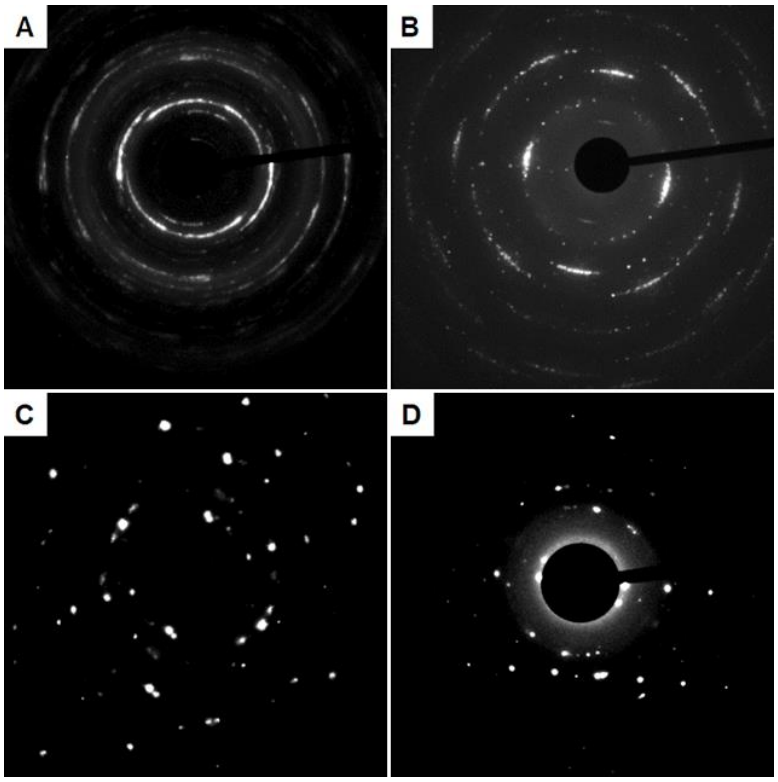

Figure 5.4 Electron diffraction images of Cs_2SnI_6 samples synthesized with (**A**) C6A and (**B**) C12A, and Cs_2SnBr_6 samples synthesized with (**C**) C6A and (**D**) C12A.

substantial differences. The C6A sample presents aggregates that appear made of spherical NCs of the order of 50 nm, with no planar structures like the previous nanobelts. The C12A sample, instead, shows only 2D NPs with lateral size of hundreds of nanometers. As mentioned, contrary to the I series, the Cs_2SnBr_6 crystals exhibit a high tendency to agglomerate forming clusters of great size. However, the electron diffraction reveals that also these samples are highly crystalline (*Figure 5.4 C* and *D*).

The cause of this phenomenon is unclear. In general, the colloidal stability of nanocrystals is a multifactorial issue that depends on the nature of the compound, the ligands and the suspension solvent, and it is determined by a balance between attractive and repulsive interparticle forces.[198] The aggregation of the Br-based samples could be related to a different interaction between halide and amines that makes the ligand binding to the crystal surface more labile, but its origin and mechanisms are still unknown and a thorough investigation is needed to understand them.

The HRTEM instrumentation allowed also to perform energy dispersive X-ray (EDX) analysis to investigate the chemical composition of the samples. Representative EDX elemental maps are reported in *Figure 5.5*. They show the clear presence of the three constituting elements of each perovskite, thus confirming the formation of the compounds revealed by the previous XRD analysis.

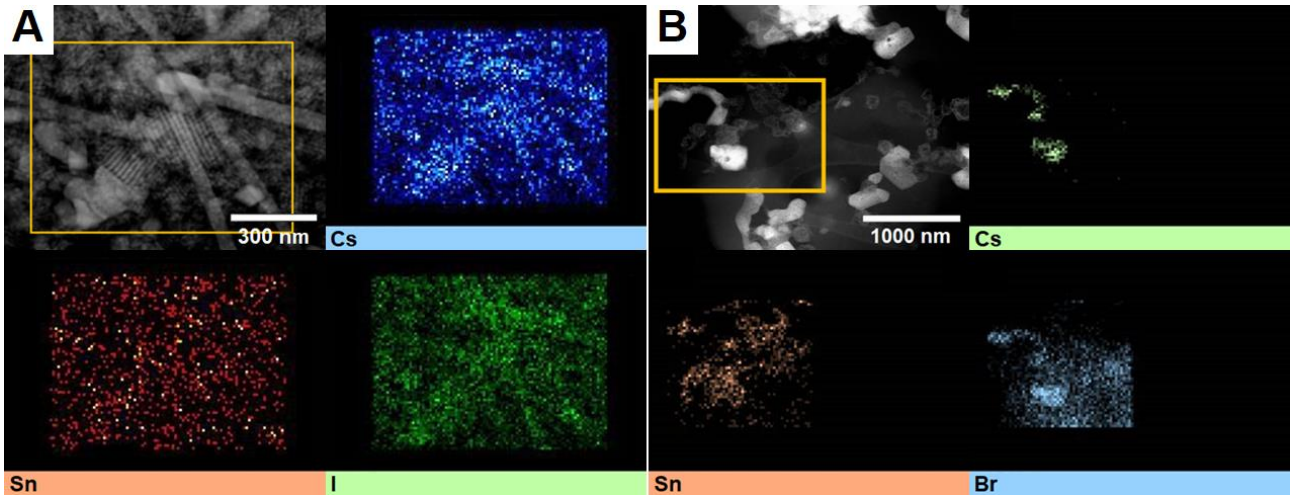

Figure 5.5 EDX elemental map of (**A**) Cs_2SnI_6 and (**B**) Cs_2SnBr_6 nanoplatelets synthesized with C12A.

5.3.3 Optical Properties

The length of the amine carbon chain not only affects the morphology of the crystals but also their optical properties. The absorption spectra of both I and Br series are reported in *Figure 5.6*. From a qualitative analysis, the NP spectra appear significantly different when compared to those of their 3D counterparts: they present a slow rise across the entire visible range and a rapid increase in the UV region. Moreover, differently from lead-based NCs, none of the samples have a sharp excitonic absorption peak, but rather they display a long tail toward the low energies. This feature has been previously reported also for tin(IV)-based perovskite thin films and it was attributed to the presence of crystal defects (most likely halide vacancies since they have a low formation energy) that introduce a sizeable density of shallow electronic states below the conduction band (CB) edge.[216,223,224] In the case of Cs_2SnBr_6, the C6A and C8A

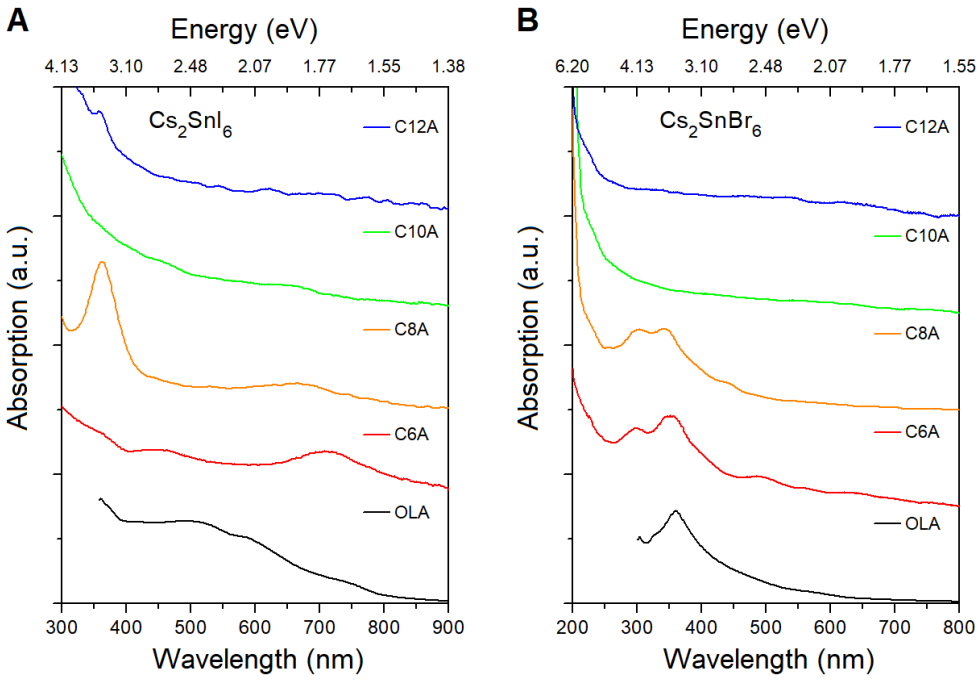

Figure 5.6 Absorption spectra of (**A**) Cs_2SnI_6 and (**B**) Cs_2SnBr_6 samples synthesized with different amines. (Curves were shifted vertically for clarity).

samples also show a peak around 360 nm, similarly to their 3D counterparts, which disappears for the longer amines. This difference can be explained by the exclusive presence of the 3D phase in these samples, as previously inferred from XRD measurements.

From the Tauc plots for direct bandgap of the absorption spectra the value of the energy bandgap is derived. For 3D NCs synthesized with OLA, Cs_2SnI_6 and Cs_2SnBr_6 were found to have gaps of 1.57 eV and 3.33 eV, that are higher than those of their relative bulk forms (1.3 eV and 2.7 eV, respectively).[225,233] On the other hand, moving to 2D structures, it can be observed that the gap energy becomes even higher, growing linearly as the amine length increases (*Figure 5.7*). These results can be ascribed to quantum confinement effects caused by the small size of the crystals consistently with previous studies on Cs_2SnI_6 NCs.[212,213,215,234] In particular, being made of a few atomic layers, perovskite NPs are reported to have very strong exciton confinement, thus explaining their larger increment of the bandgap.[147,154,235] Besides the case of NPs, the gap energy of 3D NCs synthesized with short amines is also evaluated from Tauc plot extrapolations. In the case of Cs_2SnI_6 sample with C6A, where mixed phase is present, the gap of 3D phase is estimated at 1.54 eV. The NCs of the C6A and C8A samples with Br,

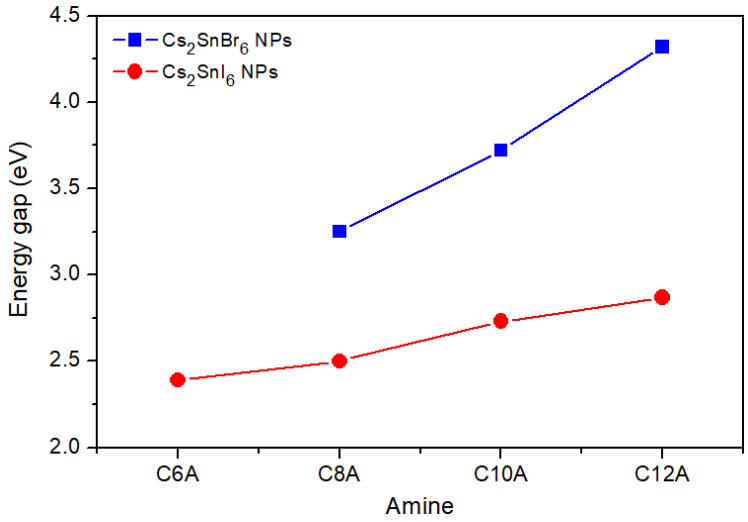

Figure 5.7 Fundamental energy gap of 2D nanoplatelets as a function of the amine length used as capping agent. (Lines are just a guide for the eye).

instead, are found to have a gap energy of 3.13 eV and 3.25 eV, respectively. All these values are reasonably close to those of NCs prepared with OLA and the differences can be ascribed to the larger diameter of the crystals causing a smaller size effect. Light emission was also affected by the change in the nanocrystal dimensionality. As it is evident from the photoluminescence spectra of *Figure 5.8*, replacing OLA with shorter amines resulted in a blue-shift of the emission, which was particularly evident in the case of I compounds where the emission color changes from dark red to orange. The 3D NCs of Cs_2SnI_6 and Cs_2SnBr_6 presented PL peak emission at 790 nm and 603 nm, respectively. Moving from C8A to C12A, the emission of Cs_2SnBr_6 NPs shifted from 599 nm to 575 nm following a linear trend. In the case of Cs_2SnI_6, instead, the NP spectra were peaked at 635 nm, 624 nm, and 628 nm. Remarkably, the samples synthesized with C6A of both halide series did not show any emission.

As mentioned, in the synthesis of nanomaterials ligands play a crucial role in stabilizing the crystals.[236] Moreover, the chemical stability of NCs depends on the shape of ligand molecules: long and branched molecules were demonstrated to achieve the best results in stabilizing nanomaterials.[48,187,190,237] In this regard, the lack of emission from the C6A samples can be attributed to a poor stabilization of the amine resulting in the formation of defect states that quench the PL radiative process. The emission energy peak of each sample appeared to be

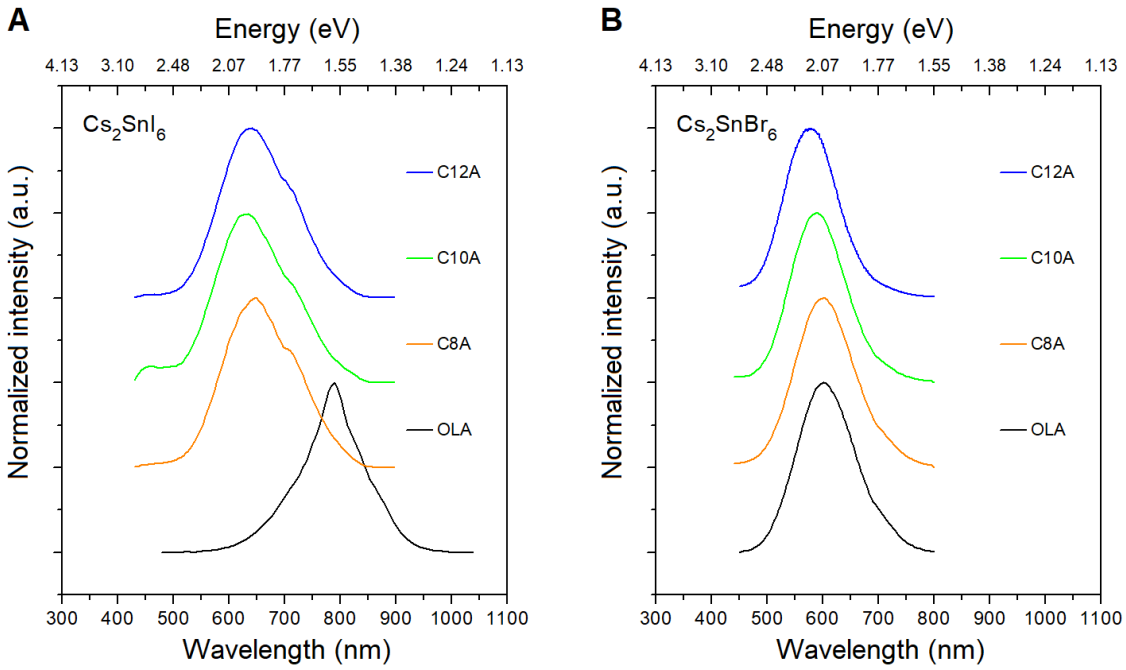

Figure 5.8 PL spectra of (**A**) Cs_2SnI_6 and (**B**) Cs_2SnBr_6 samples synthesized with different amines. (Curves were shifted vertically for clarity).

significantly lower than the value found for its energy gap. Coherently with the wide tail observed in the absorption spectra, this large Stokes shift may be caused by a high density of electronic states, arising from crystal defects, which locate right below the CB minimum: when the electrons are excited into the CB, they thermalize towards the edge, transfer into the defect states, and finally decay in the valence band with radiative emission of light. This phenomenon requires further investigation to be fully understood.

Due to the asymmetry of the curve, the PL spectra were fitted using two Gaussian lineshapes thus revealing a second peak at longer wavelengths, from 729 to 717 nm for the I samples, and from 697 to 642 nm for the Br samples. The corresponding energy values of the two emission peaks are reported in *Figure 5.9*. Accordingly with previous study by Xu et al. on Cs_2SnI_6 2D NPs, the peak emerging at lower energy may be ascribed to an emission from defect states.[215] In their work, indeed, Xu and coworkers attributed the origin of such defects to a structural distortion caused by a phase transition between two layered structures based on orthorhombic and monoclinic unit cells. This lattice distortion should modulate the formation energies of the defects while the spatial shifts of the ligand molecules, altering the bonding

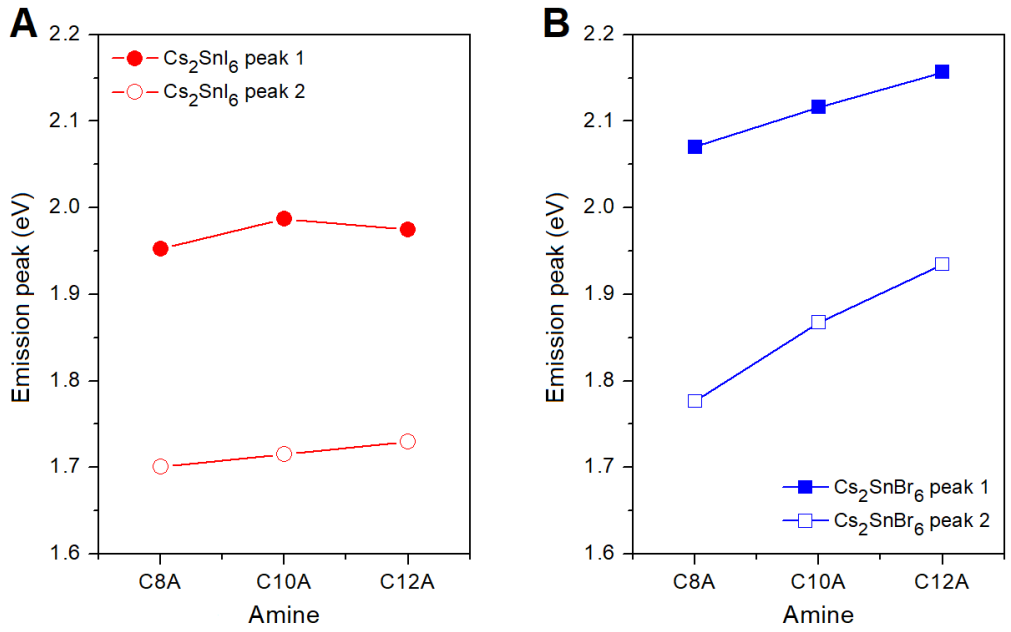

Figure 5.9 Energy of the PL peaks of (**A**) Cs_2SnI_6 and (**B**) Cs_2SnBr_6 2D nanoplatelets. (Lines are just a guide for the eye).

between the amino group and the halide octahedra, can generate more crystal defects. This phenomenon has already been observed in lead(II)- and tin(IV)-based 2D layered perovskites[238–241] and can be consistent with our previous observations on large Stokes shifts in emission and wide tails in absorption. However, to fully reveal the link between these three aspects and their exact origin further studies are needed.

5.4 Conclusions

In summary, the facile hot-injection method developed to synthesize simultaneously 3D nanocrystals and 2D nanoplatelets for both Cs_2SnI_6 and Cs_2SnBr_6 perovskites. The crystal morphology was tuned by changing the amine employed as capping agent during the synthetic

procedure. When using OLA, the most common amine widely employed in literature, the synthesis led to spherical NCs with a very small diameter of about 3 nm. When using amines with a shorter carbon chain, instead, the results were very different and the synthesis led to 2D layered NPs with diverse crystal structures depending on the ligand used, as demonstrated by XRD and TEM analyses. The change in the morphology of the crystals was also followed by a modification of their optical properties. Thanks to the reduced size, all the samples presented a much wider bandgap in comparison to their bulk form due to strong quantum confinement effects. In particular, increasing the amine length, the gap energy of the NPs linearly shifted from 1.3 eV to 2.87 eV in the case of Cs_2SnI_6 and from 2.7 eV to 4.32 eV in the case of Cs_2SnBr_6. Besides, light emission was also affected by the ligand choice and changing the amines allowed to tune the emission of Cs_2SnI_6 samples from 1.57 eV to 1.99 eV moving from 3D NCs to 2D NPs, and analogously from 2.06 eV to 2.16 eV nm for the Cs_2SnBr_6 samples. These results present an interesting advance in the research on perovskite nanocrystals towards lead-free compounds and offer a further insight in tin(IV)-based double perovskites for possible future applications in optoelectronic devices.

Chapter VI

BISMUTH-BASED PEROVSKITE NANOCRYSTALS

6.1 Introduction

Besides using the homovalent metals of Group 14, another strategy to remove lead from halide perovskites is to replace it with neighboring elements. In this context, bismuth is one of the most investigated substitution thanks to its very low hazardousness: elemental bismuth and its compounds, indeed, have a negligible toxicity because they are highly insoluble and, consequently, are hardly absorbed by the human body, although the ingestion of high doses may still lead to poisoning.[39,242] Moreover, as the next element after Pb in the Periodic Table, bismuth has a comparable ionic radius (1.19 Å for Pb^{2+} and 1.03 for Bi^{3+})[200] and a similar electronic configuration with a lone pair of electrons in the 6s orbital, thus it appears to be a reasonable alternative to lead.

Like in the case of tin(IV), the substitution of Pb with a heterovalent element, however, alters the chemical composition and the 3D structure of the perovskites in order to maintain the charge neutrality of the crystals. Bismuth halide perovskites (BHPs) are not characterized by a unique chemical formula: usually they adopt the composition $A_3B_2X_9$ but there are many other variants that follows the general formula $A_aB_bX_{a+3b}$ like, for example, $CsBiBr_4$, $CsBi_2Br_7$ and Cs_3BiBr_6. Besides the variety of compounds, BHPs also present different polymorphs, of

which the most common are a 0D phase and a 2D vacancy-ordered phase (*Figure 6.1*).[243–245] The constituting units of the 0D structure, also called dimer phase, are $[B_2X_9]^{3-}$ clusters made of two face-sharing $[BX_6]^{3-}$ octahedra. These clusters are arranged in a hexagonal lattice with the A ions placed around them and result to be completely isolated from each other. The 2D structure, instead, comprises of corrugated layers of corner-sharing octahedra stacked on one another. It is derived from the standard 3D perovskite lattice by removing every third layer of B ions along the ⟨111⟩ direction, therefore the crystals displaying such a structure are in fact vacancy-ordered perovskite derivatives (Like in the case of tin(IV)-based 0D perovskites, their formula can be expressed as $A_3\square B_2X_9$ or $A(\square_{1/3}B_{2/3})X_3$, thus highlighting how their constituting ions are tripled while one third of the metal ions are removed.

In addition to the dimer and layered phases, BHPs may also present many other crystal structures with different dimensionalities.[246,247] For example, $MA_3Bi_2Cl_9$ exhibits a 1D lattice whose building units are zigzag chains of corner-sharing $[BiCl_6]^{3-}$ octahedra.[248] This structure is obtained once again from the 3D perovskite lattice by removing every third layer of B ions along the ⟨110⟩ direction as well as the ⟨001⟩ direction to keep the charge balance. The capability of the bismuth-based perovskites to adopt a certain structure over the others depends on the radii of their constituting ions and the synthesis conditions, and it does not follow any trend.

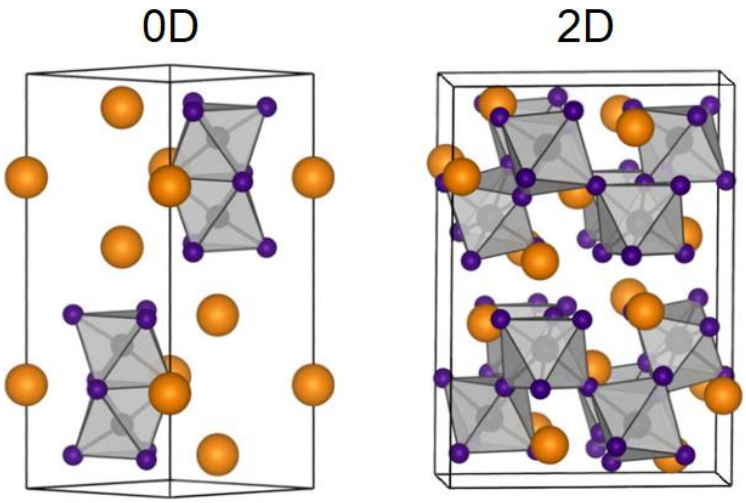

Figure 6.1 Crystal structure of 0D and 2D bismuth halide perovskites. Adapted from ref [245].

Irrespectively of the crystal phase, BHPs are always characterized by a lower structural dimensionality compared to their lead-based counterpart due to the heterovalent substitution of Pb. As discussed in *Paragraph 2.2.1*, the reduced dimensionality decreases the dispersion of the electronic bands and, consequently, affects the optoelectronic properties of the materials. Bismuth halide perovskites, indeed, exhibit high gap energies of about 2 eV or more[244,249] and large effective masses of the charge carriers.[49,250,251] This results in high exciton binding energies (hundreds of meV), low carrier mobilities and overall poor electronic transport properties. Besides, in many compounds the majority of intrinsic crystal defects is proved to introduce deep electronic states.[245,248,252] For these reasons, BHPs do not appear to be suitable materials for photovoltaic applications. Nevertheless, these materials present also some advantages compared to lead-based perovskites. In addition to the lower toxicity, they exhibit a higher stability against air and water.[244] Furthermore, the reduced structural dimensionality allows to incorporate a large number of heterovalent doping atoms into the lattice without altering the crystal structure, thus enabling the realization of compounds with new and enhanced properties.

In recent years, metal halide perovskites have been explored as possible materials for heterogeneous photocatalysis.[5,253] Theoretically, an ideal photocatalyst must have a series of physical properties that are essential to achieve high performance: great level of operational stability, strong light absorption, efficient separation of charge carriers, and appropriate redox ability for target reactions.[254] As seen in previous chapters, LHPs are characterized by small exciton binding energies, long carrier lifetimes and high carrier mobilities (all features that contribute to good charge separation), as well as high absorption coefficients and an easily tunable bandgap over the entire visible region. Moreover, the electronic band structure of several lead-based perovskites reveals to be aligned with the most common redox half-reactions, thus making these materials suitable for solar-driven catalysis of both reduction and oxidation reactions.[5]

Owing to their non-toxicity and better stability in water, bismuth halide perovskites seem to be a valid alternative to LHPs for photocatalysis in aqueous environments. Although this research topic is very recent, these compounds have already proved to achieve high performances in various catalytic processes such as degradation of organic pollutants,

reduction of carbon dioxide and evolution of hydrogen.[255–258] In particular, the use of 2D perovskite $Cs_3Bi_2Br_9$ combined with graphitic carbon nitride g-C_3N_4 (GCN) in the photogeneration of hydrogen was recently reported with remarkable results.[259] GCN is a well-known polymeric semiconductor that is widely employed as photocatalyst in a variety of reactions, in addition to many other applications.[260–262] The idea of coupling this material with different compounds to boost its photocatalytic activity is a strategy that was extensively explored in the past[263,264] and, in the last few years, it has also been tested with MHPs.[265,266]

In the current chapter, the synthesis and characterization of lead-free $Cs_3Bi_2X_9$ nanocrystals (X = Br, I) are presented, as well as the fabrication of composites of GCN with $Cs_3Bi_2Br_9$ NCs and their use in the photogeneration of hydrogen. The purpose of this research is to expand the previous results on these composites by investigating the effects of the perovskite size reduction on their photocatalytic activity.

6.2 Synthesis

Initially, the crystals were attempted to be synthesized using a hot-injection synthesis adapted from literature, like in the case of tin(IV)-based NCs.[267] However, despite the different trials, this procedure led only to the formation of Cs_3BiX_6 perovskites (X = Br, I). To overcome such a problem, a different approach was tried: the ligand-assisted reprecipitation (LARP) method. Like its hot-injection analogue, this method is a bottom-up technique that is performed in solution, and it is widely used in the fabrication of nanocrystals. In a typical LARP synthesis, all reagents are dissolved in a strong polar solvent along with the ligands to form a precursor solution. In this case, the reagents are usually halides salts of A and B, and they are combined in a stoichiometric ratio to form the perovskite. The precursor solution is subsequently injected into a weak solvent to induce a rapid drop in the solubility of the reagents. This sudden change instantly leads a supersaturation condition and, consequently, triggers the nucleation of the

nanocrystals, which is later followed by the crystal growth according to LaMer model (see *Paragraph 3.1*). Finally, the product is collected and purified by centrifugation (*Figure 6.2*).[268] In this type of synthesis, the key parameters that allow to control the size and shape of the NCs are the reaction time, the ratio between the precursors, the ratio between precursors and ligands, and the ratio between the two solvents. The reaction temperature is another factor that can be used to modulate the properties of the final crystals, however LARP syntheses are usually conducted at room temperature. In fact, the LARP technique does not require high temperatures, vacuum systems, or inert atmosphere to be performed, therefore it is simpler and cheaper than the HI method and it can be easily scaled up.[36] On the other hand, the NC quality offered by this approach is generally a little lower in comparison to the HI counterpart, and the use of polar solvents poses a risk to the integrity of the nanomaterials. As previously discussed, indeed, polar liquids can readily dissolve MHPs due to the strong ionic component of their binding, so the presence of residual solvent molecules in the final product can undermine its stability.

For the synthesis of the present $Cs_3Bi_2X_9$ nanocrystals (X = Br, I), dimethylsulfoxide (DMSO) and chloroform (Chl) were used as strong solvent and weak solvent, respectively. The perovskite precursors were cesium halides and bismuth(III) halides, while the capping agents were oleylamine (OLA) and oleic acid (OA). Based on previous literature on LARP NCs of

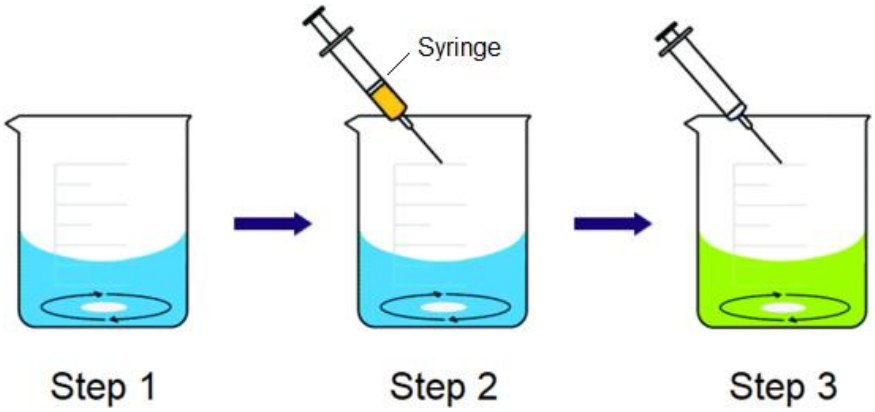

Figure 6.2 Schematic representation of the ligand-assisted reprecipitation method. In the first step the precursor solution and the weak solvent are prepared. In the second step the solution is injected into the weak solvent. In the third step the resulting suspension is centrifugate to collect the nanocrystals. Adapted from ref [268].

bismuth-based perovskites,[269,270] the following procedure was developed: 0.3 mmol of CsX (0.0638 g of CsBr and 0.0779 g of CsI) and 0.2 mmol of BiX_3 (0.0897 g of $BiBr_3$ and 0.0 g of BiI_3) are dissolved in 3 mL of DMSO and, after complete dissolution of the powders, 33 µL of OLA is added to the solution. The addition of amine causes the formation of small floccules in the mixture that disappear after a brief sonication. 0.5 mL of the as-prepared precursor solution is then quickly injected into 5 mL of Chl, mixed with 0.5 mL of OA, under sonication. After 1 minute, the solution is centrifugated at 10000 rpm for 10 minutes and the resulting supernatant is discarded. The final NCs are collected and dispersed in 5 mL of Chl to form a suspension. All the synthetic and purification processes are conducted under ambient conditions and no argon-filled glovebox is used to store the final samples.

For the preparation of nano-$Cs_3Bi_2Br_9$/g-C_3N_4 composites, 0.1500 g of g-C_3N_4 is combined in a 25 mL beaker with 3 mL of Chl. Subsequently, different volumes of the NC suspension are added under vigorous stirring to obtain distinct loadings of the perovskite in weight percentage. Specifically, samples with loadings of 1 wt%, 5 wt%, and 10 wt% were prepared. The mixture is then dried overnight at room temperature under stirring and the following day the resulting powder is collected and stored under ambient conditions.

6.3 Results

6.3.1 X-Ray Diffraction

The crystal structure of the perovskite NCs and the related composites with GCN was investigated through X-ray diffraction measures. As seen in previous chapters, the diffractograms of 0D tin(IV) halide perovskites show the same profile but shifted at different angles owing to the different halide radius that changes the lattice constant. In the case of BHPs, instead, the samples exhibit very different diffraction patterns moving from bromide to iodide

(*Figure 6.3*). This difference is related to the different structural dimensionality of the perovskites. The XRD analysis shows indeed that $Cs_3Bi_2Br_9$ NCs have a trigonal lattice belonging to the P-3m1 space group (164), while $Cs_3Bi_2I_9$ NCs have a hexagonal lattice belonging to the space group $P6_3/mmc$ (194). Such lattices correspond in fact to a 2D layered structure and a 0D dimer structure, respectively, as described in *Paragraph 6.1*. These results are consistent with data reported in literature.[271–273] Moreover, the two samples appear to be single-phase and no traces of cesium halides or other impurities are detected, thus demonstrating the effectiveness of the present LARP approach in synthesizing both Br- and I-based BHP crystals.

The diffraction patterns of nano-$Cs_3Bi_2Br_9$/g-C_3N_4 composites are reported in *Figure 6.4*. In the case of pure GCN (0% composition), only two broad peaks are observed at 12.99 and 27.38 degrees. They derive from the typical stacking of carbon nitride layers along the ⟨100⟩ and ⟨002⟩ directions, respectively, and prove the material to have a hexagonal structure that can be indexed according to the $P6_3cm$ space group (185), in line with literature.[261,274,275] The peak positions are also in agreement with previously reported values. The peaks around 22 and 34 degrees, which are found in all the samples, are just background (BG) caused by the sample holder.

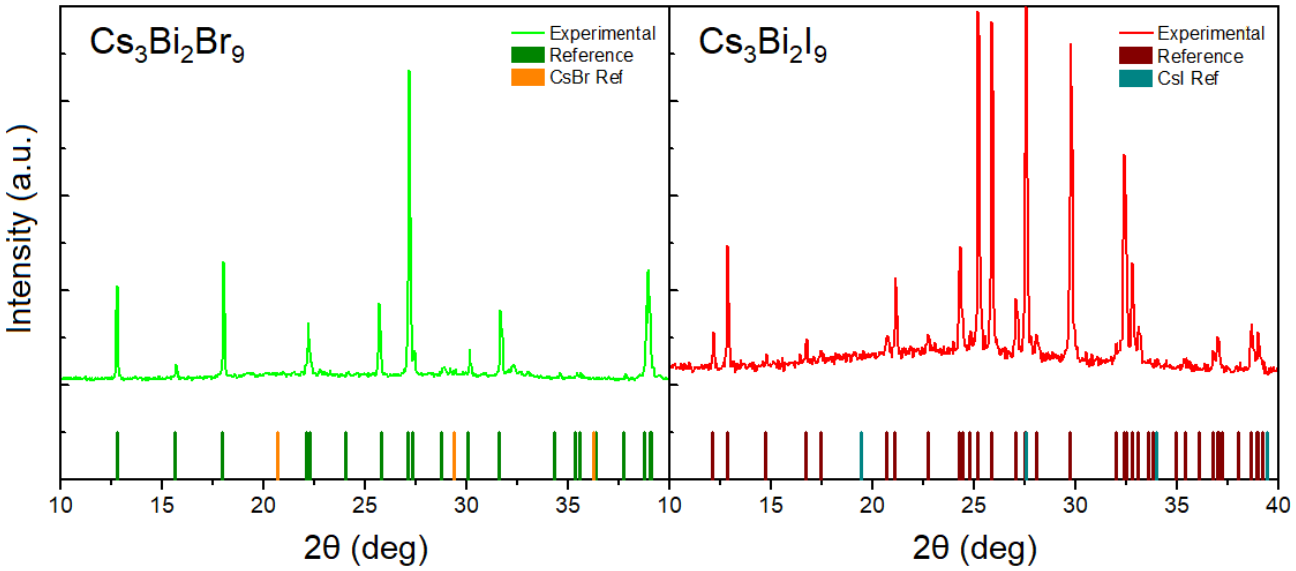

Figure 6.3 X-ray diffraction patterns of $Cs_3Bi_2Br_9$ nanocrystals (right) and $Cs_3Bi_2I_9$ nanocrystals (left).

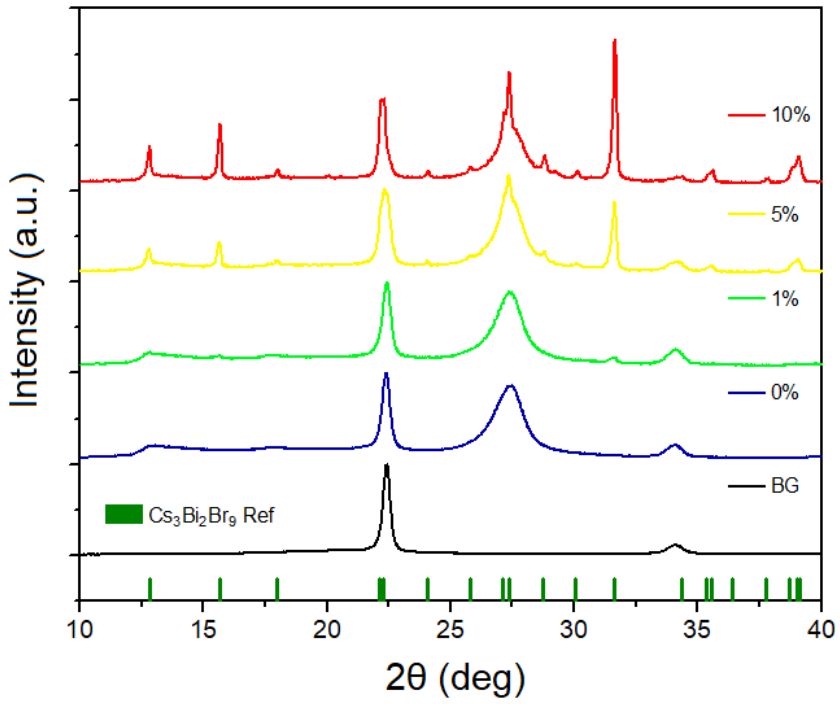

Figure 6.4 X-ray diffraction patterns of nano-$Cs_3Bi_2Br_9$/g-C_3N_4 composites prepared with different perovskite loading in weight percentage. (Curves were shifted vertically for clarity)

The diffraction pattern of the composite with 1% loading has the same profile of that of pure GCN with the exception of a small new spike occurring at about 32 degrees. The appearance of this peak, which corresponds to the (022) reflection of $Cs_3Bi_2Br_9$, proves that the perovskite contribution to the X-ray diffraction is already detectable at this low percentage of loading. On the other hand, for higher loading values the impact of the NCs become even more evident and dominates the diffractogram profile. As for the nanocrystalline sample, the perovskite peaks are in accordance with the reference pattern, thus demonstrating that its crystal structure does not change during the preparation of composites.

6.3.2 Morphological Characterization

High resolution transmission electron microscopy was used investigate the shape of the NCs and the resulting images are reported in *Figure 6.5*. Both samples appear homogeneous,

showing only one morphology. Br-based sample consists of spherical particles with an average diameter of about 2 nm. The crystals have a uniform size distribution and are well dispersed, similarly to previous tin(IV) halide perovskite NCs. I-based sample also presents spherical particle, but they are characterized by a large diameter of about 3.5 nm. Moreover, the crystals appear less dispersed, in fact they tend to agglomerate into thick clouds. This dissimilarity between the two materials could be an indication of a different tendency of $Cs_3Bi_2I_9$ NCs to form aggregates. As discussed in previous chapters, the aggregation of colloidal nanocrystals is the result of a competition between attractive and repulsive forces and depends on several factors. In this case, the formation of dense assemblies of particles may be related to a different binding of the ligands with the halide, but the precise mechanisms behind this phenomenon are unknown and require further examination to be fully understood.

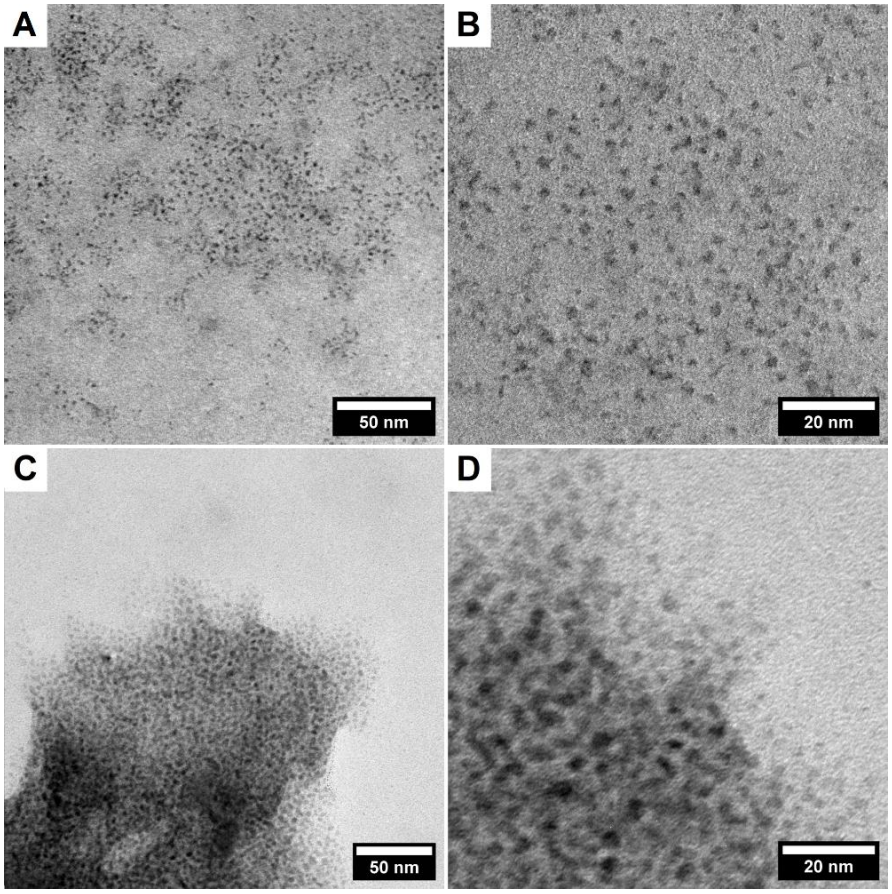

Figure 6.5 High resolution TEM images of (**A**, **B**) $Cs_3Bi_2Br_9$ and (**C**, **D**) $Cs_3Bi_2I_9$ nanocrystals at different magnifications.

Despite aggregation, electron diffraction proved that both samples are characterized by a high degree of crystallinity (*Figure 6.6*).

The morphology of the composites was instead investigated through scanning electron microscopy (SEM) and backscattered electron (BSE) imaging. The latter was used to specifically identify the $Cs_3Bi_2Br_9$ component by detecting the bismuth ions in the samples. Since this element belong exclusively to the perovskite, this technique allows then to recognize the NCs on the surface of g-C_3N_4 and create a visual picture of them. Two representative images of 5% composite are presented in *Figure 6.7*. GCN displays a lamellar structure agglomerated into grains with a size of 1–15 μm. The morphology of this material is closely related to the how it is synthesized, and these results are consistent with previous literature.[276] BSE also shows that the perovskite is evenly distributed over the entire surface of GCN. Interestingly, the $Cs_3Bi_2Br_9$ crystals detected by this technique appear much bigger than those revealed by TEM analysis. Although the spherical morphology is retained, their diameter now ranges from 100 nm to 900 nm. This inconsistency between the two sets of measures is likely to be attributed to an aggregation process between the NCs that occurs during the preparation of the composites. It is known, in fact, that the evaporation of solvent in colloidal suspensions can induce a self-assembly of the nanocrystals.[195] Since the formation of nano-$Cs_3Bi_2Br_9$/g-C_3N_4 composites is based precisely on combining the two materials in a solvent and letting the liquid evaporate, it is reasonable to assume that, as their concentration increases, perovskites NCs undergo some

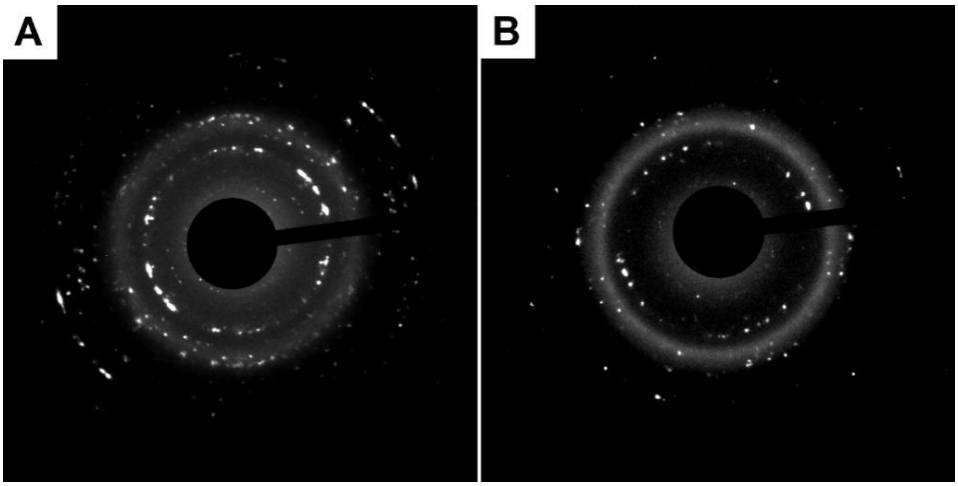

Figure 6.6 Electron diffraction images of (**A**) $Cs_3Bi_2Br_9$ and (**B**) $Cs_3Bi_2I_9$ nanocrystals.

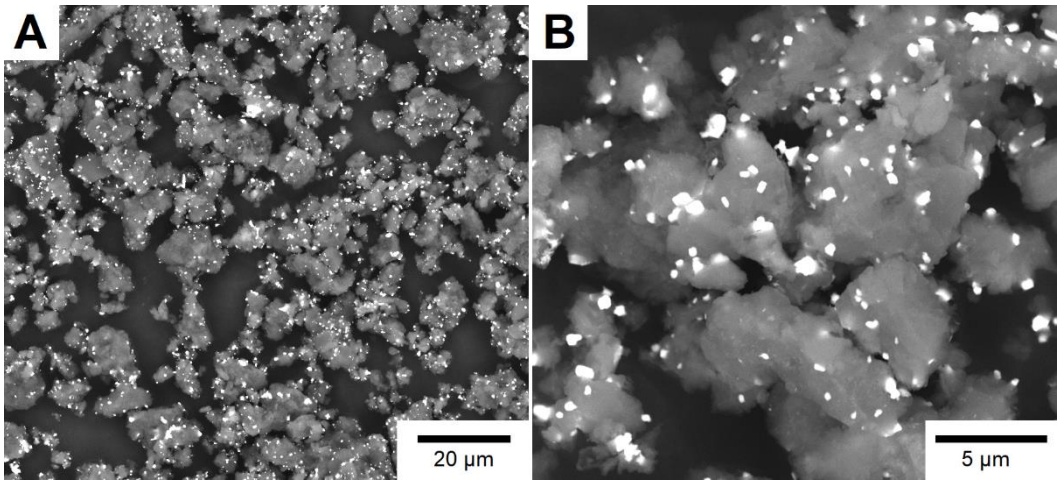

Figure 6.7 Backscattered electron images of the nano-$Cs_3Bi_2Br_9$/g-C_3N_4 composite with 5 wt% loading at (**A**) 2kx and (**B**) 10kx magnifications. The brighter spots represent the perovskite crystals.

assembling phenomenon that eventually leads to the formation of the large particles observed with BSE imaging.

6.3.3 Optical Characterization

The nanomaterials were optically characterized by UV-Visible absorption and steady-state photoluminescence spectroscopies. As reported in *Figure 6.8*, both Br- and I-based NCs exhibit strong absorption with a sharp edge. Most notably, they also present an intense exciton peak at 380 nm (3.23 eV) and 496 nm (2.50 eV), respectively. These spectra look very different from those of previous tin(IV) halide perovskites nanocrystals, which, conversely, had a less marked profile and a long Urbach tail. Since the exciton component to the absorption appear well separated from the contribution of continuum interband transitions, the Tauc plot of the spectra allowed to evaluate the gap energies of the two samples, as shown in *Figure 6.9 A*. Values of 3.63 eV and 2.72 eV are found respectively for the $Cs_3Bi_2Br_9$ and $Cs_3Bi_2I_9$ nanocrystals. These data are significantly higher than the gap energies reported for the corresponding bulk perovskites,[244] thus indicating a strong effect of quantum confinement on the properties of the

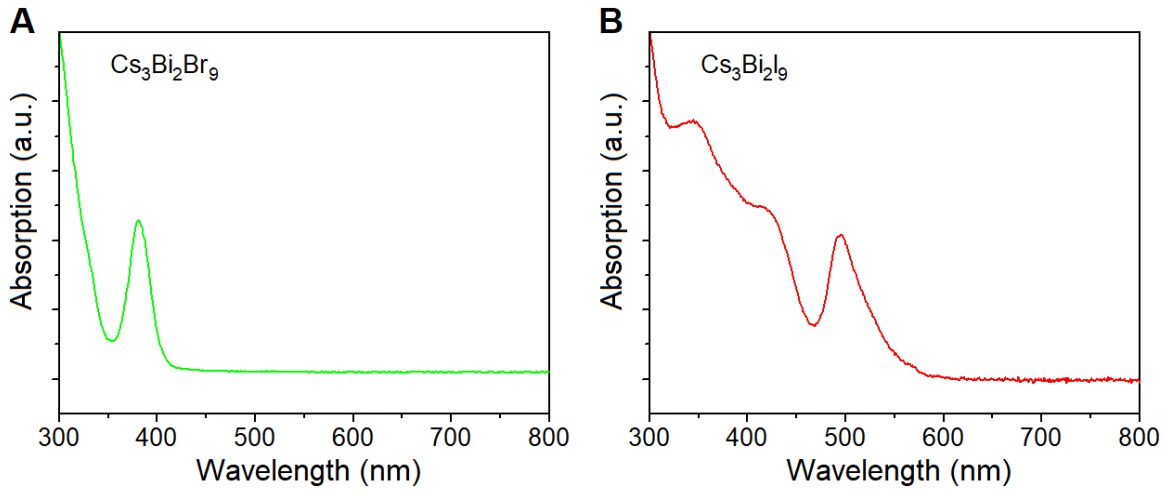

Figure 6.8 Absorption spectra of (**A**) $Cs_3Bi_2Br_9$ and (B) $Cs_3Bi_2I_9$ nanocrystals.

samples. This is consistent with the small crystal size revealed by TEM analysis and in line with previously reported results on BHP NCs.[269,277–279] In addiction, the difference between the exciton peak energy and the experimental bandgap gives an estimation of the exciton binding energy (the exact value would be obtained by fitting the absorption spectra according to the Elliott's model).[280,281] Although they are slightly lower than the data reported in some previous reports,[279,282] the values derived from the present measurements, of the order of 250 meV, are considerably high as expected due to the reduced structural dimensionality of the perovskites (see *Paragraph 6.1*).

Emission of light from the nanomaterials was investigated as well. $Cs_3Bi_2Br_9$ sample exhibit a blue photoluminescence peaking at 404 nm, with a FWHM of 86 nm (*Figure 6.9 B*).[269] As for the bandgap, the PL emission of the NCs reveals to be significantly blue-shifted with respect to the analogous bulk perovskite, which shows an emission around 475 nm.[259,269] This phenomenon is to be attributed once again to quantum confinement effects owing to the small crystal size, and it appears comparable or even amplified if compared with the results previously reported on this nanomaterial.[267,269,270,277,278] Surprisingly, $Cs_3Bi_2I_9$ sample shows no emission of light. The lack of PL from the I-based NCs could be explained with the presence of unpassivated defect states that quenches the radiative recombination processes. Bismuth iodide perovskites are known to have very low quantum yields and the mechanisms underlying that, as well as the origin of their luminescence in general, are still scarcely understood.[244] The

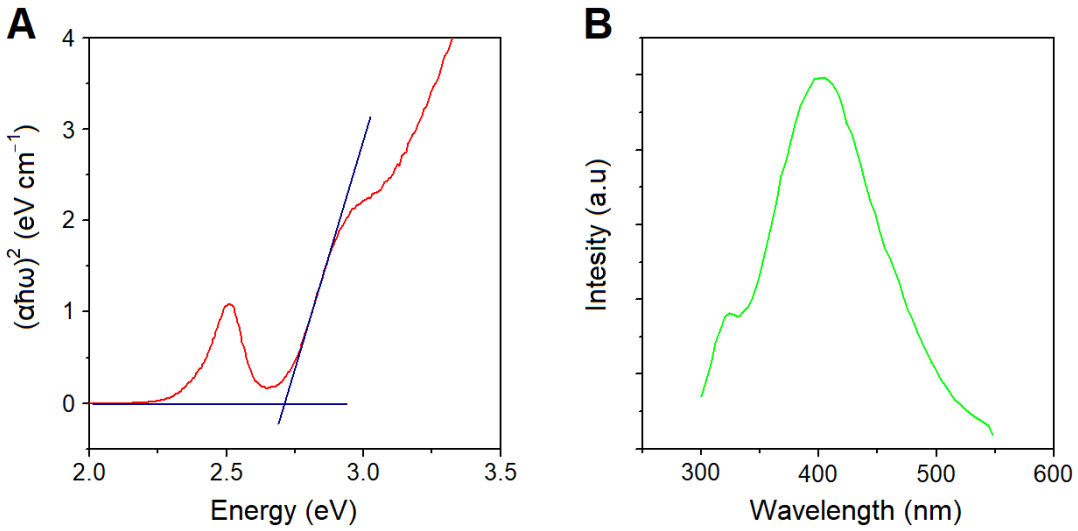

Figure 6.9 (**A**) Representative Tauc plot of the absorption spectrum of $Cs_3Bi_2I_9$ nanocrystals. (**B**) Photoluminescence spectrum of $Cs_3Bi_2Br_9$ nanocrystals.

main causes of the poor QY are believe to be surface defects, exciton self-trapping and non-radiative recombination paths favored by an indirect bandgap.[244,248,267,283]

The nano-$Cs_3Bi_2Br_9$/g-C_3N_4 composites were also optically characterized through absorption measures, and the resulting spectra are reported in *Figure 6.10*. The spectrum of pure g-C_3N_4 presents a broad peak around 400 nm and a long tail starting to raise from 600 nm. From the Tauc plot, the bandgap of GCN was evaluated to be 2.69 eV which is in perfect agreement with literature.[262,274] Composites with loadings of 1 wt% and 5 wt% exhibit essentially the same profile. The absorption peak at 400 nm appears a little more pronounced and sharper, likely due to the strong excitonic absorption of the perovskite that adds up to the total spectrum, but the variations are actually very small. The 10% composite, instead, shows the clear appearance of a new peak around 440 nm. Since the absorption spectrum of $Cs_3Bi_2Br_9$ NCs is completely flat at those wavelengths, this finding appears quite surprising.

This phenomenon could be related to the different magnitude of the perovskite crystals in the composites. Since the size of $Cs_3Bi_2Br_9$ NCs increases during the formation of the composites, as demonstrated by the TEM analysis, the quantum confinement effects might become less pronounced and the absorption might red-shift consequently, showing more bulk-like features. In fact, the absorption bulk $Cs_3Bi_2Br_9$ starts around 450 nm.[284] On the other hand,

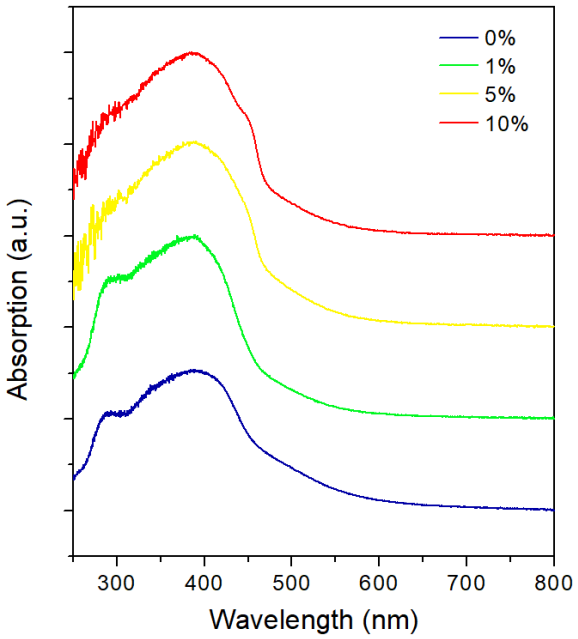

Figure 6.10 Absorption spectra of nano-$Cs_3Bi_2Br_9$/g-C_3N_4 composites with different perovskite loadings. (Curves were shifted vertically for clarity).

this phenomenon could also be an indication of a more complex interaction between the perovskite and the host material that requires further investigations to be fully unraveled.

6.3.4 Hydrogen Evolution

The GCN composites were eventually tested as photocatalysts in the production of hydrogen. The experiments were conducted according to the methodology reported in *Appendix A*, and the results are reported in *Figure 6.11*. At a loading of 1 wt%, the composite achieves the maximum photocatalytic activity, reaching a hydrogen evolution rate (HER) of 1495 μmol g^{-1} h^{-1}. This value is not only higher than the HER of pure GCN (81 μmol g^{-1} h^{-1}), but it is also higher than the previously reported HER for the analogous composite prepared with bulk perovskite (~1050 μmol g^{-1} h^{-1}). This finding confirms the synergistic effect between $Cs_3Bi_2Br_9$ and g-C_3N_4 in the photoreaction and demonstrates that the size reduction of the perovskite can in fact improve this effect by almost 50%.

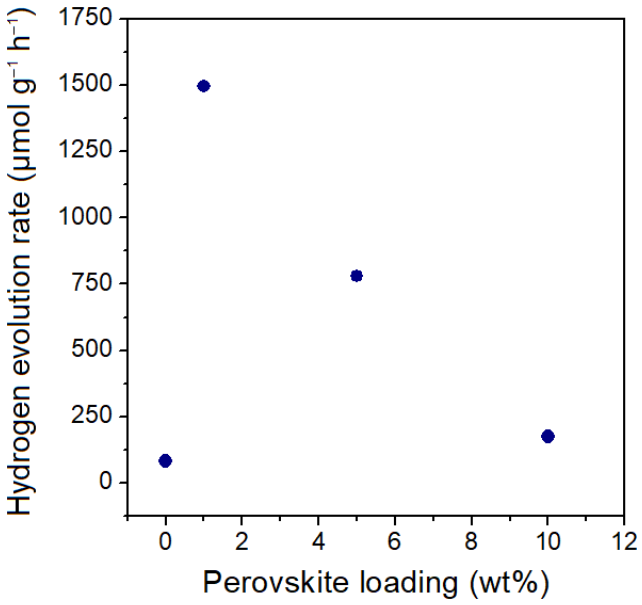

Figure 6.11 Hydrogen evolution rate for nano-$Cs_3Bi_2Br_9$/g-C_3N_4 composites at different percentages of perovskite loading in 10% (v/v) triethanolamine aqueous solution with platinum as co-catalyst, after 6 hours of irradiation under simulated solar light.

The exact origin of this enhancement is unclear and may be attributed to different factors or a combination of them. The first factor is the increase in the surface area. Despite their aggregation, the perovskite crystals exhibit nevertheless a submicron diameter, which is considerably smaller with respect to the bulk material. The reduced size results then in a larger surface area that can affect the photocatalysis. The second factor is related to the electronic structure of NCs. As previously reported, the photocatalytic boost of GCN coupled with $Cs_3Bi_2Br_9$ derives from a fortuitous alignment of their energy bands that grants an effective charge separation.[259] Since nanomaterials display a different electronic structure compared to their macroscopic form due to quantum confinement effects, it is possible that size reduction alters the band alignment and achieves an even better configuration that favors the separation of photogenerated charge carriers. Another factor that may play a role is the appearance of new localized deep states at the interface between the $Cs_3Bi_2Br_9$ and GCN that could act as catalytic sites. Due to the increased surface area of the perovskite, the concentration of such states should be higher and so their impact on the performance of the composites should become

greater.

It is worth to note that the HER of the 10% composite is lower than that reported for the counterpart prepared with bulk perovskite. The drop in the composite photocatalytic activity at high loadings was attributed to the self-trapping of electrons inside $Cs_3Bi_2Br_9$, whose detrimental effects become more and more pronounced as the perovskite content increases.[259] Since in nanomaterials the electron–phonon coupling is stronger,[285] it is reasonable to assume that in the present case the influence of self-trapping is more impactful because of the reduced crystal size of the perovskite, and so it causes a greater reduction of the HER. In this context, this result appears consistent with previous literature.

6.4 Conclusions

In summary, the synthesis of $Cs_3Bi_2X_9$ nanocrystals (X = Br, I) is reported using a simple ling-assisted reprecipitation method. The synthetic procedure is conducted under ambient conditions, does not require high temperatures and is free from toxic compounds, like phosphines, that are generally used in the synthesis of tin halide perovskite NCs. Both samples exhibit a homogeneous spherical morphology but a different tendency to agglomeration: the bromide-based material present well-dispersed particles with a diameter of about 2 nm, while the iodide-based material present aggregated particles with a diameter of 3.5 nm.

The crystal lattice of the two BHPs proves to be consistent with previous literature, namely $Cs_3Bi_2Br_9$ NCs are characterized by a trigonal 2D structure where $Cs_3Bi_2I_9$ NCs are characterized by a hexagonal 0D structure. The reduced dimensionality of the crystals has a sizable impact on their optical properties. Both samples, in fact, show a strong exciton peak in the absorption spectra at 380 nm and 496 nm, respectively, and high exciton binding energies of hundreds of meV. Moreover, due to strong quantum confinement effects, their gap energies reveal to be much higher than those of the related bulk compound, reaching values of 3.63 eV

and 2.50 eV. As regards photoluminescence, $Cs_3Bi_2Br_9$ NCs exhibit an emission at 404 nm with a FWHM of 86 nm. On the other hand, the luminescence of $Cs_3Bi_2I_9$ NCs is totally suppressed. This unexpected result is most likely caused by the presence of unpassivated defects that introduce deep electronic states.

The photocatalytic properties of $Cs_3Bi_2Br_9$ nanocrystals were also investigated in combination with graphitic carbon nitride: the two materials are combined to form composites with different perovskite loadings that are subsequently used in the photogeneration of hydrogen as catalysts. Although few points were taken, the initialresults show already a remarkable enhancement of the photocatalytic activity of nano-$Cs_3Bi_2Br_9$/g-C_3N_4 composites as the crystal size of $Cs_3Bi_2Br_9$ is reduced. In fact, the sample with 1 wt% of BHP proves to achieve a hydrogen evolution rate of 1495 μmol g^{-1} h^{-1}, which is 50% higher than the best value previously reported. The origin of this boost is still unknown, and more investigations are needed to fully discover the mechanisms behind that. Nevertheless, this finding sets a good starting point to further develop the research on GCN nanocomposites prepared with lead-free perovskites.

Chapter VII
CONCLUSIONS AND OUTLOOK

In summary, the present thesis reports the synthesis of different inorganic lead-free halide perovskites in the form of colloidal nanocrystals and the results of their structural, morphological, and optical characterization. Lead halide perovskites are one of the most interesting class of semiconductors of the last years, however the presence of toxic lead drastically restricts their applicability in daily life. For this reason, the investigation of new lead-free compounds is essential for the future development of the research and the technology based on MHPs. In the present work, lead was replaced with heterovalent metals. This substitution alters the regular perovskite lattice and leads to the formation of perovskite derivatives with a reduced structural dimensionality.

The first compounds reported are tin(IV) halide perovskites. These materials are characterized by a 0D vacancy-ordered structure since lead is replaced with a tetravalent element. Using an optimized hot-injection method, colloidal nanocrystals of the entire halide series Cs_2SnX_6 (X = I, Br, Cl) were synthesized. Notably, this is the first time that Cs_2SnBr_6 and mixed $Cs_2Sn(I/Br)_6$ are synthesized in the form of nanocrystals. X-ray diffraction (XRD) analysis proved the formation of all the compounds, which are single-phase and show no impurities. From transmission electron microscopy (TEM) images, the crystals revealed to have a spherical shape with a diameter of 3-6 nm and narrow size distributions. The optical characterization also showed a modulation of the optical properties as a function of the halide content: the bandgap changed from 1.57 eV for Cs_2SnI_6 to 3.86 eV for Cs_2SnCl_6, while the photoluminescence

peak ranged from 790 nm to 444 nm, respectively.

Afterwards, the impact of different ligands on tin(IV) halide perovskite was investigated. The commonly used oleylamine was replaced with shorter amines, ranging from hexylamine to dodecylamine, in the synthesis of Cs_2SnBr_6 and Cs_2SnI_6 nanocrystals to discover how molecules with variable length can affect the morphology and optical properties of the materials. This substitution had a dramatic impact on the shape and size of the crystals because it led to the formation of two dimensional nanoplatelets. Besides the morphology, the ligands also affected the optical properties of the perovskites. The bandgap of the nanoplatelets was significantly higher than that of their bulk counterpart, likely due to the strong quantum confinement effect that typically occurs in 2D layered nanostructures, and it grew linearly with the amine length. On the other hand, moving from NCs to nanoplatelets, the PL emission shifted from 603 nm to 575 nm in the case of Cs_2SnBr_6 and from 790 nm to 628 nm in the case of Cs_2SnI_6.

Finally, a different family of lead-free compounds was reported: bismuth halide perovskites. In this case, the substitution of lead with a trivalent element does not lead to a unique result. In fact, $Cs_3Bi_2Br_9$ presents a 2D vacancy-ordered structure, while $Cs_3Bi_2I_9$ presents a 0D dimer structure. Using a ligand-assisted reprecipitation method, NCs of $Cs_3Bi_2X_9$ (X = Br, I) were synthesized, as confirmed by the XRD measurements. Both samples exhibit a spherical morphology with a dimeter of about 2 nm for $Cs_3Bi_2Br_9$ and 3.5 nm for $Cs_3Bi_2I_9$ perovskite. Besides, the NCs showed strong and sharp absorption with a clear exciton peak at 380 nm and 496 nm, respectively, but only the bromide-based crystals exhibited luminescence.

The use of BHP NCs in photocatalysis was also reported to show a hint of possible applications for these materials. Specifically, $Cs_3Bi_2Br_9$ NCs were combined with graphitic carbon nitride to form composites that were later employed as photocatalyst in the generation of hydrogen. Since bulk $Cs_3Bi_2Br_9$ was proved to enhance the photocatalytic activity of g-C_3N_4, the idea was to investigate the effects of the perovskite size reduction on the photoreactions. The composites were prepared with different weight ratios between NCs and GCN to find the best composition to maximize the hydrogen production. Compared to the bulk form, the nanocrystalline perovskite revealed to increase the catalytic activity of the composite by almost 50%, reaching a peak value of 1495 $\mu mol\ g^{-1}\ h^{-1}$ of hydrogen. This remarkable result shows the

potentiality of these nanomaterials and paves the way for future research in the field of photocatalysis as well as other applications.

Despite these promising properties, however, lead-free MHP nanocrystals are still far from overcoming their lead-based counterpart. In fact, they are affected by a series of drawbacks that dramatically compromise their performance. Instability over time is above all the most critical issue of these materials: their lability towards air, solvents, light irradiation, and temperature is a highly limiting factor that prevents them from any applications in real-life devices. Owing to its more stable oxidation state, tin(IV) should avoid the problems arising from oxidation and make tin halide perovskites more resistant against air. The use of this metal actually proved to enhance the stability of the NCs in comparison to their tin(II)-based analogs. Nevertheless, the samples also revealed to retain their optical features unchanged for just few days, which is still an unsatisfactory result. This suggests that the degradation of the nanomaterials follows more complex pathways that involve other elements beyond oxygen.[286] Another great disadvantage of lead-free MHPs are their poor optical properties. The crystals presented very low photoluminescence quantum yields; in fact some samples showed no emission at all. This phenomenon is likely related to high concentrations of crystal defects that introduce trap states acting as non-radiative recombination centers. Such an observation points out that much work must be devoted in the optimization of the synthesis in order to obtain defect-free NCs, but it also has a more profound implication because it suggests that these compounds may have a less pronounced defect-tolerant character. Therefore, extensive research is needed to better understand the intrinsic properties of these nanomaterials. Finally, some samples also showed a high tendency to random aggregation. This behavior undermines the colloidal stability of the crystals in suspension and can lead to sintering. Therefore, if occurs in an uncontrollable and disordered way, it may prove problematic for the fabrication and functioning of electronic devices, especially those operating at high temperatures.[287,288]

Albeit with the problems encountered, the present thesis provides new insight on the synthesis, properties, and potentiality of lead-free MHP NCs and marks a new step in the research towards more sustainable technologies.

Appendix A
EXPERIMENTAL SECTION

A.1 Chemicals

Cesium carbonate (Cs_2CO_3, Acros Organics, 99.995%), tin(IV) chloride ($SnCl_4$, Sigma-Aldrich, 99.995%), tin(IV) bromide ($SnBr_4$, Sigma-Aldrich, 99%), tin(IV) iodide (SnI_4, Sigma-Aldrich, 99.999%), 1-octadecene (ODE, Acros Organics, 90%), oleic acid (OA, VWR Chemicals, 81%), oleylamine (OLA, Acros Organics, 80–90%), hexylamine (C6A, Sigma-Aldrich, ≥99%), octylamine (C8A, Sigma-Aldrich, 99%), decylamine (C10A, Sigma-Aldrich, 95%), dodecylamine (C12A, Sigma-Aldrich, 98%), hexane (Hex, Sigma-Aldrich ≥99%), ethanol (Eth, Sigma-Aldrich, 96%), anhydrous chloroform (Chl, Sigma-Aldrich, ≥99%, stabilized with ethanol), dicyandiamide (DCD, Sigma-Aldrich, 99%), triethanolamine (TEOA, Sigma-Aldrich, ≥99%), chloroplatinic acid (H_2PtCl_6, Sigma-Aldrich, 38% Pt basis), argon (Ar, Sapio, 99.999%,).

All reagents were used without further purification.

A.2 Syntheses

A.2.1 Synthesis of Cesium Oleate

For the synthesis of Cs_2SnX_6 nanocrystals (X = Cl, Br, $Br_{0.5}I_{0.5}$, I), a solution of cesium oleate was prepared by loading 15 mL of ODE in a 50 mL three-neck flask along with 0.5 mL of OA and 0.5 mL of OLA, and drying the mixture under vacuum for 1 hour at 120 °C. After that, 0.1625 g of cesium carbonate was added to the liquids and the solution was dried again under vacuum at the same temperature for 1 additional hour. Finally, the flask was heated at 150 °C under nitrogen flow until complete dissolution of Cs_2CO_3 (approximately 1 hour). The resulting solution was stored under nitrogen atmosphere.

In the case of tin(IV)-based crystals with amines different from OLA, the synthesis of Cs-oleate was conducted in the same way but without oleylamine.

Since Cs-oleate is insoluble in ODE at room temperature, the solution was preheated at 120 °C before use to completely dissolve the precipitate.

A.2.2 Synthesis of Graphitic Carbon Nitride

Graphitic carbon nitride was synthesized from the thermal polymerization of dicyandiamide. The precursor was slowly heated to 550 °C with at a rate of 1 °C min^{-1}, and the temperature was maintained for 4 hours. After that, the resulting product was cooled down to room temperature with a rate of 10 °C min^{-1}. The synthesis was conducted under nitrogen flux in a partially closed alumina crucible.

A.3 Characterization Techniques

A.3.1 X-Ray Diffraction

X-ray diffraction (XRD) investigations were carried out under ambient condition on a Bruker D8 Advance diffractometer using copper Kα radiation (λ = 1.54056 Å) as X-ray source. The measurements were performed in the Bragg-Brentano configuration, with resolution of 0.04° and integration time of 4 seconds The reference patterns were calculated with PowderCell 2.4 software using the literature data specified in the text as references. Lattice parameters were determined from Rietveld refinement of the diffraction pattern.

In the case of tin(IV)-based samples with amines different from OLA, the specimens were prepared by depositing the crystals on a glass slide with a spatula and spreading it thoroughly in order to get a smooth surface. In the case of bismuth-based samples, the specimens were prepared by dropping the sample dispersed in Chl on a glass slide and letting the solvent evaporate.

A.3.2 Transmission Electron Microscopy

Transmission electron microscopy (TEM) was performed on a JEOL JEM-1200 EX II microscope operating at 100 kV, equipped with a tungsten filament as electron source. The specimens were prepared by depositing 8 μL of the crystals dispersed in suspension on an aluminum grid covered with a polymeric film and letting the solvent evaporate under ambient conditions. The size distribution of the samples was calculated from TEM images using ImageJ software.

A.3.3 High Resolution Transmission Electron Microscopy

High resolution transmission electron microscopy (HRTEM) was performed on a ZEISS LIBRA200FE equipped with a high-angle annular dark-field (HAADF) detector for STEM (scanning TEM) mode. Energy dispersive X-ray (EDX) analysis was conducted on the same instrument using an Oxford X-stream 2 probe. The specimens were prepared by depositing 8 µL of the crystals dispersed in suspension on a copper grid covered with a double carbon film and letting the solvent evaporate in air.

A.3.4 Backscattered Electron Imaging

Backscattered electron (BSE) imaging was carried out on a TESCAN Mira3 scanning electron microscope (SEM) operated at 20 kV. The instrument was equipped with a Schottky field effect gun (FEG) as electron source and an annular single-crystal YAG scintillator as detector.

A.3.5 Absorption Spectroscopy

In the case of Cs_2SnX_6 nanocrystals (X = Cl, Br, $Br_{0.5}I_{0.5}$, I), UV–Visible–NIR absorption measurements were performed under ambient conditions using a Varian Cary 6000i spectrophotometer equipped with a double monochromator, a deuterium lamp and a tungsten filament lamp as light sources, a photomultiplier (for UV-Vis) and an InGaAs photodiode (for NIR) as detectors. Spectral range was 280–1800 nm, in step of 2 nm. The specimens were prepared by depositing the NCs on a glass slide and covering them with a glass coverslip. The baseline was taken using the glass slide as reference.

In the case of tin(IV)-based samples with amines different from OLA, UV-Visible absorption measurements were performed under ambient conditions using a Varian Cary 50 spectrophotometer equipped with a Xe lamp as light source, a silicon photodiode as detector

and a Czerny-Turner monochromator with fixed spectral bandwidth of 1.5 nm. The spectra were recorded from 200 nm to 1000 nm, with resolution of 2 nm and integration time of 0.5 sec. The specimens were prepared by loading the samples into quartz cuvettes with 1 cm optical path. The baseline was taken using the cuvettes filled with Hex as reference.

In the case of $Cs_3Bi_2X_9$ nanocrystals (X = Br, I), UV-Visible absorption measurements were performed under ambient conditions using the previous Varian Cary 50 spectrophotometer from 300 nm to 800 nm, with resolution of 1 nm and integration time of 0.5 sec. The specimens were prepared by loading the samples into quartz cuvettes with 1 cm optical path. The baseline was taken using the cuvettes filled with Chl as reference.

In the case of nano-$Cs_3Bi_2Br_9$/g-C_3N_4 composites, UV-Visible absorption measurements were performed under ambient conditions using a Jasco V-750 spectrophotometer equipped with a Jasco ISV-922 integrating sphere. The spectra were recorded from 250 nm to 800 nm, with resolution of 1 nm. The specimens were prepared by loading the samples into quartz cuvettes with 1 mm optical path. The baseline was taken using a standard white plate.

A.3.6 Steady-State Photoluminescence Spectroscopy

In the case of Cs_2SnX_6 nanocrystals (X = Cl, Br, $Br_{0.5}I_{0.5}$, I), photoluminescence (PL) investigations were conducted under ambient conditions using a 355 nm laser line (PowerChip Microlaser) as excitation light source and a LN2-cooled silicon CCD (Princeton Instruments Spec-10:400) as detector. The specimens were prepared by depositing the NCs on a glass slide and covering them with a glass cover slip. Measurements were performed in transmission mode, with a resolution of 0.5 nm and an integration time of 5 seconds, using a longpass filter at 450 nm to remove the laser line from the PL signal. The background noise and the luminescence from the glass slide were subtracted from the spectra of the samples.

In the case of tin(IV)-based samples with amines different from OLA, PL measurements were performed under ambient conditions using a Varian Cary Eclipse fluorescence spectrophotometer equipped with Xe lamp as light source, a photomultiplier as detector and two Czerny-Turner monochromators with limiting resolution of 1.5 nm. The spectra were

recorded exciting the samples at 360 nm wavelength. The specimens were prepared by loading the samples into quartz cuvettes with 1 cm optical path.

In the case of $Cs_3Bi_2X_9$ nanocrystals (X = Br, I), PL measurements were performed under ambient conditions using the previous Varian Cary Eclipse fluorescence spectrophotometer exciting at 300 nm.

To find the emission peaks, the PL spectra were fitted with gaussian lineshapes using OriginLab Origin 8.1 software.

A.3.7 Photoluminescence Quantum Yield

Photoluminescence quantum yield (QY) measurements were performed on the samples dispersed in Hex into quartz cuvettes (1 cm optical path) using a Varian Cary Eclipse Fluorescence Spectrophotometer with an excitation wavelength of 350 nm. Rhodamine B and Rhodamine 6G dissolved in ethanol were used as standards to calculate the QY values for all the samples.

A.4 Hydrogen Evolution

To conduct the photocatalysis experiments, 0.0240 g of the nano-$Cs_3Bi_2Br_9$/g-C_3N_4 composite under study was loaded into a 28 mL Pyrex glass container along with 24 mL of a 10% (v/v) solution of triethanolamine in tridistilled water. The mixture was deoxygenated by argon bubbling for 20 min to obtain anoxic conditions. Afterwards, 42 µL of a 15 g L^{-1} aqueous solution of chloroplatinic acid was added to the photoreactor, and the mixture was deoxygenated with Ar bubbling for additional 3 min. The addition of H_2PtCl_6 allows the in situ photodeposition of platinum on the composite surface, which acts as co-catalyst during the

reaction. Finally, the container was closed with sleeve stopper septa and sealed with parafilm.

The irradiation of the samples was conducted with simulated solar light (300–800 nm) using a CO.FO.ME.GRA Solar Box 1500e equipped with a 1500 W xenon lamp and an outdoor UV filter made of IR-treated soda lime glass. The box was set at a power factor of 500 W m^{-2}, and the irradiation was performed for 6 hours under magnetic stirring. The apparent photon flux of the instrument was experimentally determined by 2-nitrobenzaldehyde actinometry over the wavelength range 300–410 nm according to the methodology reported in literature,[289] and a value of $1.53 \cdot 10^{-7}$ photon moles per second was found.

The amount of evolved hydrogen was quantified through gas chromatography (GC) using a DANI 3600 gas chromatograph equipped with a thermal conductivity detector (TCD) and interfaced with a Shimadzu C-R3A recorder.

BIBLIOGRAPHY

[1] G. E. Moore, 'Cramming More Components onto Integrated Circuits' *Electronics* 38, 8, 114 (1965).

[2] L. Łukasiak, A. Jakubowski, 'History of Semiconductors' *J. Telecommun. Inf. Technol.* 1, 3–9 (2010).

[3] Semiconductor Industry from 2015 to 2025, *SEMI*, https://www.semi.org/en/semiconductor-industry-2015-2025 (accessed Jan. 2022).

[4] S. Narayanan et al., 'Metal Halide Perovskites for Energy Storage Applications' *Eur. J. Inorg. Chem.* 2021, 13, 1201–1212 (2021).

[5] H. Huang et al., 'Solar-Driven Metal Halide Perovskite Photocatalysis: Design, Stability, and Performance' *ACS Energy Lett.* 5, 4, 1107–1123 (2020).

[6] F. Li et al., 'Emerging Transistor Applications Enabled by Halide Perovskites' *Accounts Mater. Res.* 3, 1, 8–20 (2022).

[7] J. Li et al., 'Review on Recent Progress of Lead-Free Halide Perovskites in Optoelectronic Applications' *Nano Energy* 80, 105526 (2021).

[8] S. Arya et al., 'A Comprehensive Review on Synthesis and Applications of Single Crystal Perovskite Halides' *Prog. Solid State Chem.* 60, 100286 (2020).

[9] V. Adinolfi et al., 'The Electrical and Optical Properties of Organometal Halide Perovskites Relevant to Optoelectronic Performance' *Adv. Mater.* 30, 1, 1700764 (2018).

[10] F. J. Iftikhar et al., 'Structural and Optoelectronic Properties of Hybrid Halide Perovskites for Solar Cells' *Org. Electron.* 91, 106077 (2021).

[11] H. M. Jang et al., 'Enhancing Photoluminescence Quantum Efficiency of Metal Halide Perovskites by Examining Luminescence-Limiting Factors' *APL Mater.* 8, 2, 020904 (2020).

[12] M. Mittal et al., 'Size of the Organic Cation Tunes the Bandgap of Colloidal Organolead Bromide Perovskite Nanocrystals' *J. Phys. Chem. Lett.* 7, 16, 3270–3277 (2016).

[13] I. E. Castelli et al., 'Bandgap Calculations and Trends of Organometal Halide Perovskites' *APL Mater.* 2, 8, 081514 (2014).

[14] F. Brivio et al., 'Relativistic Quasiparticle Self-Consistent Electronic Structure of Hybrid Halide Perovskite Photovoltaic Absorbers' *Phys. Rev. B* 89, 15, 155204 (2014).

[15] H. Topsoe, 'No Title' *Overs. K. Dan. Vidensk. Selsk. Forh.* 8, 247 (1882).

[16] H. L. Wells, 'Über die Cäsium- und Kalium-Bleihalogenide' *Zeitschrift für Anorg. Chemie* 3, 1, 195–210 (1893).

[17] D. B. Mitzi et al., 'Conducting Tin Halides with a Layered Organic-Based Perovskite Structure' *Nature* 369, 6480, 467–469 (1994).

[18] D. B. Mitzi et al., 'Conducting Layered Organic-Inorganic Halides Containing ⟨110⟩-Oriented Perovskite Sheets' *Science* 267, 5203, 1473–1476 (1995).

[19] D. B. Mitzi et al., 'Transport, Optical, and Magnetic Properties of the Conducting Halide Perovskite $CH_3NH_3SnI_3$' *J. Solid State Chem.* 114, 1, 159–163 (1995).

[20] C. R. Kagan et al., 'Organic-Inorganic Hybrid Materials as Semiconducting Channels in Thin-Film Field-Effect Transistors' *Science* 286, 5441, 945–947 (1999).

[21] D. B. Mitzi et al., 'Structurally Tailored Organic-Inorganic Perovskites: Optical Properties and Solution-Processed Channel Materials for Thin-Film Transistors' *Chem. Mater.* 13, 10, 3728–3740 (2001).

[22] N. S. Kumar, K. C. B. Naidu, 'A Review on Perovskite Solar Cells (PSCs), Materials and Applications' *J. Mater.* 7, 5, 940–956 (2021).

[23] Best Research-Cell Efficiency Chart, *National Renewable Energy Laboratory*, https://www.nrel.gov/pv/cell-efficiency.html (accessed Jan. 2022).

[24] A. Kojima et al., 'Organometal Halide Perovskites as Visible-Light Sensitizers for

Photovoltaic Cells' *J. Am. Chem. Soc.* 131, 17, 6050–6051 (2009).

[25] B. S. Murty et al., *Textbook of Nanoscience and Nanotechnology*, Springer Berlin Heidelberg, Berlin, Heidelberg (2013).

[26] Quantum Dots for Micro-LED Displays, *IDTechEx*, https://www.idtechex.com/en/webinar/quantum-dots-for-micro-led-displays/315 (accessed May 2022).

[27] S. Talebian et al., 'Facts and Figures on Materials Science and Nanotechnology Progress and Investment' *ACS Nano* 15, 10, 15940–15952 (2021).

[28] What are Nanomaterials?, *Nanowerk*, https://www.nanowerk.com/what-are-nanomaterials.php (accessed May 2022).

[29] S. Kumar, T. Nann, 'Shape Control of II–VI Semiconductor Nanomaterials' *Small* 2, 3, 316–329 (2006).

[30] C. Burda et al., 'Chemistry and Properties of Nanocrystals of Different Shapes' *Chem. Rev.* 105, 4, 1025–1102 (2005).

[31] Z. Liu et al., 'Shape Control in the Synthesis of Colloidal Semiconductor Nanocrystals' in *Anisotropic Particle Assemblies* (editors N. Wu, D. Lee, A. Striolo), Elsevier, Amsterdam (2018).

[32] X.-L. Yu et al., 'Synthesis and Sensing Properties of ZnO/ZnS Nanocages' *Nanoscale Res. Lett.* 5, 3, 644–648 (2010).

[33] F. Zhang et al., 'Brightly Luminescent and Color-Tunable Colloidal $CH_3NH_3PbX_3$ (X = Br, I, Cl) Quantum Dots: Potential Alternatives for Display Technology' *ACS Nano* 9, 4, 4533–4542 (2015).

[34] L. Protesescu et al., 'Nanocrystals of Cesium Lead Halide Perovskites ($CsPbX_3$, X = Cl, Br, and I): Novel Optoelectronic Materials Showing Bright Emission with Wide Color Gamut' *Nano Lett.* 15, 6, 3692–3696 (2015).

[35] A. Dey et al., 'State of the Art and Prospects for Halide Perovskite Nanocrystals' *ACS Nano* 15, 7, 10775–10981 (2021).

[36] J. Shamsi et al., 'Metal Halide Perovskite Nanocrystals: Synthesis, Post-Synthesis Modifications, and Their Optical Properties' *Chem. Rev.* 119, 5, 3296–3348 (2019).

[37] S. Lou et al., 'Stability: a Desiderated Problem for the Lead Halide Perovskites' *Opt.*

Mater. X 1, 100023 (2019).

[38] S. Mazumdar et al., 'Stability of Perovskite Solar Cells: Degradation Mechanisms and Remedies' *Front. Electron.* 2, 8 (2021).

[39] A. C. Ufelle, A. Barchowsky, 'Toxic Effects of Metals' in *Casarett and Doull's Toxicology: the Basic Science of Poisons* (editor C. D. Klaassen), 9th edition, McGraw-Hill Education, New York (2019).

[40] K. Rehman et al., 'Prevalence of Exposure of Heavy Metals and Their Impact on Health Consequences' *J. Cell. Biochem.* 119, 1, 157–184 (2018).

[41] M. Balali-Mood et al., 'Toxic Mechanisms of Five Heavy Metals: Mercury, Lead, Chromium, Cadmium, and Arsenic' *Front. Pharmacol.* 12, 227 (2021).

[42] E. Silbergeld, 'Facilitative Mechanisms of Lead as a Carcinogen' *Mutat. Res. Mol. Mech. Mutagen.* 533, 1–2, 121–133 (2003).

[43] A. L. Wani et al., 'Lead Toxicity: a Review' *Interdiscip. Toxicol.* 8, 2, 55–64 (2015).

[44] M. Ren et al., 'Potential Lead Toxicity and Leakage Issues on Lead Halide Perovskite Photovoltaics' *J. Hazard. Mater.* 426, 127848 (2022).

[45] B. Hailegnaw et al., 'Rain on Methylammonium Lead Iodide Based Perovskites: Possible Environmental Effects of Perovskite Solar Cells' *J. Phys. Chem. Lett.* 6, 9, 1543–1547 (2015).

[46] J. Li et al., 'Biological Impact of Lead from Halide Perovskites Reveals the Risk of Introducing a Safe Threshold' *Nat. Commun.* 11, 1, 310 (2020).

[47] F. Zhang et al., 'Recent Advances and Opportunities of Lead-Free Perovskite Nanocrystal for Optoelectronic Application' *Energy Mater. Adv.* 2021, 1–38 (2021).

[48] Q. Xie et al., 'Branched Capping Ligands Improve the Stability of Cesium Lead Halide ($CsPbBr_3$) Perovskite Quantum Dots' *J. Mater. Chem. C* 7, 36, 11251–11257 (2019).

[49] Y. Gao et al., 'Lead-Free Halide Perovskites: a Review of the Structure–Property Relationship and Applications in Light-Emitting Devices and Radiation Detectors' *J. Mater. Chem. A* 9, 20, 11931–11943 (2021).

[50] S. F. Hoefler et al., 'Progress on Lead-Free Metal Halide Perovskites for Photovoltaic Applications: a Review' *Monatshefte für Chemie - Chem. Mon.* 148, 5, 795–826 (2017).

[51] S. Thomas, A. Thankappan, *Perovskite Photovoltaics*, Elsevier, Amsterdam (2018).

[52] G. Grancini, M. K. Nazeeruddin, 'Dimensional Tailoring of Hybrid Perovskites for Photovoltaics' *Nat. Rev. Mater.* 4, 1, 4–22 (2019).

[53] C. Artini, 'Crystal Chemistry, Stability and Properties of Interlanthanide Perovskites: a Review' *J. Eur. Ceram. Soc.* 37, 2, 427–440 (2017).

[54] G. George et al., *Fundamentals of Perovskite Oxides: Synthesis, Structure, Properties and Applications*, CRC Press, Boca Raton, Florida (2020).

[55] E. A. R. Assirey, 'Perovskite Synthesis, Properties and Their Related Biochemical and Industrial Application' *Saudi Pharm. J.* 27, 6, 817–829 (2019).

[56] R. Sarmiento-Pérez et al., 'Prediction of Stable Nitride Perovskites' *Chem. Mater.* 27, 17, 5957–5963 (2015).

[57] A. Fuertes, 'Chemistry and Applications of Oxynitride Perovskites' *J. Mater. Chem.* 22, 8, 3293–3299 (2012).

[58] P. Schouwink et al., 'Structure and Properties of Complex Hydride Perovskite Materials' *Nat. Commun.* 5, 1, 1–10 (2014).

[59] T. Sato et al., 'Hydrides with the Perovskite Structure: General Bonding and Stability Considerations and the New Representative $CaNiH_3$' *J. Solid State Chem.* 178, 11, 3381–3388 (2005).

[60] A. Swarnkar et al., 'Are Chalcogenide Perovskites an Emerging Class of Semiconductors for Optoelectronic Properties and Solar Cell?' *Chem. Mater.* 31, 3, 565–575 (2019).

[61] D. Tiwari et al., 'Chalcogenide Perovskites for Photovoltaics: Current Status and Prospects' *J. Phys. Energy* 3, 3, 034010 (2021).

[62] M. Palummo et al., 'Halide Pb-Free Double Perovskites: Ternary vs. Quaternary Stoichiometry' *Energies* 13, 14, 3516 (2020).

[63] Z. Ma et al., 'Lead-Free Metal Halide Perovskites and Perovskite Derivatives as an Environmentally Friendly Emitter for Light-Emitting Device Applications' *J. Phys. Chem. Lett.* 11, 14, 5517–5530 (2020).

[64] J. Sun et al., 'Organic-Inorganic Metal Halide Perovskite Optoelectronic Devices beyond Solar Cells' *Adv. Sci.* 5, 5, 1700780 (2018).

[65] V. M. Goldschmidt, 'Die Gesetze der Krystallochemie' *Naturwissenschaften* 14, 21, 477–485 (1926).

[66] M. R. Filip, F. Giustino, 'The Geometric Blueprint of Perovskites' *Proc. Natl. Acad. Sci.* 115, 21, 5397–5402 (2018).

[67] H. D. Megaw, *Crystal Structures: a Working Approach*, W.B. Saunders Company, Philadelphia (1973).

[68] W. Travis et al., 'On the Application of the Tolerance Factor to Inorganic and Hybrid Halide Perovskites: a Revised System' *Chem. Sci.* 7, 7, 4548–4556 (2016).

[69] G. Kieslich et al., 'An Extended Tolerance Factor Approach for Organic-Inorganic Perovskites' *Chem. Sci.* 6, 6, 3430–3433 (2015).

[70] T. Sato et al., 'Extending the Applicability of the Goldschmidt Tolerance Factor to Arbitrary Ionic Compounds' *Sci. Rep.* 6, 1, 23592 (2016).

[71] C. J. Bartel et al., 'New Tolerance Factor to Predict the Stability of Perovskite Oxides and Halides' *Sci. Adv.* 5, 2, (2019).

[72] S. Gholipour et al., 'Globularity-Selected Large Molecules for a New Generation of Multication Perovskites' *Adv. Mater.* 29, 38, 1702005 (2017).

[73] T. Lanigan-Atkins et al., 'Two-Dimensional Overdamped Fluctuations of the Soft Perovskite Lattice in $CsPbBr_3$' *Nat. Mater.* 20, 7, 977–983 (2021).

[74] M. W. Lufaso, P. M. Woodward, 'Jahn-Teller Distortions, Cation Ordering and Octahedral Tilting in Perovskites' *Acta Crystallogr. B* 60, Pt 1, 10–20 (2004).

[75] M. Johnsson, P. Lemmens, 'Crystallography and Chemistry of Perovskites' in *Handbook of Magnetism and Advanced Magnetic Materials* John Wiley & Sons, Ltd, Chichester, UK (2007).

[76] J.-H. Lee et al., 'Resolving the Physical Origin of Octahedral Tilting in Halide Perovskites' *Chem. Mater.* 28, 12, 4259–4266 (2016).

[77] K. L. Svane et al., 'How Strong Is the Hydrogen Bond in Hybrid Perovskites?' *J. Phys. Chem. Lett.* 8, 24, 6154–6159 (2017).

[78] S. Jin, 'Can We Find the Perfect A-Cations for Halide Perovskites?' *ACS Energy Lett.* 6, 9, 3386–3389 (2021).

[79] W. Dachraoui et al., 'Local Oxygen-Vacancy Ordering and Twinned Octahedral Tilting Pattern in the $Bi_{0.81}Pb_{0.19}FeO_{2.905}$ Cubic Perovskite' *Chem. Mater.* 24, 7, 1378–1385 (2012).

[80] P. Rajak et al., 'Evidence of Mn-Ion Structural Displacements Correlated with Oxygen Vacancies in $La_{0.7}Sr_{0.3}MnO_3$ Interfacial Dead Layers.' *ACS Appl. Mater. Interfaces* 13, 46, 55666–55675 (2021).

[81] T. Oku, 'Crystal Structures of $CH_3NH_3PbI_3$ and Related Perovskite Compounds Used for Solar Cells' in *Solar Cells - New Approaches and Reviews* IntechOpen, London (2015).

[82] M. C. Oliveira et al., 'Temperature Dependence on Phase Evolution in the $BaTiO_3$ Polytypes Studied Using Ab Initio Calculations' *Int. J. Quantum Chem.* 120, 1, e26054 (2020).

[83] C. Li et al., 'Formability of ABO_3 Perovskites' *J. Alloys Compd.* 372, 1–2, 40–48 (2004).

[84] A. Kumar et al., 'Prediction of Formability in Perovskite-Type Oxides' *Open Appl. Phys. J.* 1, 11–19 (2008).

[85] L. M. Feng et al., 'Formability of ABO_3 Cubic Perovskites' *J. Phys. Chem. Solids* 69, 4, 967–974 (2008).

[86] Z. Wang et al., 'Stability of Perovskite Solar Cells: a Prospective on the Substitution of the A Cation and X Anion' *Angew. Chem. Int. Ed.* 56, 5, 1190–1212 (2017).

[87] C. Li et al., 'Formability of ABX_3 (X = F, Cl, Br, I) Halide Perovskites' *Acta Crystallogr. B* 64, 6, 702–707 (2008).

[88] M. Becker et al., 'Formation of Hybrid ABX_3 Perovskite Compounds for Solar Cell Application: First-Principles Calculations of Effective Ionic Radii and Determination of Tolerance Factors' *Dalt. Trans.* 46, 11, 3500–3509 (2017).

[89] F. Dogan et al., 'Focus on Properties and Applications of Perovskites' *Sci. Technol. Adv. Mater.* 16, 2, 020301 (2015).

[90] C. Zhou et al., 'Low-Dimensional Metal Halide Perovskites and Hybrids' *Mater. Sci. Eng. R Reports* 137, 38–65 (2019).

[91] W. Gao et al., 'A-Site Cation Engineering of Metal Halide Perovskites: Version 3.0 of Efficient Tin-Based Lead-Free Perovskite Solar Cells' *Adv. Funct. Mater.* 30, 34, 2000794 (2020).

[92] J.-W. Lee et al., 'Rethinking the A Cation in Halide Perovskites' *Science* 375, 6583, (2022).

[93] Z. Gao et al., 'High Throughput Screening of Promising Lead-Free Inorganic Halide

Double Perovskites via First-Principles Calculations' *Phys. Chem. Chem. Phys.* 24, 5, 3460–3469 (2022).

[94] R. E. Brandt et al., 'Identifying Defect-Tolerant Semiconductors with High Minority-Carrier Lifetimes: beyond Hybrid Lead Halide Perovskites' *MRS Commun.* 5, 02, 265–275 (2015).

[95] S. Tao et al., 'Absolute Energy Level Positions in Tin- and Lead-Based Halide Perovskites' *Nat. Commun.* 10, 1, 2560 (2019).

[96] J. Even et al., 'Importance of Spin–Orbit Coupling in Hybrid Organic-Inorganic Perovskites for Photovoltaic Applications' *J. Phys. Chem. Lett.* 4, 17, 2999–3005 (2013).

[97] M. Hussain et al., 'Spin–Orbit Coupling Effect on Energy Level Splitting and Band Structure Inversion in $CsPbBr_3$' *J. Mater. Sci.* 56, 1, 528–542 (2021).

[98] L. Huang, W. R. L. Lambrecht, 'Electronic Band Structure Trends of Perovskite Halides: beyond Pb and Sn to Ge and Si' *Phys. Rev. B* 93, 19, 195211 (2016).

[99] Y. Su et al., 'Highly Controllable and Efficient Synthesis of Mixed-Halide $CsPbX_3$ (X = Cl, Br, I) Perovskite QDs toward the Tunability of Entire Visible Light' *ACS Appl. Mater. Interfaces* 9, 38, 33020–33028 (2017).

[100] K. T. Butler et al., 'Band Alignment of the Hybrid Halide Perovskites $CH_3NH_3PbCl_3$, $CH_3NH_3PbBr_3$ and $CH_3NH_3PbI_3$' *Mater. Horizons* 2, 2, 228–231 (2015).

[101] M. R. Filip et al., 'Steric Engineering of Metal-Halide Perovskites with Tunable Optical Bandgaps' *Nat. Commun.* 5, 1, 5757 (2014).

[102] A. Amat et al., 'Cation-Induced Bandgap Tuning in Organohalide Perovskites: Interplay of Spin–Orbit Coupling and Octahedra Tilting' *Nano Lett.* 14, 6, 3608–3616 (2014).

[103] Z. Xiao et al., 'Searching for Promising New Perovskite-Based Photovoltaic Absorbers: the Importance of Electronic Dimensionality' *Mater. Horizons* 4, 2, 206–216 (2017).

[104] C. Quarti et al., 'Structural and Optical Properties of Methylammonium Lead Iodide Across the Tetragonal to Cubic Phase Transition: Implications for Perovskite Solar Cells' *Energy Environ. Sci.* 9, 1, 155–163 (2016).

[105] H. Jin et al., 'It's a Trap! On the Nature of Localised States and Charge Trapping in Lead Halide Perovskites' *Mater. Horizons* 7, 2, 397–410 (2020).

[106] A. Zakutayev et al., 'Defect Tolerant Semiconductors for Solar Energy Conversion' *J.*

Phys. Chem. Lett. 5, 7, 1117–1125 (2014).

[107] A. Buin et al., 'Materials Processing Routes to Trap-Free Halide Perovskites' *Nano Lett.* 14, 11, 6281–6286 (2014).

[108] A. Filippetti, A. Mattoni, 'Hybrid Perovskites for Photovoltaics: Insights from First Principles' *Phys. Rev. B* 89, 12, 125203 (2014).

[109] A. Walsh, A. Zunger, 'Instilling Defect Tolerance in New Compounds' *Nat. Mater.* 16, 10, 964–967 (2017).

[110] S. J. Adjogri, E. L. Meyer, 'Chalcogenide Perovskites and Perovskite-Based Chalcohalide as Photoabsorbers: a Study of Their Properties, and Potential Photovoltaic Applications' *Materials* 14, 24, 7857 (2021).

[111] E. J. Juarez-Perez et al., 'Photoinduced Giant Dielectric Constant in Lead Halide Perovskite Solar Cells' *J. Phys. Chem. Lett.* 5, 13, 2390–2394 (2014).

[112] R. Su et al., 'Dielectric Screening in Perovskite Photovoltaics' *Nat. Commun.* 12, 1, 2479 (2021).

[113] I. Anusca et al., 'Dielectric Response: Answer to Many Questions in the Methylammonium Lead Halide Solar Cell Absorbers' *Adv. Energy Mater.* 7, 19, 1700600 (2017).

[114] M. H. Du, 'Efficient Carrier Transport in Halide Perovskites: Theoretical Perspectives' *J. Mater. Chem. A* 2, 24, 9091–9098 (2014).

[115] R. H. Bube, *Photoelectronic Properties of Semiconductors*, Cambridge University Press, Cambridge (1992).

[116] J. N. Wilson et al., 'Dielectric and Ferroic Properties of Metal Halide Perovskites' *APL Mater.* 7, 1, 010901 (2019).

[117] Y. Jiang et al., 'Properties of Excitons and Photogenerated Charge Carriers in Metal Halide Perovskites' *Adv. Mater.* 31, 47, 1806671 (2019).

[118] J. M. Frost, A. Walsh, 'What Is Moving in Hybrid Halide Perovskite Solar Cells?' *Acc. Chem. Res.* 49, 3, 528–535 (2016).

[119] J. Haruyama et al., 'First-Principles Study of Ion Diffusion in Perovskite Solar Cell Sensitizers' *J. Am. Chem. Soc.* 137, 32, 10048–10051 (2015).

[120] A. Slonopas et al., 'Role of the Colossal Frequency and Temperature Dependent

Dielectric Constant in the Performance of the Organo-Metallic Tri-Halide Perovskites' *Appl. Phys. Lett.* 110, 22, 222905 (2017).

[121] D. P. Almond, C. R. Bowen, 'An Explanation of the Photoinduced Giant Dielectric Constant of Lead Halide Perovskite Solar Cells' *J. Phys. Chem. Lett.* 6, 9, 1736–1740 (2015).

[122] Y.-T. Huang et al., 'Perovskite-Inspired Materials for Photovoltaics and Beyond : from Design to Devices' *Nanotechnology* 32, 13, 132004 (2021).

[123] Y. Chen, H. Zhou, 'Defects Chemistry in High-Efficiency and Stable Perovskite Solar Cells' *J. Appl. Phys.* 128, 6, 060903 (2020).

[124] S. G. Motti et al., 'Defect Activity in Lead Halide Perovskites' *Adv. Mater.* 31, 47, 1901183 (2019).

[125] J. Kang, L.-W. Wang, 'High Defect Tolerance in Lead Halide Perovskite $CsPbBr_3$' *J. Phys. Chem. Lett.* 8, 2, 489–493 (2017).

[126] N. Baig et al., 'Nanomaterials: a Review of Synthesis Methods, Properties, Recent Progress, and Challenges' *Mater. Adv.* 2, 6, 1821–1871 (2021).

[127] P. Iqbal et al., 'Nanotechnology: the "Top-Down" and "Bottom-Up" Approaches' in *Supramolecular Chemistry: from Molecules to Nanomaterials* (editors P. A. Gale, J. W. Steed), John Wiley & Sons, Ltd, Chichester, UK (2012).

[128] S. E. Creutz et al., 'Colloidal Nanocrystals of Lead-Free Double Perovskite (Elpasolite) Semiconductors: Synthesis and Anion Exchange To Access New Materials' *Nano Lett.* 18, 2, 1118–1123 (2018).

[129] M. Imran et al., 'Benzoyl Halides as Alternative Precursors for the Colloidal Synthesis of Lead-Based Halide Perovskite Nanocrystals' *J. Am. Chem. Soc.* 140, 7, 2656–2664 (2018).

[130] V. K. LaMer, R. H. Dinegar, 'Theory, Production and Mechanism of Formation of Monodispersed Hydrosols' *J. Am. Chem. Soc.* 72, 11, 4847–4854 (1950).

[131] J. Zeng et al., 'Colloidal Hybrid Nanocrystals: Synthesis, Properties, and Perspectives' in *Nanocrystal* (editor Y. Masuda), IntechOpen, London (2011).

[132] J. W. Gibbs, 'Method of Geometrical Representation of the Thermodynamic Properties of Substances by Means of Surfaces' *Trans. Connect. Acad. Arts Sci.* 2, 382–404 (1873).

[133] Y. Zhang et al., 'Nucleation-Controlled Growth of Superior Lead-Free Perovskite $Cs_3Bi_2I_9$ Single-Crystals for High-Performance X-Ray Detection' *Nat. Commun.* 11, 1, 2304 (2020).

[134] N. T. K. Thanh et al., 'Mechanisms of Nucleation and Growth of Nanoparticles in Solution' *Chem. Rev.* 114, 15, 7610–7630 (2014).

[135] R. Viswanatha, D. D. Sarma, 'Growth of Nanocrystals in Solution' in *Nanomaterials Chemistry: Recent Developments and New Directions* (editors C. N. R. Rao, A. Müller, A. K. Cheetham), Wiley-VCH, Weinheim, Germany (2007).

[136] D. V. Talapin et al., 'Evolution of an Ensemble of Nanoparticles in a Colloidal Solution: Theoretical Study' *J. Phys. Chem. B* 105, 49, 12278–12285 (2001).

[137] W. Ostwald, 'Studien über die Bildung und Umwandlung fester Körper' *Zeitschrift für Phys. Chemie* 22U, 1, 289–330 (1897).

[138] T. Pradeep, *A Textbook of Nanoscience and Nanotechnology*, McGraw-Hill Education, New York (2012).

[139] M. Kuno, *Introductory Nanoscience: Physical and Chemical Concepts*, Garland Science, New York (2011).

[140] F. T. Rabouw, C. de Mello Donega, 'Excited-State Dynamics in Colloidal Semiconductor Nanocrystals' *Top. Curr. Chem.* 374, 5, 58 (2016).

[141] A. L. Efros, M. Rosen, 'The Electronic Structure of Semiconductor Nanocrystals' *Annu. Rev. Mater. Sci.* 30, 1, 475–521 (2000).

[142] A. L. Efros, A. L. Efros, 'Interband Light Absorption in Semiconductor Spheres' *Sov. Phys. Semicond.* 16, 7, 772–775 (1982).

[143] L. E. Brus, 'Electron–Electron and Electron-Hole Interactions in Small Semiconductor Crystallites: the Size Dependence of the Lowest Excited Electronic State' *J. Chem. Phys.* 80, 9, 4403–4409 (1984).

[144] Y. Kayanuma, 'Quantum-Size Effects of Interacting Electrons and Holes in Semiconductor Microcrystals with Spherical Shape' *Phys. Rev. B* 38, 14, 9797–9805 (1988).

[145] D. Amgar et al., 'Inorganic and Hybrid Organo-Metal Perovskite Nanostructures: Synthesis, Properties, and Applications' *Adv. Funct. Mater.* 26, 47, 8576–8593 (2016).

[146] D. N. Minh et al., 'Room-Temperature Synthesis of Widely Tunable Formamidinium Lead Halide Perovskite Nanocrystals' *Chem. Mater.* 29, 13, 5713–5719 (2017).

[147] M. C. Weidman et al., 'Colloidal Halide Perovskite Nanoplatelets: an Exciting New Class of Semiconductor Nanomaterials' *Chem. Mater.* 29, 12, 5019–5030 (2017).

[148] Q. A. Akkerman et al., 'Tuning the Optical Properties of Cesium Lead Halide Perovskite Nanocrystals by Anion Exchange Reactions' *J. Am. Chem. Soc.* 137, 32, 10276–10281 (2015).

[149] S. Gupta et al., '25th Anniversary Article: Ion Exchange in Colloidal Nanocrystals' *Adv. Mater.* 25, 48, 6923–6944 (2013).

[150] M. Saruyama et al., 'Spontaneous Formation of Wurzite-CdS/Zinc Blende-CdTe Heterodimers through a Partial Anion Exchange Reaction' *J. Am. Chem. Soc.* 133, 44, 17598–17601 (2011).

[151] M. Gao et al., 'The Making of a Reconfigurable Semiconductor with a Soft Ionic Lattice' *Matter* 4, 12, 3874–3896 (2021).

[152] S. H. Lee, J. C. Rasaiah, 'Molecular Dynamics Simulation of Ion Mobility. 2. Alkali Metal and Halide Ions Using the SPC/E Model for Water at 25 °C' *J. Phys. Chem.* 100, 4, 1420–1425 (1996).

[153] Y. Bekenstein et al., 'Highly Luminescent Colloidal Nanoplates of Perovskite Cesium Lead Halide and Their Oriented Assemblies' *J. Am. Chem. Soc.* 137, 51, 16008–16011 (2015).

[154] Q. Wang et al., 'Quantum Confinement Effect and Exciton Binding Energy of Layered Perovskite Nanoplatelets' *AIP Adv.* 8, 2, 025108 (2018).

[155] A. Pan et al., 'Insight into the Ligand-Mediated Synthesis of Colloidal $CsPbBr_3$ Perovskite Nanocrystals: the Role of Organic Acid, Base, and Cesium Precursors' *ACS Nano* 10, 8, 7943–7954 (2016).

[156] G. Almeida et al., 'Role of Acid–Base Equilibria in the Size, Shape, and Phase Control of Cesium Lead Bromide Nanocrystals' *ACS Nano* 12, 2, 1704–1711 (2018).

[157] M. Kazes et al., 'Effect of Surface Ligands in Perovskite Nanocrystals: Extending in and Reaching out' *Acc. Chem. Res.* 54, 6, 1409–1418 (2021).

[158] A. F. Gualdrón-Reyes et al., 'Progress in Halide-Perovskite Nanocrystals with Near-

Unity Photoluminescence Quantum Yield' *Trends Chem.* 3, 6, 499–511 (2021).

[159] A. Dutta et al., 'Near-Unity Photoluminescence Quantum Efficiency for All $CsPbX_3$ (X = Cl, Br, and I) Perovskite Nanocrystals: a Generic Synthesis Approach' *Angew. Chem. Int. Ed.* 58, 17, 5552–5556 (2019).

[160] N. Droseros et al., 'Origin of the Enhanced Photoluminescence Quantum Yield in $MAPbBr_3$ Perovskite with Reduced Crystal Size' *ACS Energy Lett.* 3, 6, 1458–1466 (2018).

[161] J. Even et al., 'Analysis of Multivalley and Multibandgap Absorption and Enhancement of Free Carriers Related to Exciton Screening in Hybrid Perovskites' *J. Phys. Chem. C* 118, 22, 11566–11572 (2014).

[162] A. D. Wright et al., 'Electron–Phonon Coupling in Hybrid Lead Halide Perovskites' *Nat. Commun.* 7, 1, 11755 (2016).

[163] H. Utzat et al., 'Probing Linewidths and Biexciton Quantum Yields of Single Cesium Lead Halide Nanocrystals in Solution' *Nano Lett.* 17, 11, 6838–6846 (2017).

[164] H. C. Woo et al., 'Temperature-Dependent Photoluminescence of $CH_3NH_3PbBr_3$ Perovskite Quantum Dots and Bulk Counterparts' *J. Phys. Chem. Lett.* 9, 14, 4066–4074 (2018).

[165] X. Chi et al., 'Elucidating Surface and Bulk Emission in 3D Hybrid Organic-Inorganic Lead Bromide Perovskites' *Adv. Opt. Mater.* 6, 15, 1800470 (2018).

[166] T. Erdem, H. V. Demir, 'Color Science of Nanocrystal Quantum Dots for Lighting and Displays' *Nanophotonics* 2, 1, 57–81 (2013).

[167] M. C. Brennan et al., 'Universal Size-Dependent Stokes Shifts in Lead Halide Perovskite Nanocrystals' *J. Phys. Chem. Lett.* 11, 13, 4937–4944 (2020).

[168] M. C. Brennan et al., 'Origin of the Size-Dependent Stokes Shift in CsPbBr3 Perovskite Nanocrystals' *J. Am. Chem. Soc.* 139, 35, 12201–12208 (2017).

[169] A. Swarnkar et al., 'Colloidal $CsPbBr_3$ Perovskite Nanocrystals: Luminescence beyond Traditional Quantum Dots' *Angew. Chem.* 127, 51, 15644–15648 (2015).

[170] G. Rainò et al., 'Single Cesium Lead Halide Perovskite Nanocrystals at Low Temperature: Fast Single-Photon Emission, Reduced Blinking, and Exciton Fine Structure' *ACS Nano* 10, 2, 2485–2490 (2016).

[171] A. L. Efros, D. J. Nesbitt, 'Origin and Control of Blinking in Quantum Dots' *Nat. Nanotechnol.* 11, 8, 661–671 (2016).

[172] T. Ahmed et al., 'Mechanistic Investigation of the Defect Activity Contributing to the Photoluminescence Blinking of $CsPbBr_3$ Perovskite Nanocrystals' *ACS Nano* 13, 11, 13537–13544 (2019).

[173] G. Yuan et al., 'Two Mechanisms Determine Quantum Dot Blinking' *ACS Nano* 12, 4, 3397–3405 (2018).

[174] D. I. Chepic et al., 'Auger Ionization of Semiconductor Quantum Drops in a Glass Matrix' *J. Lumin.* 47, 3, 113–127 (1990).

[175] A. Alaei et al., 'Polymorphism in Metal Halide Perovskites' *Mater. Adv.* 2, 1, 47–63 (2021).

[176] S. Wang et al., 'Perovskite Nanocrystals: Synthesis, Stability, and Optoelectronic Applications' *Small Struct.* 2, 3, 2000124 (2021).

[177] Y. Zhou, Y. Zhao, 'Chemical Stability and Instability of Inorganic Halide Perovskites' *Energy Environ. Sci.* 12, 5, 1495–1511 (2019).

[178] M. V Kovalenko et al., 'Properties and Potential Optoelectronic Applications of Lead Halide Perovskite Nanocrystals' *Science* 358, 6364, 745–750 (2017).

[179] L. Protesescu et al., 'Dismantling the "Red Wall" of Colloidal Perovskites: Highly Luminescent Formamidinium and Formamidinium–Cesium Lead Iodide Nanocrystals' *ACS Nano* 11, 3, 3119–3134 (2017).

[180] Z. Li et al., 'Stabilizing Perovskite Structures by Tuning Tolerance Factor: Formation of Formamidinium and Cesium Lead Iodide Solid-State Alloys' *Chem. Mater.* 28, 1, 284–292 (2016).

[181] Y. Chen et al., 'Phase Engineering of Nanomaterials' *Nat. Rev. Chem.* 4, 5, 243–256 (2020).

[182] R. X. Yang, L. Z. Tan, 'Understanding Size Dependence of Phase Stability and Bandgap in $CsPbI_3$ Perovskite Nanocrystals' *J. Chem. Phys.* 152, 3, 034702 (2020).

[183] S. Sarang et al., 'Stabilization of the Cubic Crystalline Phase in Organometal Halide Perovskite Quantum Dots via Surface Energy Manipulation' *J. Phys. Chem. Lett.* 8, 21, 5378–5384 (2017).

[184] G. Niu et al., 'Review of Recent Progress in Chemical Stability of Perovskite Solar Cells' *J. Mater. Chem. A* 3, 17, 8970–8980 (2015).

[185] L. Xu et al., 'Stability and Reactivity: Positive and Negative Aspects for Nanoparticle Processing' *Chem. Rev.* 118, 7, 3209–3250 (2018).

[186] Y. Ouyang et al., 'Photo-Oxidative Degradation of Methylammonium Lead Iodide Perovskite: Mechanism and Protection' *J. Mater. Chem. A* 7, 5, 2275–2282 (2019).

[187] B. Luo et al., 'Lead Halide Perovskite Nanocrystals: Stability, Surface Passivation, and Structural Control' *ChemNanoMat* 3, 7, 456–465 (2017).

[188] G. Abdelmageed et al., 'Mechanisms for Light-Induced Degradation in $MAPbI_3$ Perovskite Thin Films and Solar Cells' *Appl. Phys. Lett.* 109, 23, 233905 (2016).

[189] F. Krieg et al., 'Colloidal $CsPbX_3$(X = Cl, Br, I) Nanocrystals 2.0: Zwitterionic Capping Ligands for Improved Durability and Stability' *ACS Energy Lett.* 3, 3, 641–646 (2018).

[190] D. Yang et al., 'Surface Chemistry of All Inorganic Halide Perovskite Nanocrystals: Passivation Mechanism and Stability' *Adv. Mater. Interfaces* 5, 8, 1701662 (2018).

[191] B. Luo et al., 'Peptide-Passivated Lead Halide Perovskite Nanocrystals Based on Synergistic Effect between Amino and Carboxylic Functional Groups' *Adv. Funct. Mater.* 27, 6, 1604018 (2017).

[192] G. H. Ahmed et al., 'Successes and Challenges of Core–Shell Lead Halide Perovskite Nanocrystals' *ACS Energy Lett.* 6, 4, 1340–1357 (2021).

[193] W. Lv et al., 'Improving the Stability of Metal Halide Perovskite Quantum Dots by Encapsulation' *Adv. Mater.* 31, 28, 1900682 (2019).

[194] A. Ambrosetti et al., 'Wavelike Charge Density Fluctuations and van der Waals Interactions at the Nanoscale' *Science* 351, 6278, 1171–1176 (2016).

[195] M. A. Boles et al., 'Self-Assembly of Colloidal Nanocrystals: from Intricate Structures to Functional Materials' *Chem. Rev.* 116, 18, 11220–11289 (2016).

[196] J. Zito, I. Infante, 'The Future of Ligand Engineering in Colloidal Semiconductor Nanocrystals' *Acc. Chem. Res.* 54, 7, 1555–1564 (2021).

[197] J. De Roo et al., 'Highly Dynamic Ligand Binding and Light Absorption Coefficient of Cesium Lead Bromide Perovskite Nanocrystals' *ACS Nano* 10, 2, 2071–2081 (2016).

[198] M. A. Boles et al., 'The Surface Science of Nanocrystals' *Nat. Mater.* 15, 2, 141–153

(2016).

[199] H. Huang et al., 'Lead Halide Perovskite Nanocrystals in the Research Spotlight: Stability and Defect Tolerance' *ACS Energy Lett.* 2, 9, 2071–2083 (2017).

[200] R. D. Shannon, 'Revised Effective Ionic Radii and Systematic Studies of Interatomic Distances in Halides and Chalcogenides' *Acta Crystallogr. A* 32, 5, 751–767 (1976).

[201] M. Pitaro et al., 'Tin Halide Perovskites: from Fundamental Properties to Solar Cells' *Adv. Mater.* 34, 1, 2105844 (2022).

[202] W. Ke et al., '"Unleaded" Perovskites: Status Quo and Future Prospects of Tin-Based Perovskite Solar Cells' *Adv. Mater.* 31, 47, 1803230 (2019).

[203] G. G. Graf, 'Tin, Tin Alloys, and Tin Compounds' in *Ullmann's Encyclopedia of Industrial Chemistry* (editors B. Elvers, C. Ley), 5th edition, Wiley-VCH, Weinheim (2000).

[204] A. K. Jaiswal et al., 'Tin Toxicity with Analytical Aspects and Its Management' *Int. J. Forensic Sci.* 2, 2, 78–83 (2019).

[205] K. Ahmad, M. A. Gondal, 'Bandgap Engineering of Tin Halide Perovskite Materials for Sustainable Energy Conversion Application' in *Sustainable Materials and Green Processing for Energy Conversion* (editors K. Y. Cheong, A. Apblett), Elsevier, Amsterdam (2021).

[206] J. K. Chen et al., 'Advances and Challenges in Tin Halide Perovskite Nanocrystals' *ACS Mater. Lett.* 3, 11, 1541–1557 (2021).

[207] P. Umari et al., 'Relativistic GW calculations on $CH_3NH_3PbI_3$ and $CH_3NH_3SnI_3$ Perovskites for Solar Cell Applications' *Sci. Rep.* 4, 1, 4467 (2015).

[208] A. Hermann et al., 'Spin–Orbit Effects in Structural and Electronic Properties for the Solid State of the Group-14 Elements from Carbon to Superheavy Element 114' *Phys. Rev. B* 82, 15, 155116 (2010).

[209] M. Awais et al., 'Tin Halide Perovskites Going Forward: Frost Diagrams Offer Hints' *ACS Mater. Lett.* 3, 3, 299–307 (2021).

[210] T. C. Jellicoe et al., 'Synthesis and Optical Properties of Lead-Free Cesium Tin Halide Perovskite Nanocrystals' *J. Am. Chem. Soc.* 138, 9, 2941–2944 (2016).

[211] A. E. Maughan et al., 'Perspectives and Design Principles of Vacancy-Ordered Double Perovskite Halide Semiconductors' *Chem. Mater.* 31, 4, 1184–1195 (2019).

[212] A. Wang et al., 'Controlled Synthesis of Lead-Free and Stable Perovskite Derivative Cs_2SnI_6 Nanocrystals via a Facile Hot-Injection Process' *Chem. Mater.* 28, 22, 8132–8140 (2016).

[213] D. S. Dolzhnikov et al., 'Ligand-Free, Quantum-Confined Cs_2SnI_6 Perovskite Nanocrystals' *Chem. Mater.* 29, 18, 7901–7907 (2017).

[214] S. Ghosh et al., 'Control Synthesis of Air-Stable Morphology Tunable Pb-Free Cs_2SnI_6 Perovskite Nanoparticles and Their Photodetection Properties' *Part. Part. Syst. Charact.* 35, 9, 1800199 (2018).

[215] Y. Xu et al., 'Ligand-Mediated Synthesis of Colloidal Cs_2SnI_6 Three-Dimensional Nanocrystals and Two-Dimensional Nanoplatelets.' *Nanotechnology* 30, 29, 295601 (2019).

[216] A. E. Maughan et al., 'Defect Tolerance to Intolerance in the Vacancy-Ordered Double Perovskite Semiconductors Cs_2SnI_6 and Cs_2TeI_6' *J. Am. Chem. Soc.* 138, 27, 8453–8464 (2016).

[217] C. de Mello Donegá et al., 'Physicochemical Evaluation of the Hot-Injection Method, a Synthesis Route for Monodisperse Nanocrystals' *Small* 1, 12, 1152–1162 (2005).

[218] H. Ma et al., 'Growth of Metal Halide Perovskite, from Nanocrystal to Micron-Scale Crystal: a Review' *Crystals* 8, 5, 182 (2018).

[219] Y. Jing et al., 'Sb^{3+} Doping-Induced Triplet Self-Trapped Excitons Emission in Lead-Free Cs_2SnCl_6 Nanocrystals' *J. Phys. Chem. Lett.* 7439–7444 (2019).

[220] A. Kaltzoglou et al., 'Mixed-Halide $Cs_2SnI_3Br_3$ Perovskite as Low Resistance Hole-Transporting Material in Dye-Sensitized Solar Cells' *Electrochim. Acta* 184, 466–474 (2015).

[221] L. Vegard, 'Die Konstitution der Mischkristalle und die Raumfüllung der Atome' *Zeitschrift für Phys.* 5, 1, 17–26 (1921).

[222] T.-W. Lin et al., 'Phase Transition and Energy Transfer of Lead-Free Cs_2SnCl_6 Perovskite Nanocrystals by Controlling the Precursors and Doping Manganese Ions' *J. Inf. Disp.* 20, 4, 209–216 (2019).

[223] Z. Xiao et al., 'Intrinsic Defects in a Photovoltaic Perovskite Variant Cs_2SnI_6' *Phys. Chem. Chem. Phys.* 17, 29, 18900–18903 (2015).

[224] B. Saparov et al., 'Thin-Film Deposition and Characterization of a Sn-Deficient Perovskite Derivative Cs_2SnI_6' *Chem. Mater.* 28, 7, 2315–2322 (2016).

[225] G. Yuan et al., 'Structural, Optical, and Thermal Properties of $Cs_2SnI_{6-x}Br_x$ Mixed Perovskite Solid Solutions' *Eur. J. Inorg. Chem.* 2019, 20, 2524–2529 (2019).

[226] S. Ding et al., 'Ligand Engineering of Perovskite Quantum Dots for Efficient and Stable Solar Cells' *J. Energy Chem.* 69, 626–648 (2022).

[227] K. Hills-Kimball et al., 'Recent Advances in Ligand Design and Engineering in Lead Halide Perovskite Nanocrystals' *Adv. Sci.* 8, 12, 2100214 (2021).

[228] H. Huang et al., 'Growth Mechanism of Strongly Emitting $CH_3NH_3PbBr_3$ Perovskite Nanocrystals with a Tunable Bandgap' *Nat. Commun.* 8, 1, 996 (2017).

[229] K. Xiao et al., 'Amine Treatment Induced Perovskite Nanowire Network in Perovskite Solar Cells: Efficient Surface Passivation and Carrier Transport' *Nanotechnology* 29, 6, 065401 (2018).

[230] Z. Xu et al., '$[(CH_3)_3NCH_2CH_2NH_3]SnI_4$: a Layered Perovskite with Quaternary/Primary Ammonium Dications and Short Interlayer Iodine−Iodine Contacts' *Inorg. Chem.* 42, 5, 1400–1402 (2003).

[231] V. K. Ravi et al., 'Origin of the Substitution Mechanism for the Binding of Organic Ligands on the Surface of $CsPbBr_3$ Perovskite Nanocubes' *J. Phys. Chem. Lett.* 8, 20, 4988–4994 (2017).

[232] E. Fanizza et al., 'Post-Synthesis Phase and Shape Evolution of $CsPbBr_3$ Colloidal Nanocrystals: the Role of Ligands' *Nano Res.* 12, 5, 1155–1166 (2019).

[233] A. Kaltzoglou et al., 'Optical-Vibrational Properties of the Cs_2SnX_6 (X = Cl, Br, I) Defect Perovskites and Hole-Transport Efficiency in Dye-Sensitized Solar Cells' *J. Phys. Chem. C* 120, 22, 11777–11785 (2016).

[234] A. Veronese et al., 'Highly Tunable Emission by Halide Engineering in Lead-Free Perovskite-Derivative Nanocrystals: the Cs_2SnX_6 (X = Cl, Br, Br/I, I) System' *Front. Chem.* 8, 35 (2020).

[235] P. Tyagi et al., 'Colloidal Organohalide Perovskite Nanoplatelets Exhibiting Quantum Confinement' *J. Phys. Chem. Lett.* 6, 10, 1911–1916 (2015).

[236] A. Heuer-Jungemann et al., 'The Role of Ligands in the Chemical Synthesis and

Applications of Inorganic Nanoparticles' *Chem. Rev.* 119, 8, 4819–4880 (2019).

[237] S. Kumar et al., 'Understanding the Ligand Effects on Photophysical, Optical, and Electroluminescent Characteristics of Hybrid Lead Halide Perovskite Nanocrystal Solids' *J. Phys. Chem. Lett.* 10, 24, 7560–7567 (2019).

[238] E. R. Dohner et al., 'Intrinsic White-Light Emission from Layered Hybrid Perovskites' *J. Am. Chem. Soc.* 136, 38, 13154–13157 (2014).

[239] D. Cortecchia et al., 'Broadband Emission in Two-Dimensional Hybrid Perovskites: the Role of Structural Deformation' *J. Am. Chem. Soc.* 139, 1, 39–42 (2017).

[240] T. Okuda et al., 'Static and Dynamic Structures of Monoalkylammonium Hexachlorostannate(IV) Complexes $[C_nH_{2n+1}NH_3]_2SnCl_6$ (n = 2 to 6) Studied by Means of NQR and NMR' *J. Mol. Struct.* 296, 1–2, 103–110 (1993).

[241] K. Pradeesh et al., 'Exciton Switching and Peierls Transitions in Hybrid Inorganic-Organic Self-Assembled Quantum Wells' *Appl. Phys. Lett.* 95, 17, 173305 (2009).

[242] N. Yang, H. Sun, 'Bismuth: Environmental Pollution and Health Effects' in *Encyclopedia of Environmental Health* (editor J. O. Nriago), 1st edition, Elsevier, Amsterdam (2011).

[243] Z. Jin et al., 'A Critical Review on Bismuth and Antimony Halide Based Perovskites and Their Derivatives for Photovoltaic Applications: Recent Advances and Challenges' *J. Mater. Chem. A* 8, 32, 16166–16188 (2020).

[244] S. H. Reddy et al., 'Can Perovskite Inspired Bismuth Halide Nanocrystals Outperform Their Lead Counterparts?' *J. Mater. Chem. A* 8, 26, 12951–12963 (2020).

[245] A. J. Lehner et al., 'Crystal and Electronic Structures of Complex Bismuth Iodides $A_3Bi_2I_9$ (A = K, Rb, Cs) Related to Perovskite: Aiding the Rational Design of Photovoltaics' *Chem. Mater.* 27, 20, 7137–7148 (2015).

[246] E. E. Morgan et al., 'Tunable Perovskite-Derived Bismuth Halides: $Cs_3Bi_2(Cl_{1-x}I_x)_9$' *Inorg. Chem.* 59, 6, 3387–3393 (2020).

[247] M.-Q. Li et al., 'Structure Tunable Organic-Inorganic Bismuth Halides for an Enhanced Two-Dimensional Lead-Free Light-Harvesting Material' *Chem. Mater.* 29, 13, 5463–5467 (2017).

[248] M. Leng et al., 'Surface Passivation of Bismuth-Based Perovskite Variant Quantum Dots To Achieve Efficient Blue Emission' *Nano Lett.* 18, 9, 6076–6083 (2018).

[249] S.-Y. Kim et al., 'Wide Range Tuning of Bandgap Energy of $A_3B_2X_9$ Perovskite-Like Halides' *Scr. Mater.* 166, 107–111 (2019).

[250] Z. Xiao et al., 'From Lead Halide Perovskites to Lead-Free Metal Halide Perovskites and Perovskite Derivatives' *Adv. Mater.* 31, 47, 1803792 (2019).

[251] M. Wang et al., 'Lead-Free Perovskite Materials for Solar Cells' *Nano-Micro Lett.* 13, 1, 62 (2021).

[252] B. Ghosh et al., 'Poor Photovoltaic Performance of $Cs_3Bi_2I_9$: an Insight through First-Principles Calculations' *J. Phys. Chem. C* 121, 32, 17062–17067 (2017).

[253] K. A. Huynh et al., 'Halide Perovskite Photocatalysis: Progress and Perspectives' *J. Chem. Technol. Biotechnol.* 95, 10, jctb.6342 (2020).

[254] H. Zhou et al., 'Towards Highly Efficient Photocatalysts Using Semiconductor Nanoarchitectures' *Energy Environ. Sci.* 5, 5, 6732 (2012).

[255] S. S. Bhosale et al., 'Mechanism of Photocatalytic CO_2 Reduction by Bismuth-Based Perovskite Nanocrystals at the Gas–Solid Interface' *J. Am. Chem. Soc.* 141, 51, 20434–20442 (2019).

[256] Y. Dai et al., 'A Supported Bismuth Halide Perovskite Photocatalyst for Selective Aliphatic and Aromatic C–H Bond Activation' *Angew. Chem. Int. Ed.* 59, 14, 5788–5796 (2020).

[257] B.-M. Bresolin et al., 'Pb-Free $Cs_3Bi_2I_9$ Perovskite as a Visible-Light-Active Photocatalyst for Organic Pollutant Degradation' *Nanomaterials* 10, 4, 763 (2020).

[258] H. Zhao et al., 'Dimethylammonium Iodide Stabilized Bismuth Halide Perovskite Photocatalyst for Hydrogen Evolution' *Nano Res.* 14, 4, 1116–1125 (2021).

[259] L. Romani et al., 'Experimental Strategy and Mechanistic View to Boost the Photocatalytic Activity of $Cs_3Bi_2Br_9$ Lead-Free Perovskite Derivative by g-C_3N_4 Composite Engineering' *Adv. Funct. Mater.* 31, 46, 2104428 (2021).

[260] A. Wang et al., 'Recent Advances of Graphitic Carbon Nitride-Based Structures and Applications in Catalyst, Sensing, Imaging, and LEDs' *Nano-Micro Lett.* 9, 4, 47 (2017).

[261] L. H. Amorin et al., 'Electronic, Structural, Optical, and Photocatalytic Properties of Graphitic Carbon Nitride' *New J. Chem.* 43, 34, 13647–13653 (2019).

[262] E. O. Oseghe et al., 'Multi-Dimensional Applications of Graphitic Carbon Nitride

Nanomaterial: a Review' *J. Mol. Liq.* 344, 117820 (2021).

[263] M. Ismael, 'A Review on Graphitic Carbon Nitride (g-C_3N_4) Based Nanocomposites: Synthesis, Categories, and Their Application in Photocatalysis' *J. Alloys Compd.* 846, 156446 (2020).

[264] J. Liang et al., 'A Review on g-C_3N_4 Incorporated with Organics for Enhanced Photocatalytic Water Splitting' *J. Mater. Chem. A* 9, 22, 12898–12922 (2021).

[265] J. Luo et al., 'Halide Perovskite Composites for Photocatalysis: a Mini Review' *EcoMat* 3, 1, e12079 (2021).

[266] M. Corti et al., 'g-C_3N_4/Metal Halide Perovskite Composites as Photocatalysts for Singlet Oxygen Generation Processes for the Preparation of Various Oxidized Synthons' *Catal. Sci. Technol.* 11, 6, 2292–2298 (2021).

[267] Y. Zhang et al., 'Direct-Indirect Nature of the Bandgap in Lead-Free Perovskite Nanocrystals' *J. Phys. Chem. Lett.* 8, 14, 3173–3177 (2017).

[268] C. K. Ng et al., 'Scalable Synthesis of Colloidal $CsPbBr_3$ Perovskite Nanocrystals with High Reaction Yields through Solvent and Ligand Engineering' *Nanoscale* 12, 8, 4859–4867 (2020).

[269] M. Leng et al., 'All-Inorganic Bismuth-Based Perovskite Quantum Dots with Bright Blue Photoluminescence and Excellent Stability' *Adv. Funct. Mater.* 28, 1, 1704446 (2018).

[270] Z.-Z. Ma et al., 'Water-Induced Fluorescence Enhancement of Lead-Free Cesium Bismuth Halide Quantum Dots by 130% for Stable White Light-Emitting Devices' *Nanoscale* 12, 6, 3637–3645 (2020).

[271] Y. N. Ivanov et al., 'Phase Transitions of $Cs_3Sb_2I_9$, $Cs_3Bi_2I_9$, and $Cs_3Bi_2Br_9$ Crystals' *Inorg. Mater.* 37, 6, 623–627 (2001).

[272] F. Lazarini, 'Caesium Enneabromodibismuthate(III)' *Acta Crystallogr. Sect. B Struct. Crystallogr. Cryst. Chem.* 33, 9, 2961–2964 (1977).

[273] O. Lindqvist et al., 'The Crystal Structure of Cesium Bismuth Iodide, $Cs_3Bi_2I_9$.' *Acta Chem. Scand.* 22, 2943–2952 (1968).

[274] J. Wang et al., 'Determination of Crystal Structure of Graphitic Carbon Nitride: Ab Initio Evolutionary Search and Experimental Validation' *Chem. Mater.* 29, 7, 2694–2707 (2017).

[275] M. J. Bojdys et al., 'Ionothermal Synthesis of Crystalline, Condensed, Graphitic Carbon Nitride' *Chem. - A Eur. J.* 14, 27, 8177–8182 (2008).

[276] A. Speltini et al., 'Rationalization of Hydrogen Production by Bulk g-C_3N_4: an In-Depth Correlation between Physico-Chemical Parameters and Solar Light Photocatalysis' *RSC Adv.* 8, 69, 39421–39431 (2018).

[277] R. F. Ali et al., 'Green Solvent Assisted Synthesis of Cesium Bismuth Halide Perovskite Nanocrystals and the Influences of Slow and Fast Anion Exchange Rates' *Nanoscale Adv.* 1, 11, 4442–4449 (2019).

[278] M. Gao et al., 'Controlled Synthesis and Photostability of Blue Emitting $Cs_3Bi_2Br_9$ Perovskite Nanocrystals by Employing Weak Polar Solvents at Room Temperature' *J. Mater. Chem. C* 7, 12, 3688–3695 (2019).

[279] J. Pal et al., 'Synthesis and Optical Properties of Colloidal $M_3Bi_2I_9$ (M = Cs, Rb) Perovskite Nanocrystals' *J. Phys. Chem. C* 122, 19, 10643–10649 (2018).

[280] P. Lefebvre et al., 'General Formalism for Excitonic Absorption Edges in Confined Systems with Arbitrary Dimensionality' *Le J. Phys. IV* 03, C5, 377–380 (1993).

[281] R. J. Elliott, 'Intensity of Optical Absorption by Excitons' *Phys. Rev.* 108, 6, 1384–1389 (1957).

[282] S. Rieger et al., 'Excitons and Narrow Bands Determine the Optical Properties of Cesium Bismuth Halides' *Phys. Rev. B* 100, 20, 201404 (2019).

[283] K. M. McCall et al., 'Strong Electron–Phonon Coupling and Self-Trapped Excitons in the Defect Halide Perovskites $A_3M_2I_9$ (A = Cs, Rb; M = Bi, Sb)' *Chem. Mater.* 29, 9, 4129–4145 (2017).

[284] M. N. Tran et al., 'Resolving the Discrepancies in the Reported Optical Absorption of Low-Dimensional Non-Toxic Perovskites, $Cs_3Bi_2Br_9$ and Cs_3BiBr_6' *J. Mater. Chem. C* 8, 30, 10456–10463 (2020).

[285] T. Takagahara, 'Electron–Phonon Interactions in Semiconductor Nanocrystals' *J. Lumin.* 70, 1–6, 129–143 (1996).

[286] W. Zhu et al., 'Deciphering the Degradation Mechanism of the Lead-Free All Inorganic Perovskite Cs_2SnI_6' *npj Mater. Degrad.* 3, 1, 7 (2019).

[287] K. Sandeep, 'Revealing the Role of Aggregation and Surface Chemistry in the Bi-phasic

Anion Exchange Reactions of Cesium Lead Halide Perovskites' *ChemistrySelect* 5, 13, 4034–4039 (2020).

[288] D. Baranov et al., 'Aging of Self-Assembled Lead Halide Perovskite Nanocrystal Superlattices: Effects on Photoluminescence and Energy Transfer' *ACS Nano* 15, 1, 650–664 (2021).

[289] K. L. Willett, R. A. Hites, 'Chemical Actinometry: Using o-Nitrobenzaldehyde to Measure Lamp Intensity in Photochemical Experiments' *J. Chem. Educ.* 77, 7, 900 (2000).